

**Modification of the Electrochemical Properties of
Graphite-based Polyaniline Composite for
Supercapacitor Application**

DISSERTATION

Zur Erlangung des akademischen Grades
Doktor rerum naturalium
(Dr. rer. nat.)
vorgelegt
dem Bereich Mathematik und Naturwissenschaften
der Technischen Universität Dresden
von

M. Eng. Xueyan Zhao

geboren am 03.05.1990 in Sichuan, V. R. China

Tag der Verteidigung: 26.03.2019
Gutachterin: Prof. Dr. Brigitte Voit

Die Dissertation wurde in der Zeit von Oktober/2015 bis März/2019 im
Leibniz-Institut für Polymerforschung Dresden e. V. angefertigt.

Reviewers:

Prof. Dr. Brigitte Voit

Prof. Dr. Xinliang Feng

List of Abbreviations and Symbols

Abbreviations

APS	ammonium persulfate
CV	cyclic voltammetric
CVD	chemical vapor deposition
d	distance
DBSA	4-dodecylbenzenesulfonic acid
EC	electrochemical capacitor
EDLC	electrical double-layer capacitor
EDX	energy dispersive X-ray spectrometry
EG	expanded graphite
FTIR	Fourier-transform infrared spectroscopy
GNP	graphite nanoplates
GO	graphite oxide
HH	hydrazine monohydrate
PANI	polyaniline
PDA	polydopamine
PTFE	polytetrafluoroethylene
PVA	polyvinyl alcohol
rGO	reduced graphite oxide
rpm	revolutions per minute
SEM	scanning electron microscope
SS	stainless steel
TA	tannic acid
TGA	thermogravimetric analysis
UV	ultraviolet
wt.	weight

XPS	X-ray photoelectron spectroscopy
XRD	X-ray diffraction

Symbols

c	specific capacitance
C	capacitance
E	energy density
I	current
P	power density
R	resistance
V	potential
ν	potential scan rate
θ	angle

Units

$^{\circ}\text{C}$	degree centigrade
cm	centimetre
F	faraday
g	gram
h	hour
K	kelvin
kN	kilonewton
kV	kilovolt
mg	milligram
min	minute
mL	millilitre
mm	millimetre
mV	millivolt

nm	nanometre
s	second
S	siemens
V	volt
W	watt

Contents

1. Introduction	6
2. Aim of this work	8
3. Theoretical background.....	11
3.1. Supercapacitor	11
3.1.1. Fundamental	11
3.1.2. Mechanism	15
3.2. Polyaniline	19
3.2.1. Structure and properties.....	19
3.2.2. Synthesis.....	21
3.2.3. Supercapacitor application	26
3.3. Carbon-based PANI composite	33
3.3.1. Preparation methods and electrochemical performance.....	33
3.3.2. Strategies to improve the electrochemical properties.....	36
4. Experimental part.....	44
4.1. Materials	44
4.2. Sample Preparation	44
4.2.1. Synthesis of PANI/GNP composites.....	44
4.2.2. Synthesis of PANI/(GO-PDA) and PANI/GO-PDA composites.....	45
4.2.3. Synthesis of PANI/(rGO-TA), PANI/(rGO-HH), and PANI/GNP composites.....	47
4.3. Instruments and Characterization methods.....	48
5. Result and Discussions.....	52
5.1. PANI/GNP composites with different oxidant and dopant loading	52
5.1.1. Introduction	52
5.1.2. Structural characterization of PANI/GNP composites.....	53
5.1.3. Effect of dopant and oxidant amount on electrochemical behavior	58
5.1.4. Effect of oxidant nature on electrochemical behavior.....	65
5.1.5. Summary	69
5.2. PANI/(GO-PDA) and PANI/GO-PDA composites.....	70
5.2.1. Introduction	70
5.2.2. Structural characterization of PDA-functionalized GO	71
5.2.3. Electrochemical properties and morphology of PANI/GO-PDA composites.....	75
5.2.4. Electrochemical properties and morphology of PANI/(GO-PDA) composites.....	79

5.2.5.	Summary	83
5.3.	PANI/TA-doped rGO and PANI/TA-doped GNP composites.....	84
5.3.1.	Introduction	84
5.3.2.	Structural characterization of TA-doped rGO and GNP	85
5.3.3.	Electrochemical properties and morphology of PANI/rGO	89
5.3.4.	Electrochemical properties and morphology of PANI/GNP	95
5.3.5.	Solid-state symmetric supercapacitor device	97
5.3.6.	Summary	102
6.	Conclusions	104
7.	Outlook.....	109
	Bibliography.....	111
	Publications and Conference Contributions.....	123
	Acknowledgement.....	124
	Versicherung	126
	Erklärung.....	126

1. Introduction

Supercapacitors, which are also named as electrochemical capacitors (EC), have drawn a lot of attention in recent years. [1] The rapid growth of portable electronics and hybrid electric vehicles in the modern society calls for energy suppliers with not only high energy density but also high power density. As is commonly known, the conventional dielectric capacitors own high power density but low energy density; while the batteries and fuel cells own high energy density but low power density. Some researchers reported that supercapacitors can bridge the power/energy gap between the conventional dielectric capacitors and the batteries. [2-4] Moreover, supercapacitors have long cycle life and are promising safe and environment-friendly energy storage devices. [5, 6] A typical supercapacitor usually consists of two electrodes (an anode and a cathode), electrolyte, a separator, and a current collector. Among these components, the electrodes are the most crucial parts. [7]

Up to now, many active materials have been developed to be supercapacitor electrodes. [8, 9] Depending on the type of active materials and the corresponding charge storage and release mechanisms, ECs can be divided into electrical double-layer capacitors (EDLCs) and pseudocapacitors. EDLCs are usually based on carbonaceous materials with high specific surface area, such as mesoporous carbon, carbon nanotubes, graphite, graphene, etc. [10, 11] EDLCs charge and discharge by rapid ions adsorption and desorption. [12, 13] Due to this mechanism, EDLCs own high power density and long-term cycle stability, but suffer from low energy density. Pseudocapacitors commonly function through rapid and reversible redox reactions of faradic materials (transition metal oxides or conducting polymers). [14, 15] This battery-like behavior endows pseudocapacitors with much higher specific capacitances and energy densities compared to EDLCs. Polyaniline (PANI) is considered to be one of the most competitive faradic materials due to its cost-effectiveness, facile synthesis, and large theoretical specific pseudocapacitance. [16-18] However, similar to other conducting polymers, the low power density and poor stability during the charge/discharge cycle obstruct the development of PANI for commercial supercapacitor electrode. [19] In

order to alleviate these shortcomings of PANI, some researchers turned to develop carbon-based PANI composites. [12, 20, 21]

It has been reported that PANI/carbonaceous material composites can combine the electrical double-layer capacitance of the carbonaceous material and the pseudocapacitance of PANI. [22, 23] Moreover, the carbonaceous material can offer a transportation complex for electron and a structural support for the PANI, thus increasing the overall conductivity and stability of composites. [24] Among various carbonaceous materials, graphene has attracted tremendous attention due to its intriguing two-dimensional structure and high theoretical specific surface area. [25, 26] Recently, Memon *et al.* developed flexible supercapacitor electrodes by electrodepositing PANI on macroporous graphene thin films. The obtained hybridized electrode exhibits excellent specific capacitance and long-term cycle stability. [27] However, the high cost of producing monolayer graphene obstacles the large-scale production PANI/graphene composites for supercapacitor purpose.

In my study, graphite nanoplates (GNP), which is composed by multiple layers of graphene, and reduced graphite oxide (rGO) were used as alternatives to the monolayer graphene. GNP and rGO also own large specific surface area, high mechanical strength, and good electrical conductivity; and their production methods are mature and cost-effective. GNP is usually derived from low-cost natural graphite; and rGO can be produced by various oxidation-reduction methods. [28-30] In order to obtain a positive synergetic effect between the PANI and the GNP or rGO, and to enhance the overall electrochemical properties of the composites, this research not only investigated the effect of certain synthesis parameters, but also proposed two green methods of pre-modification of GNP or rGO.

2. Aim of this work

Composites of PANI and carbonaceous materials can combine the virtues of pseudocapacitor and EDLC, namely the high capacitance and energy density of PANI and the excellent conductivity, stability and power density of the carbonaceous component. Graphene is extensively considered as the most promising carbonaceous filler, but the production of graphene is expensive and difficult. With the aim to develop PANI-related composites with not only good electrochemical performance but also low cost, this research used low-cost graphite (graphite nanoplates, GNP or reduced graphite oxide, rGO) as alternatives to graphene. The electrochemical performances of PANI/GNP and PANI/rGO composites were studied, and methods of modification were proposed in order to enhance the electrochemical performance.

Considering the cost and technical feasibility for future large-scale manufacturing, the synthesis method of in-situ polymerization of aniline in the presence of carbonaceous materials was used throughout this work. Even though using PANI-related composites as supercapacitor electrodes have been extensively reported, the relationship between the synthesis parameters and the electrochemical performance of the obtained composites has been scarcely investigated. Therefore, in the first section of this research the influence of certain synthesis parameters on the electrochemical properties of PANI/GNP composites was systematically investigated. The weight ratio of PANI to GNP was set as 1 to 0.1 or 1 to 1. These PANI/GNP composites were synthesized with or without dopant, with different kinds of oxidants, and with various contents of oxidant. Then the cyclic voltammetric behavior, conductivities, and morphologies of the PANI/GNP composites were studied. Besides, the specific capacitances of all the investigated PANI/GNP composites were calculated based on the cyclic voltammograms in order to evaluate their energy storage abilities.

There are some obstacles to produce graphite (GNP or rGO)-based PANI composites with good electrochemical performance. For the GNP-based PANI composites: (1) GNP layers tend to cluster together, thus decrease the overall specific surface area, conductivity and capacitance of the composites; (2) the interaction between GNP and PANI is weak, which has negative effect on the distribution PANI

and weakens the synergic effect of components. Using rGO as the graphite component also suffer from the restacking of rGO layers but can achieve better interaction with PANI; an additional drawback of rGO-based PANI composite is the toxicity of the commonly used reducing agents of graphite oxide (GO). In order to overcome these drawbacks of rGO and GNP, in the second and third sections of the research two green chemicals, namely polydopamine and tannic acid, were used to pre-modify rGO or GNP.

The oxidative process of polymerizing dopamine into polydopamine was expected to reduce graphite oxide and to increase the interaction between the graphite (GO-PDA in this section) and the PANI component. Moreover, the PDA coated on GO-PDA was expected to interact with PANI, thus promote a homogeneous dispersion of PANI in the composites. The composites of GO-PDA and PANI were prepared by two different routes. Reducing GO by the polymerization of dopamine in the first step, followed by in-situ polymerization of aniline in the presence of the obtained GO-PDA resulted in PANI/(GO-PDA) composites. Otherwise, in-situ polymerization of PANI/GO composite in the first step followed by reducing this composite by polymerization of dopamine produced PANI/GO-PDA composites. The structure of the GO-PDAs were characterized; and then the electrochemical properties of PANI/(GO-PDA) and PANI/GO-PDA composites and some related influencing factors, such as specific surface area, morphology, and conductivity of composites have been investigated.

The environmental friendly tannic acid (TA) was used to develop the electrochemical properties of both PANI/rGO and PANI/GNP composites. TA was expected to reduce GO and suppress the restacking of rGO-TA and GNP-TA. The reduction effect of TA on GO was studied by various structural characterization techniques. Then PANI/(rGO-TA) and PANI/(GNP-TA) composites were produced by in-situ polymerization of aniline in the presence of rGO-TA and GNP-TA, respectively. The electrochemical properties, morphologies, conductivities and surface areas of the PANI/(rGO-TA) and PANI/(GNP-TA) composites were investigated and compared with those of PANI/(rGO-HH), in which hydrazine hydrate (HH) has been used as reducing agent, and PANI/GNP composites, respectively. Moreover, the corresponding solid-state two-electrode supercapacitor devices have been assembled in order to test their electrochemical performance in practical use.

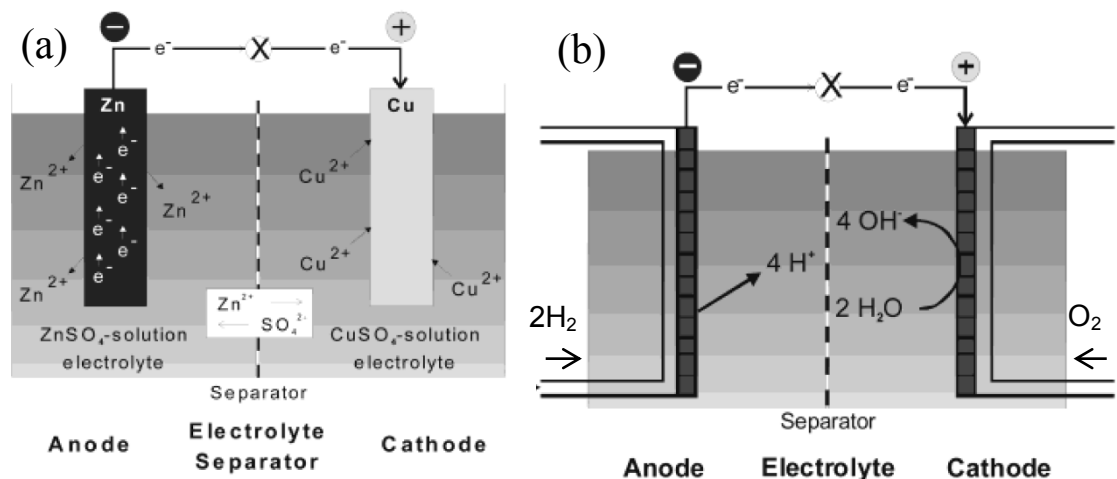
In a word, this work is aimed to develop a green and cost-effective way to produce composites of PANI and carbonaceous material with good electrochemical properties. For this purpose, low-cost rGO and GNP were used as the carbonaceous components, and chemical oxidative polymerization was used as synthesis method. The effect of certain synthesis parameters on the electrochemical performance of composites was investigated. Pre-modification of rGO or GNP by polydopamine or tannic acid were proposed in order to replace the commonly used toxic reducing agents for rGO, retard the restacking of rGO and GNP, and simultaneously enhance the interaction between graphite component (rGO or GNP) and PANI.

3. Theoretical background

3.1. Supercapacitor

3.1.1. Fundamental

Electrochemical energy conversion/storage devices can be divided into three main types: batteries, fuel cells, and supercapacitor. [31, 32] The operation of batteries and fuel cells are supported by coupling two chemical reactions at the anode and cathode as illustrated in Fig. 3.1 (a) and (b). Batteries are closed system; while fuel cells are open system, namely the active materials for redox reactions are supplied from the outside of cell. Both of battery and fuel cell own high energy density, but suffer from low power density. It is because the chemical reactions are time-consuming, and the transfer of charges is heterogeneous. On the other hand, supercapacitors operate more like charge/discharge devices, which simply involve ionic movement at the electrode surface. [33] Therefore, compared to secondary batteries and fuel cells, supercapacitors show higher power density (exceeding 1 kW kg^{-1}), longer cycle life (more than 100 times higher than batteries) and shorter charge/discharge time (within seconds). [34] As shown in Fig. 3.1 (c), supercapacitors, which include double layer capacitors and pseudocapacitors, fill the power/energy gap between the batteries and conventional dielectric capacitors. [35] In another word, supercapacitors show high energy density without sacrificing the power density.



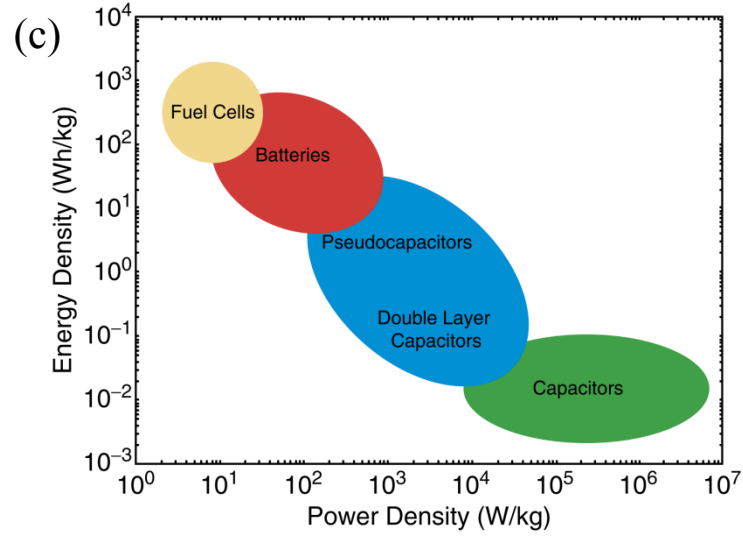


Fig. 3.1 Schematic illustration of (a) a battery (Daniell cell) and (b) a fuel cell, adapted with permission from American Chemical Society [31]; (c) plot of specific power against specific energy (Ragone plot) for various electrical energy conversion and storage devices. Reused with permission from Materials Research Society. [35]

A typical structure of supercapacitor is illustrated in Fig. 3.2. [36] Obviously, a supercapacitor is usually composed of two electrically isolated electrodes, an ion permeable separator, electrolyte and two current collectors. The interfaces between electrodes and electrolyte exhibit as dielectric capacitors, thus the entire cell are similar to two dielectric capacitors in series. [37-39] The relationship between the overall capacitance (C_{cell}) and the capacitances of positive (C_p) and negative electrode (C_n) is shown in Equation 3.1.

$$\frac{1}{C_{cell}} = \frac{1}{C_p} + \frac{1}{C_n} \quad (3.1)$$

The energy (E) and power (P) of supercapacitors can be calculated by

$$E = \frac{1}{2} C_{cell} V^2 \quad (3.2)$$

$$P = \frac{V^2}{4R_s} \quad (3.3)$$

Obviously, the overall capacitance is dominated by the electrode with lower capacitance. And the electrochemical performance of a supercapacitor rely on the equivalent series

resistance (R_s), C_{cell} , and especially the cell voltage (V), since both of E and P are proportional to the square of V .

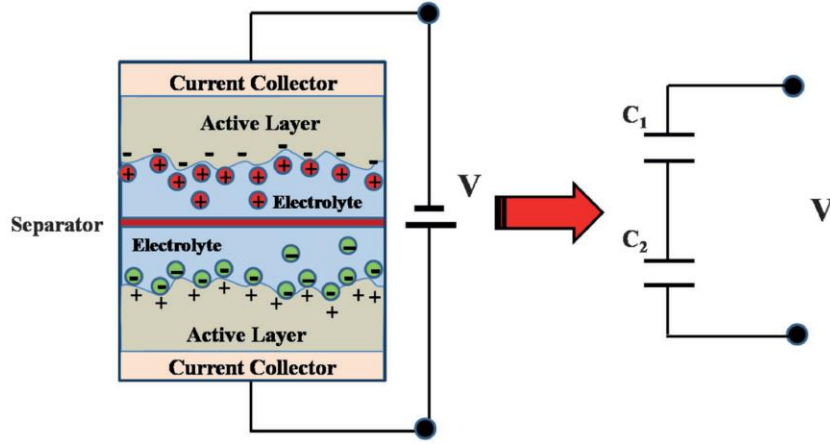


Fig. 3.2 Schematic representation of a supercapacitor cell. Reused with permission from John Wiley and Sons. [36]

The cell voltage of a supercapacitor largely depends on the voltage stability window of the electrolyte. Aqueous electrolytes, such as sulphuric acid (H_2SO_4), potassium hydroxide (KOH), sodium sulphate (Na_2SO_4), etc., show relatively lower decomposition voltage (about 1.23 V) than the non-aqueous electrolytes (up to 3.5-4 V), such as acetonitrile, propylene carbonate, tetraethylammonium tetrafluoroborate, etc. [40] Therefore, non-aqueous electrolytes have been used in many commercial supercapacitors, even though the aqueous electrolytes own lower cost, lower internal resistance, and higher specific capacitance due to the intrinsic higher dielectric constant. [34] Recently, lots of efforts have been devoted to develop ionic liquids as electrolytes in energy storage devices. Ionic liquid is known as melted salt, whose salt lattice energy is counterbalanced by the outside heat. They are solvent free, and their voltage stability window relies only on the electrochemical stability of ions. Therefore, they show wide voltage stability windows (even higher than 4 V). Chen *et al.* developed a full-cell supercapacitor using polyaniline (PANI) as electrode and ionic liquid (1-ethyl-3-methylimidazolium tetrafluoroborate) as electrolyte. The energy density and power density of this supercapacitor can reach remarkable 84 Wh kg^{-1} and 182 kW kg^{-1} , respectively. [41] However, the ionic conductivity of ionic liquid decreases with the

temperature decreasing and shows just a few millisiemens per centimetre at ambient temperature. In order to overcome this drawback, Brandt *et al.* proposed using the mixture of ionic liquids and organic solvents as the electrolyte of supercapacitor. [42] Moreover, aiming to extend the application field of supercapacitor, many researchers have studied solid electrolyte such as hydrogel electrolyte based on poly(ethylene oxide) or polyvinyl alcohol. [43] The solid electrolyte can act as both the electrolyte and separator, which means excess separator is not necessary. Compared to aqueous electrolyte, solid electrolyte own wider potential window, easy to assemble and might has positive effect on the cycle stability of supercapacitor. [44] On the other hand, the electrolyte concentration should be set at a reasonable value: too low will retard the building-up of ionic double-layer; too high will reduce the ion activity due to less water hydration, and result in decrease of specific capacitance and energy density. [45]

The equivalent series resistance (R_s) in Equation 3.3 is comprised of the interfacial resistance between the electrode and the current collector, the diffusion resistance of ions moving through electrode and separator, electronic resistance of the electrode, and electrolyte resistance. [46] In order to decrease the R_s , not only the electrode and electrolyte should be optimized, but also the contact impedance between the active materials and current collector should be controlled to a low value. [47] In the study of Chmiola *et al.*, properly increasing the size of micropores (diameter < 2 nm) in the carbon electrode decreased the R_s of the supercapacitor, thus increased the specific capacitance. [48] Recently, many efforts have been devoted to develop binder-free supercapacitors and even free-standing supercapacitors, in which not only the inactive binder but also current collector is not necessary. [49, 50] Jiang *et al.* reported a binder-free electrode, which was produced by directly grow cobalt-manganese composite oxide nanostructures on a three-dimensional nickel foam. The obtained electrode exhibited a high specific capacitance of 840.2 F g⁻¹ at a current density of 10 A g⁻¹ and excellent cycle stability (retained 102 % capacitance after 7000 cycles). [51] Xiao *et al.* prepared freestanding mesoporous vanadium nitride/carbon nanotube hybrid electrodes and then assembled it into all-solid-state supercapacitors by using phosphoric acid-polyvinyl alcohol (H₃PO₄-PVA) gel as electrolyte. The obtained supercapacitor showed a specific volume capacitance of 7.9 F cm⁻³ at a current density of 0.025 A cm⁻³; and the R_s of it was measured to be as small as 22 Ω cm². [52]

Electrochemical performances of active materials are usually evaluated by three testing methods, namely cyclic voltammetric (CV) test, galvanostatic charge and discharge (GCD), and electrochemical impedance spectroscopy (EIS). Additionally, testing systems can be divided into two-electrode cells and three-electrode cells according to their geometry. Compared to a two-electrode system, which contains a working electrode and a counter electrode, a three-electrode system contains an additional reference electrode. In a three-electrode system, the current flow between the working electrode and counter electrode, and the voltage on working electrode can be accurately measured based on the potential of the reference electrode. In comparison, the two-electrode system is more common in practical use, and three-electrode system is more accurate for the research work.

3.1.2. Mechanism

According to the charge storage mechanisms of different electrode materials, supercapacitors can be divided into electrochemical double-layer capacitors (EDLCs) and pseudocapacitors. EDLCs are usually made up by carbonaceous electrode and store charge through physical ionic adsorption. Pseudocapacitors commonly use transition metal oxides or conducting polymers as the electrode, and charge is stored and released through rapid redox reactions. [1, 22] Fig. 3.2 illustrated a typical EDLC: during the charging process, the external electrical field drives electrons moving from the negative electrode to the positive electrode. Then spontaneous electrolyte ions with the counter charge are attracted around the responsible electrode. The interface between the active material and the electrolyte behaves as a conventional dielectric capacitor, but with much higher capacitance (C) due to the atomic range of the charge separation distance (d) and larger accessible surface area (A).

$$C = \frac{A\epsilon}{4\pi d} \quad (3.4)$$

This mechanism of EDLCs, i.e. simple ion adsorption/desorption at the electrode surfaces, endows them with high power density and long-term cycle stability. Moreover, the pore size, pore size distribution and the surface wettability of electrode materials,

which are related to the accessible surface area, are important for the capacitance of an EDLC.

Pseudocapacitors, also named as redox capacitors, are another kind of supercapacitors. Energy is stored via fast and reversible electrochemical reactions between electrodes and electrolyte. Fig. 3.3 clearly illustrates the faradaic charge/discharge processes of a pseudocapacitor. The redox couple (O_p/R_p) at the positive electrode is oxidized in the charge process and reduced in the discharge process; while the redox couple (O_n/R_n) at the negative electrode is reduced in the charge process, and oxidized in the discharge process. [53] The faradaic processes occurring between the electrode and electrolyte rely on the material of electrode. The faradaic processes can be reversible adsorption (such as adsorption of hydrogen on the surface of platinum or gold), redox reactions of transition metal oxides (for example, ruthenium oxide, manganese dioxide, nickel oxide, iron oxide, or cobalt oxide), or reversible electrochemical doping/dedoping in conducting polymers (such as PANI, polypyrrole, or polythiophene) or heteroatom (nitrogen, boron, oxygen and sulfur) doped materials. [54] The battery-like redox reactions make pseudocapacitors exhibiting much higher specific capacitance and energy density than the EDLCs. Conway *et al.* reported that the capacitance of a pseudocapacitor can be 10-100 times higher than the electrostatic capacitance of an EDLC. [55] However, similar to batteries, pseudocapacitors often suffer from lower power density and bad stability during charge/discharge cycle. The former disadvantage is attributed to the longer time needed for faradaic processes compared to non-faradaic processes; and the latter disadvantage is due to volumetric changes of the electrode materials caused by the insertion and removal of ions during charging and discharging.

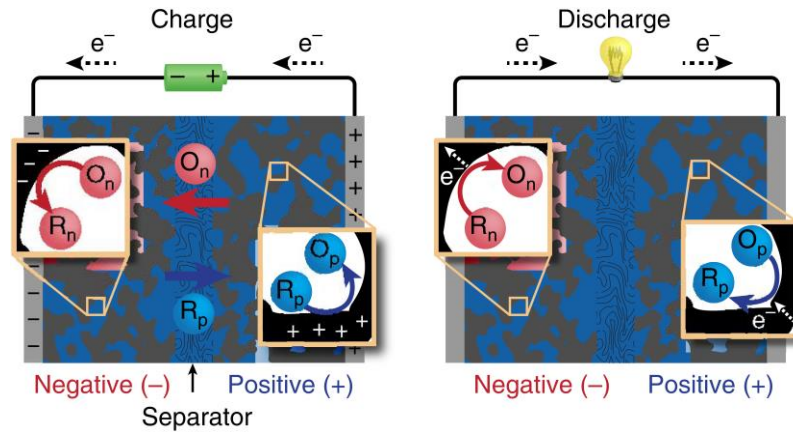


Fig. 3.3 Microscopic charge/discharge processes of a pseudocapacitor. Reused with the permission of Creative Commons CC BY. Copyright belong to Springer Nature 2015. [53]

Producing hybrid supercapacitor is an attractive way to combine a capacitive EDLC (power source) with a faradic pseudocapacitor (energy source). [33] An appropriate combination can not only achieve synergic effect, but also extend the voltage stability window. According to the configuration of electrode, hybrid supercapacitors can be divided into composite hybrids, asymmetric hybrids and battery-like hybrid supercapacitors. [56]

Composite hybrid supercapacitors usually use composites of faradic materials (conducting polymer or transition metal oxide) and carbonaceous materials (activated carbon, carbon nanotube, graphite, etc.) as electrodes. Composite hybrid supercapacitors show higher capacitance than EDLC due to the contribution of pseudocapacitance and higher power density than pseudocapacitance due to the carbonaceous component. Besides, the carbonaceous materials can increase the accessible surface area, supply a conductive channel for pseudocapacitive materials, and limit the ion diffusion-induced volume changes of faradic materials. Therefore, composite hybrid supercapacitors illustrate better cycle stability than the corresponding pseudocapacitors. [57, 58]

In asymmetric hybrid supercapacitors, one electrode is a capacitive carbonaceous material and the other electrode is a faradaic material. This strategy can also combine the high energy and power density of pseudocapacitors and the cyclic stability of EDLCs. Moreover, the asymmetric design can increase the cell voltage window, therefore further enhance the energy and power densities. Additionally, since

conducting polymers in the negatively doped state show worse stability than those in the positively doped state, they are usually used as the positive electrode in an asymmetric hybrid capacitor. For the design of asymmetric capacitors, the positive and negative electrode materials should exhibit comparable rate performance. In an asymmetric device, even though the specific capacitance values of the positive and negative electrodes (C_p and C_n , respectively) are different, the stored amount of charge in the positive and negative electrode should be balanced:

$$C_n \cdot m_n \cdot \Delta V_n \approx C_p \cdot m_p \cdot \Delta V_p \quad (3.5)$$

where m_n and m_p are the masses of the active electrode materials, ΔV is working voltage window, and C_n and C_p represent the specific capacitances of negative electrode and positive electrode, respectively. Brousse *et al.* have assembled an asymmetric supercapacitor cell using activated carbon as positive electrode and manganese oxide as negative electrode. This cell showed a specific energy density of 10 Wh kg⁻¹, a specific power density of 16 kW kg⁻¹, a R_s of lower than 1.3 Ω cm², and good cycle stability with only 12.5 % capacitance loss after 195000 cycles. [59] Salinas-Torres *et al.* prepared an asymmetric capacitor using activated carbon as negative electrode and activated carbon fiber/PANI composite as positive electrode. This capacitor showed an energy density of 20 Wh kg⁻¹, a power density of 2.1 kW kg⁻¹, and excellent cycle stability with 90 % retention over 1000 cycles. [60]

A battery-like hybrid supercapacitor usually consists of a supercapacitive positive electrode, a lithium ion battery-type negative electrode, and a Li salt-contained organic electrolyte as shown in Fig. 3.4. This type of supercapacitor can combine high capacitance and energy density of battery-type electrode, fast power density of supercapacitive electrode, and the wide voltage window of the organic electrolyte. Amatucci *et al.* proposed an activated carbon//Li₄Ti₅O₁₂ (positive//negative) asymmetric supercapacitor. This hybrid supercapacitor showed a high energy density of 20 Wh kg⁻¹ and good cycle stability with only 10-15 % capacitance loss after 5000 cycles. [61] Zhang *et al.* assembled a battery-type hybrid supercapacitor by using iron oxide/graphene nanocomposite as negative electrode and three-dimensional graphene as positive electrode. The final cell exhibited a high energy density of 147 Wh kg⁻¹ under a power density of 150 W kg⁻¹. [62]

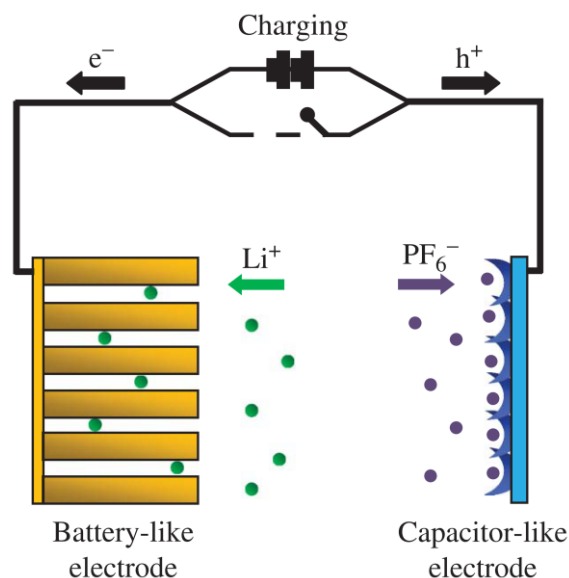


Fig. 3.4 Schematic drawing of a battery-type asymmetric supercapacitor. Open access, copyright belong to Taylor and Francis Group, LLC. [63]

3.2. Polyaniline

3.2.1. Structure and properties

Intrinsically conducting polymers have been extensively investigated since the discovery of polyacetylene (PA) in 1977. The most commonly used conducting polymers contain PA, polyaniline (PANI), polypyrrole (PPy), and polythiophene (PTh) and its derivatives such as poly(3,4-ethylenedioxythiophene) (PEDOT). It can be seen from the molecular structures illustrated in Fig. 3.5 that conducting polymers own highly π -conjugated polymeric molecular chains. [64, 65] The usual band gap between the highest occupied molecular orbitals and the lowest unoccupied molecular orbitals of polymers is about 10 eV, but the π -conjugation can reduce the band gap of conducting polymer to 1-3 eV; therefore they show conductivity. For practical application, the pristine states of conducting polymers usually need to be doped by oxidation or reduction, which results in positively charged polymer (*p*-doped) and negatively charged polymer (*n*-doped), respectively. It is worth noting that PANI, PPy and some other conducting polymers can only be *p*-doped, because the potentials required for *n*-doping is too negative compared to the reduction potential limit of electrolytes. PTh

and its derivatives are promising materials for *n*-doping. After doping, the conductivity of conducting polymers can increase by several orders of magnitude. [65] Besides conductivity and plastic properties, conducting polymers also show highly reversible redox behavior. Therefore, they are used in various practical fields, such as electric, electronic, sensor, supercapacitor, electromagnetic device, etc.

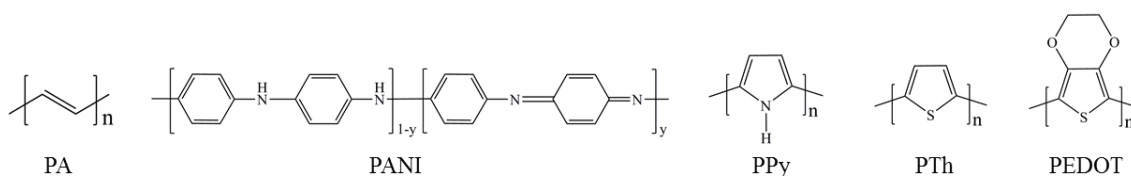


Fig. 3.5 Chemical structure of polyacetylene (PA), polyaniline (PANI), polypyrrole (PPy), polythiophene (PTh) and poly(3,4-ethylenedioxythiophene) (PEDOT).

Among the conducting polymers, PANI is the most attractive one due to its low cost, easy to synthesis, promising electrochemical behavior and thermal stability. The monomer (aniline) is inexpensive and can be produced from benzene or extracted from oil and coal. [66] Moreover, compared to other conducting polymers, PANI own unique redox states and doping mechanisms. The states of PANI change with the ratio of quinoid to benzenoid units in the molecular structure, namely y to $1-y$ in the PANI structure shown in Fig. 3.5. The redox reactions between different state of PANI, i.e. fully reduced state (leucoemeraldine), partly oxidized states (protoemeraldine, emeraldine and nigraniline), and fully oxidized state (pernigraniline), were illustrated in Fig. 3.6 (a). [67, 68] Fig. 3.6 (b) shows the protic doping and dedoping between the insulating emeraldine base and conductive emeraldine salt. The pH value of the solution decides not only the extent of redox reaction but also the conductivity of PANI. Additionally, the color of PANI at different states is different. Leucoemeraldine is transparent; undoped emeraldine is blue; doped emeraldine is green; and pernigraniline is dark violet. Therefore, PANI can also be used for electrochromic devices and displays. [69]

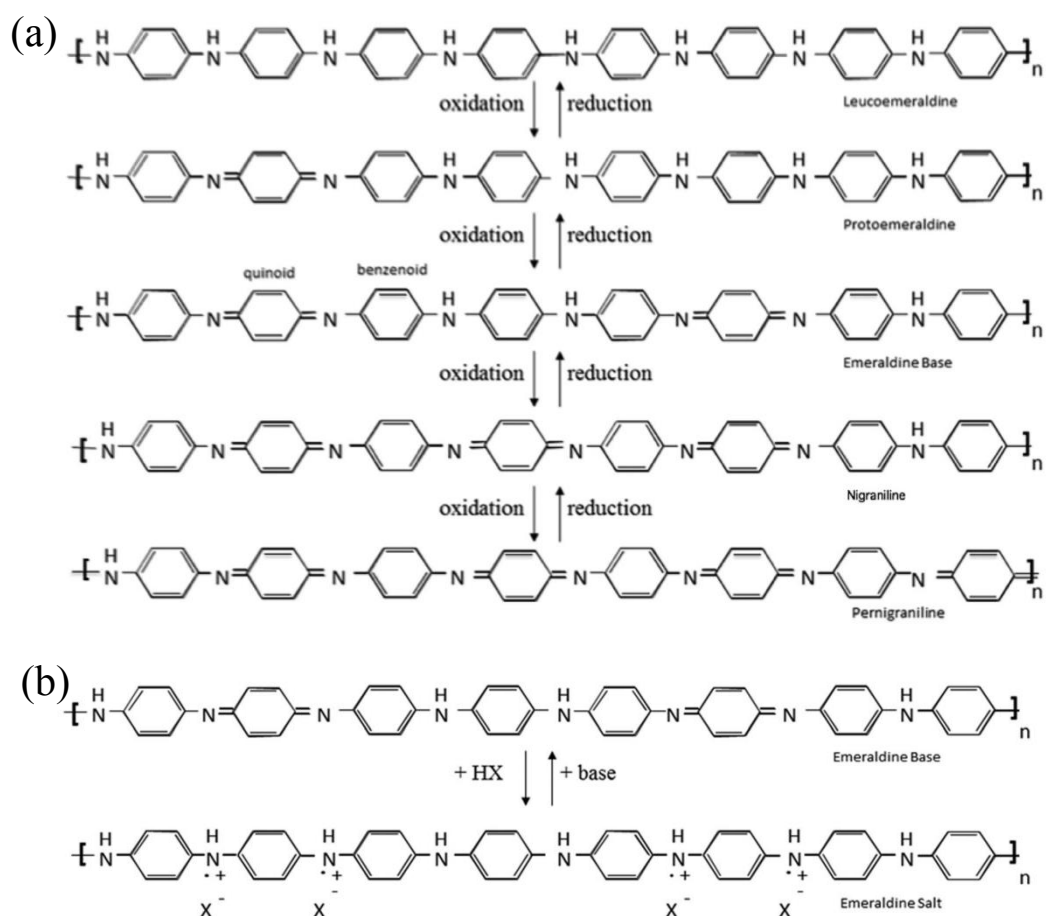


Fig. 3.6 Structures of different states of PANI. Reuse with permission from Royal Society of Chemistry. [66]

3.2.2. Synthesis

PANI can be produced by various methods, such as chemical oxidative polymerization, [70] electrochemical synthesis, [71] interfacial polymerization, [72] ultrasonic irradiation polymerization, [73] emulsion polymerization, [74] etc. Among them, chemical oxidative polymerization is the most extensively used method and is suitable for mass production of PANI. Fig. 3.7 illustrates the polymerization of aniline with ammonium peroxydisulfate (APS) as oxidant in an acidic aqueous media. This polymerization resulted in protonated emeraldine salt and some by-products (sulfuric acid and ammonium sulfate). The most commonly used protic acid is volatile hydrochloric acid (HCl), since the excess acid can be removed under vacuum. After polymerization, the obtained emeraldine salt can be deprotonated by alkalis into emeraldine base and then treated by excess dopant. Colak *et al.* examined copper

chloride (CuCl_2), aluminium chloride (AlCl_3), and various organic and protonic acids as dopant for PANI by re-doping the PANI salt, which has been prepared by chemical oxidative polymerization of aniline in HCl solution followed by dedoping using ammonium hydroxide (NH_4OH). [75] Moreover, the electrochemical property and morphology of PANI depend on the nature of aniline and the polymerization conditions, i.e. the presence of additives (such as surfactants and colloidal stabilizers), templates, chemical nature of oxidant, the ratio of monomer to dopant, the concentration of dopant, and reaction temperature. [68] Carswell *et al.* have synthesized PANI with controllable nanostructure, from spheres to wires to flat films, by using adsorbed surfactants as templates. [76] Wang *et al.* successfully produced PANI nanostructures with different morphologies, such as fibers, micro-mats and disks, by changing the synthesis parameters. [77] Fig. 3.8 illustrates the schematic of three different morphologies of PANI. The granular morphology is usually formed by precipitation polymerization with strong oxidant, high aniline concentration and high pH value. The nanofiber morphology is a one-dimensional structure with a diameter of around tens of nanometres. The nanotube morphology also owns a one-dimensional structure, but a template is necessary during the polymerization in order to form the internal cavity. [78] Compared to the granular morphology, nanofiber and nanotube morphologies endow PANI with higher specific surface area. Additionally, some researchers added previously synthesized PANI as the seed in the polymerization of aniline, which is called as seeding polymerization. The final morphology of the obtained PANI nanofiber depends on the acid, the amount of aniline, type of seed, and the solvent. [79]

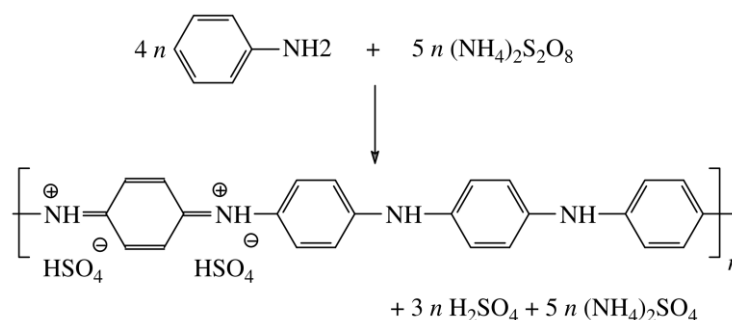


Fig. 3.7 Oxidative polymerization of PANI using APS as oxidant in an acidic medium. Reprinted with the permission from American Chemical Society. [80]

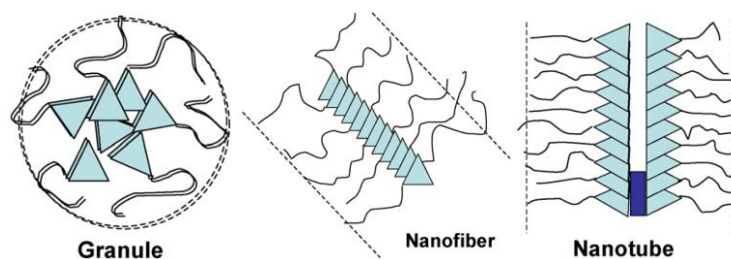


Fig. 3.8 Schematic illustration of the formation of PANI with different morphologies. Reuse with the permission from Elsevier. [78]

Electrochemical synthesis of PANI is an attractive environmental friendly method. Oxidant is not necessary in this method, thus the PANI produced by electrochemical synthesis usually own higher purity than the PANI obtained by the chemical oxidative polymerization. Moreover, electrochemical polymerization can produce PANI directly on the substrate, which means it is suitable for the fabrication of binder-free supercapacitor electrodes. [81, 82] Electrochemical synthesis can be realized by various ways, such as cyclic voltammetry, galvanostatic electrolysis and potentiostatic electrolysis, etc. Both of cyclic voltammetry and galvanostatic electrolysis require accurate control of potential, thus usually use three-electrode cells. Potentiostatic electrolysis can use either three-electrode cells or two-electrode cells. For all methods, the synthesized PANI is deposited on the working electrode (anode, usually an inert electrode using metal, conducting glass, or carbonaceous material) in an aqueous protic acid electrolyte. PANI produced by cyclic voltammetry own more disordered chains compared to the PANI produced by galvanostatic and potentiostatic electrolysis. Additionally, PANI produced by potentiostatic or galvanostatic electrolysis is usually in the conducting doped state. Whereas, the PANI obtained by cyclic voltammetry might be in the insulating base state, since the deposited PANI changes between the insulating base state and conductive doped state during cyclic voltammetry. Besides the cell structure and type of electrochemical method, synthesis parameters, such as dopant, template, temperature, reaction time, pH value of electrolyte, monomer concentration, current density, and potential can also influence the properties of produced PANI. Zhou *et al.* found that the addition of methanol in electrochemical synthesis of PANI favored the formation fibrillar morphology. [83] Kan *et al.* reported that adding ethanol increased the reaction rate and enhanced the redox reaction of the electrochemical

polymerization of aniline. [84] Additionally, the dilute polymerization uses lower concentration of aniline than the conventional chemical polymerization. Chiou *et al.* successfully produced PANI nanofibers by the dilute polymerization without any specific templates, such as surfactants, organic solvents, oligomers, etc. [85]

Interfacial polymerization is a simple and effective method to produce PANI with fibrillar morphology. The obtained PANI nanofibers can own an average diameter of smaller than 100 nm. In this method, the oxidative polymerization of PANI only occurs in the interface between two immiscible solvents. In the case of an organic solvent/aqueous solvent immiscible reaction system, aniline is in the organic solvent, and dopant and oxidant are in the aqueous solvent. Additionally, different to the chemical oxidative polymerization and electrochemical polymerization, the dopants used in interfacial polymerization are organic dopants. Fig. 3.9 compares the PANI synthesis process in a chemical polymerization and in an interfacial polymerization. In the interfacial polymerization, the newly produced hydrophilic PANI nanofibers tend to move away from the interface, thus further growth of PANI can be prevented. However, in a conventional chemical polymerization, the PANI nanofibers produced in the early stage will subsequently grow into agglomerated PANI particles, since they are still exposed to aniline and oxidant. Besides PANI nanofibers, interfacial polymerization can also obtain PANI with other morphologies. Chen *et al.* have produced PANI with fine nanorod-, particle- and bud-like structures under different ratio of dopant (salicylic acid) to aniline. [86]

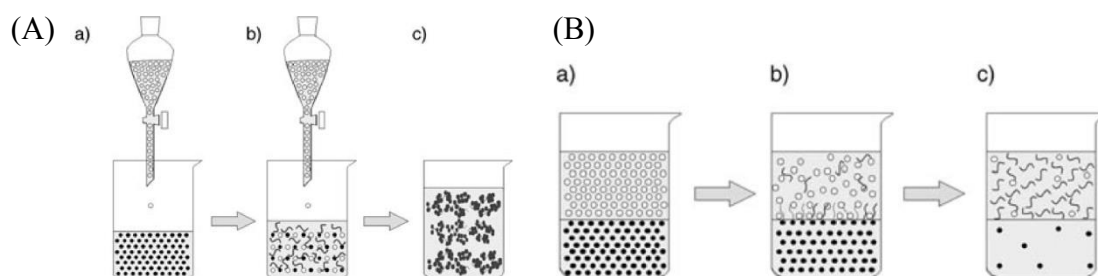


Fig. 3.9 Schematic diagrams of PANI produced by (A) conventional chemical polymerization method and (B) interfacial polymerization method. The solid and open circles represent aniline and oxidant, respectively. Reuse with the permission from John Wiley and Sons. [87]

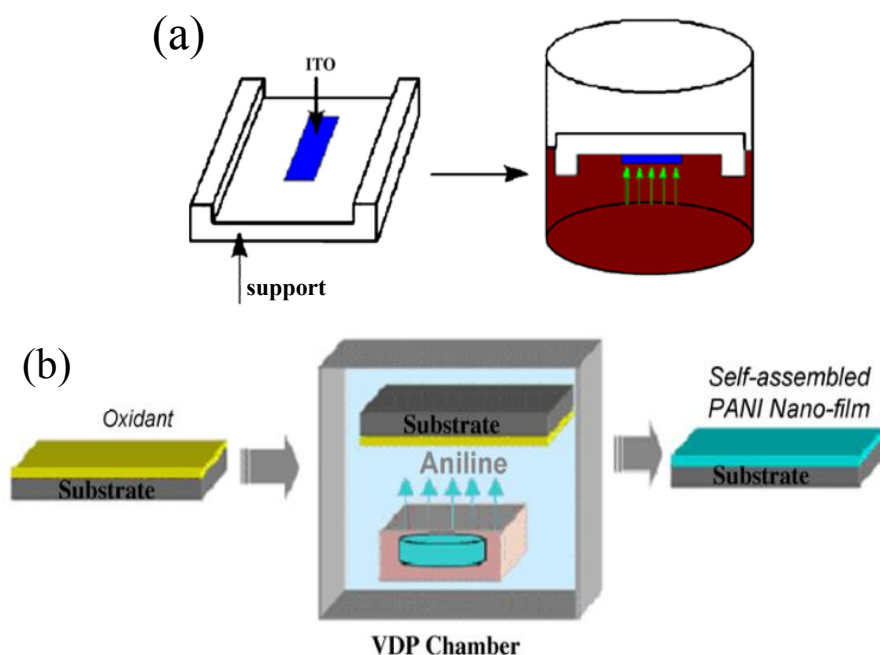


Fig. 3.10 Schematic diagrams of PANI synthesis by two kinds of self-assembling polymerization methods: (a) using ITO as substrate; [88] (b) using a polymeric substrate. [89] Reuse with permissions from Elsevier.

Some other synthesis methods of PANI have also been reported. In a direct emulsion polymerization process, PANI is polymerized in an emulsion of water and a nonpolar or weakly polar organic solvent (such as xylene, chloroform, or toluene) with the presence of oxidant and protic acid. In an inverse emulsion polymerization, aniline aqueous solution is emulsified in a nonpolar organic solvent. Then the polymerization is initiated by an oil-soluble initiator, for example the ammonium persulfate or benzoyl peroxide. [70] Some researchers have synthesized PANI by microemulsion method, which is done in a micro-heterogeneous system with large interfacial area. [90, 91] The direct and inverse emulsion polymerization methods are easy to be controlled and can achieve high reaction rate and PANI product with high molecular weight. [92] Zhou *et al.* prepared PANI with controlled morphology and crystallinity by varying the water content in the reverse microemulsion. [93] Another synthesis method of PANI is ultrasonic irradiation polymerization. The polymerization effect of ultrasound irradiation is derived from acoustic cavitation, namely the formation, growth, and implosive collapse of bubbles in the liquid. Lu *et al.* found that this method can produce PANI nanotubes and nanofibers by using common mineral acids or organic acids and without the addition of dopant and template. [94] Fig. 3.10 illustrates two kinds of self-

assembling polymerization of PANI. In Fig. 3.10 (a), indium tin oxide (ITO) was used as a substrate; PANI film was assembled on the ITO with addition of oxidant (APS) in an aqueous solution. [88] In Fig. 3.10 (b), aniline was in the vapor phase and assembled into PANI thin films on the polymeric substrate, which contained oxidant (iron chloride), camphorsulfonic acid, and Fe (*p*-toluene sulfonate)₃. [89]

3.2.3. Supercapacitor application

Due to the multiple redox states and high capacitance value, PANI is a promising electrode material for supercapacitor. When PANI changes its state, a large surface charge potential can be created. Fig. 3.11 shows a typical cyclic voltammogram and a discharge curve of a supercapacitor using PANI as electrodes. Obviously, there are three pairs of redox reactions in the cyclic voltammogram. With the potential increasing, PANI changes from insulating leucoemeraldine to conductive protonated emeraldine, and then to pernigraniline. It is noteworthy that the electrochemical performance of a faradic material in practical testing is dominated by pseudocapacitive behavior but also shows EDLC behavior. As shown in Fig. 3.11, the regions marked by purple curves are attributed to the contribution of EDLC, and the green regions are due to the pseudocapacitive behavior. Furthermore, when PANI is used as supercapacitor electrode, the electrolyte should be able to supply sufficient protons in order to enable a long-term electrochemical cycle. Additionally, the potential range for a cyclic voltammogram of PANI electrode in an aqueous electrolyte is usually set at 0.8-1.0 V. A potential window of lower than 0.6 V has no practical interest. [17]

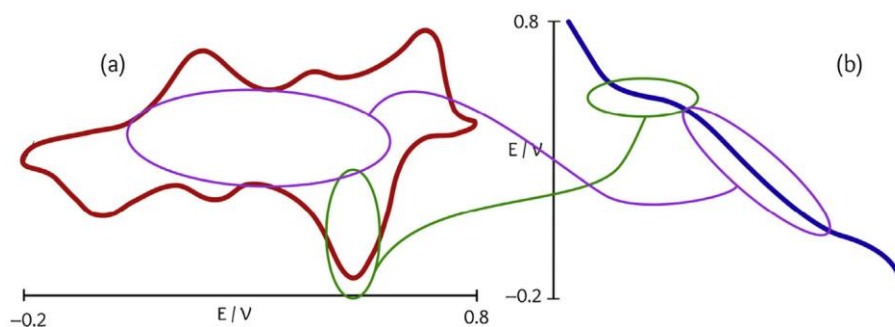


Fig. 3.11 (a) Typical cyclic voltammogram and (b) discharge profile of a PANI electrode. Reuse with the permission of Elsevier. [17]

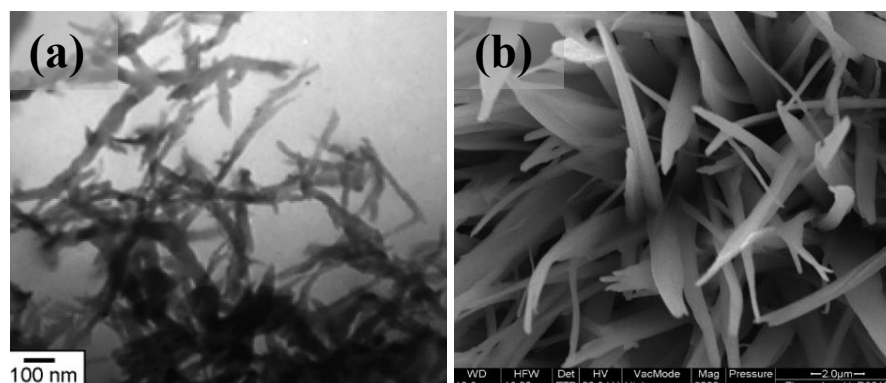


Fig. 3.12 SEM images of (a) PANI nanofibers, reuse with permission from Elsevier [95]; and (b) PANI nanobelts, reuse with the permission from American Chemical Society [96].

The main influencing factors for the capacitive performance of a PANI electrode contain the synthetic route and method, morphology of PANI, the amount and type of binder, and the thickness of electrode. [65] Bian *et al.* reported that some dopants were covalently attached to PANI chains and cannot be electrochemically removed, therefore blocked the capacity of PANI. [97] Kuang *et al.* found that polymerization temperature changed the morphology of the produced PANI and affected the specific capacitance and cycle stability. [98] The morphology of PANI is tightly connected with the accessible surface area for charging and discharging. Therefore, PANI with various nanostructured morphology have been developed and used as supercapacitor electrode, such as PANI nanofibers, PANI nanoribbons, PANI nanotubes, PANI nanobelts, PANI nanosheets, PANI nanorice, PANI nanocapsules, PANI nanobrushes, etc. Zhou *et al.* reported that compared to granular or flake-like PANI, nanofibrous PANI has larger accessible surface area and better electronic and ionic conductivity, thus own higher capacitance. Mi *et al.* have synthesized PANI nanofibers by a template method, in which ferric chloride and ammonium persulfate (APS) were used as oxidant, and methyl orange/ferric chloride was used as seed template. [95] Fig 3.12 (a) shows the SEM image of the obtained PANI nanofibers. The PANI presented a high specific capacitance of 428 F g^{-1} at a current density of 2 mA cm^{-2} , high rate capability (a capacitance retention of 83 % at 5 mA cm^{-2}) and good electrochemical reversibility. Li *et al.* successfully prepared PANI nanobelts, whose SEM image is shown in Fig 3.12 (b),

by electrochemical polymerization. This PANI showed a high specific capacitance of 873 F g^{-1} at 10 mV s^{-1} and good stability over 1000 cycles. [96]

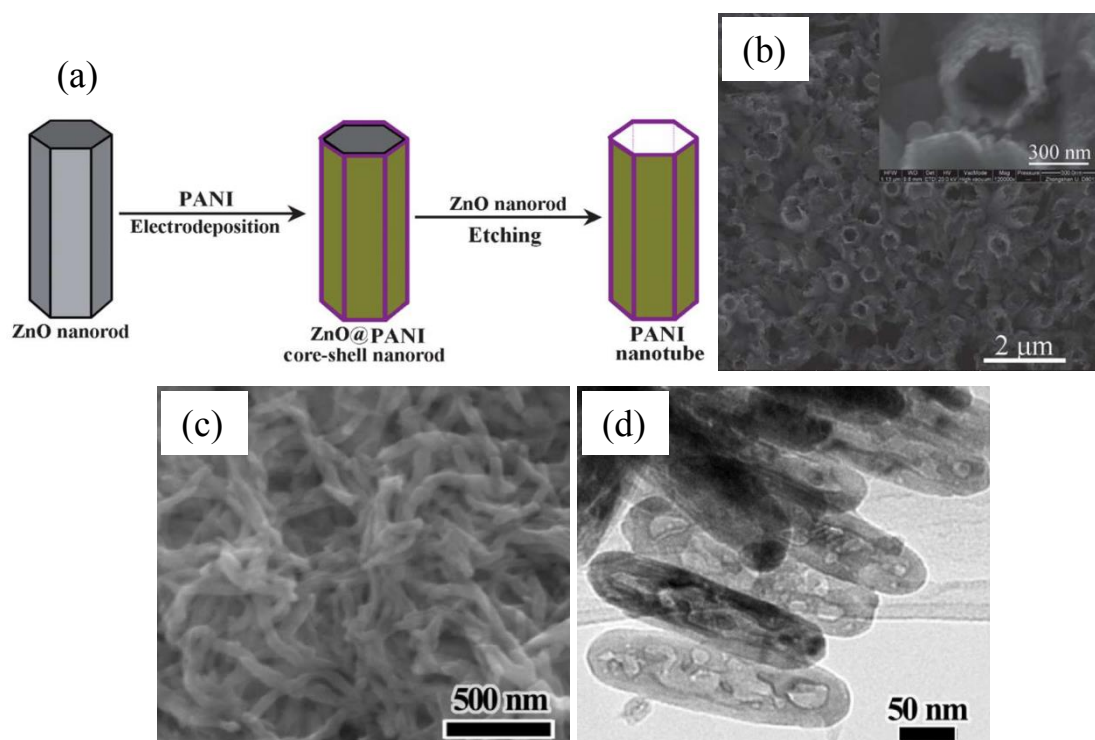


Fig. 3.13 (a) The synthesis illustration and (b) SEM image of PANI nanotube, reuse with permission from Royal Society of Chemistry [99]; (c) SEM and (d) TEM images of PANI nanocapsules, reuse with permission from Elsevier [100].

The practical specific capacitance of PANI nanofibers is much lower than the theoretical specific capacitance (1200 F g^{-1}). It is because some surface is inaccessible in the timescale of the charge/discharge process. [66] Preparing a mesoporous/microporous structure can not only increase surface area, but also facilitate transfer of ions, thus enhances the capacitance and rate capability. Liu *et al.* have synthesized porous PANI by in-situ oxidative polymerization of aniline using APS as oxidant in the presence of an anionic surfactant (sodium dodecyl sulfate). [101] This porous PANI owned much higher supercapacitance than the non-porous PANI. Among the nanostructured PANIs, PANI nanotube and PANI nanocapsule own porous structures. Fig. 3.13 (a) and (b) show the synthesis route of PANI nanotubes via a zinc oxide (ZnO) nanorod template-directed electrochemical method, and the SEM of the

obtained PANI nanotubes, respectively. [99] The nanotube structure enhanced the transport ability of electroactive ions; therefore the PANI exhibited an outstanding cycle stability and a good rate capability (specific capacitance decayed only about 21.2 wt.% when the scan rate increase from 5 mV s⁻¹ to 50 mV s⁻¹). Yang *et al.* reported a facile template-directed interfacial polymerization method and prepared hollow PANI nanocapsules with holes on the wall. The SEM and TEM of the obtained PANI nanocapsules are illustrated in Fig. 3.13 (c) and (d), respectively. [100] The PANI nanocapsules exhibited a high specific capacitance of 502 F g⁻¹ at a current density of 5 mA cm⁻² and excellent cycle stability.

Some researchers have combined PANI with transition metal oxides in order to develop the electrochemical performance. Transition metal oxides have high theoretical specific capacitance, but suffer from many drawbacks. Ruthenium oxide (RuO₂) is the most promising transition metal oxide since it can store charge reversibly, but it is too expensive to commercialize. There are some cheap alternatives for RuO₂, such as manganese oxide (MnO₂), iron oxide (Fe₃O₄), stannic oxide (SnO₂), etc. But their electrical conductivities are low. Deshmukh *et al.* prepared PANI/RuO₂ composite thin films by a chemical bath deposition method. This composite showed specific capacitances of 830 F g⁻¹ at 5 mV s⁻¹ and 255 F g⁻¹ at 100 mV s⁻¹, and good cycle stability (the specific capacitance at 100 mV s⁻¹ decreased by 15 % after 5000 CV cycles). [102] Li *et al.* produced RuO₂/PANI composites by electrochemically depositing PANI on a tantalum substrate and then electrodepositing RuO₂ on the PANI. This RuO₂/PANI composite owned a specific capacitance of 474 F g⁻¹ at a scan rate of 50 mV s⁻¹ and decayed only 12 % after 1000 CV cycles. [103] Hu *et al.* prepared a PANI/SnO₂ nanocomposite, in which the SnO₂ nanoparticles were embedded within the netlike PANI. This composite had a specific capacitance of 305.3 F g⁻¹ at a current density of 5 mA cm⁻² and decayed only 4.5 % capacitance after 500 cycles. [104] Jiang *et al.* produced PANI/MnO₂ coaxial nanofibers composites. The MnO₂ floccules supplied high specific surface area, and the PANI nanofibers served as backbone and conductive pathway. The optimal PANI/MnO₂ in their study showed a high specific capacitance of 383 F g⁻¹ at 0.5 A g⁻¹ and good cycle stability with 75.5 % capacitance retention over 2000 cycles. [105]

Composites of PANI and other conducting polymers have also been studied for the application in supercapacitor electrode. Poly(3,4-ethylenedioxythiophene) (PEDOT) is an attractive conducting polymer since it is highly conductive, environment friendly, and chemically stable. Polystyrenesulfonate (PSS) is often used to increase the water-dispersion of PEDOT, but the addition of PSS sacrifices the electrical conductivity of PEDOT. Dipali *et al.* used silver nanowire (AgNW) to improve the conductivity of PEDOT:PSS and developed AgNW-PEDOT:PSS/PANI hybrid nanostructures. They deposited a thin layer of AgNW-PEDOT:PSS firstly on a stainless steel substrate by a dip coating technique and then electrodeposited PANI on the pre-coated substrate. The obtained AgNW-PEDOT:PSS/PANI nanostructure showed a large specific capacitance of 643 F g^{-1} at 10 mV s^{-1} and still retained 85.87 % capacitance after 1000 cycles. [106] Polypyrrole (PPy) is another commonly used conducting polymer. PANI-based electrodes usually work in acidic electrolytes, while PPy-based electrodes are usually used with neutral electrolytes. Therefore, the combination of PANI and PPy can extend the pH range of electrolyte. Mi *et al.* prepared core-shell PPy/PANI composites by in-situ chemical polymerization of aniline on the surface of PPy nanotubes. The resulting PANI/PPy composite presented a specific capacitance of 416 F g^{-1} in sulphuric acid (H_2SO_4) and a specific capacitance of 291 F g^{-1} in potassium chloride (KCl). [107] More recently, Lei *et al.* developed a new one-step triple-phase interfacial synthesis method to produce PANI-coated PPy composite, which showed a high specific capacitance of 348.5 F g^{-1} but bad cycle stability with a 48.6 % loss of capacitance after 100 cycles. [108]

Besides the binary nanocomposites, ternary nanocomposites have also been investigated to develop the electrochemical performance of PANI. Xia *et al.* reported a two-step method to producing nanostructured graphene/ Fe_2O_3 /PANI composite. The obtained ternary composite showed a high specific capacitance of 638 F g^{-1} at a scan rate of 1 mV s^{-1} , which is much higher than the 58 F g^{-1} of the pristine PANI, and excellent electrochemical stability with 92 % retention of specific capacitance after 5000 cycles. [109] Li *et al.* developed an interesting and efficient strategy to grow cobalt oxide (Co_3O_4) on the graphene by employing PANI as coupling linker. The synthesis procedure is illustrated in Fig. 3.14 (a) and (b). The as-prepared ternary nanocomposites have well-defined two-dimensional morphologies and outstanding

electrochemical performance (in Fig. 3.14 (c)). [110] Han *et al.* produced 70 % MnO₂ nanorods intercalated graphene oxide/PANI ternary composites, which showed a high specific capacitance of 512 F g⁻¹ at a current density of 0.25 A g⁻¹ and outstanding cycle stability with 97 % capacitance retention after 5000 cycles. [111]

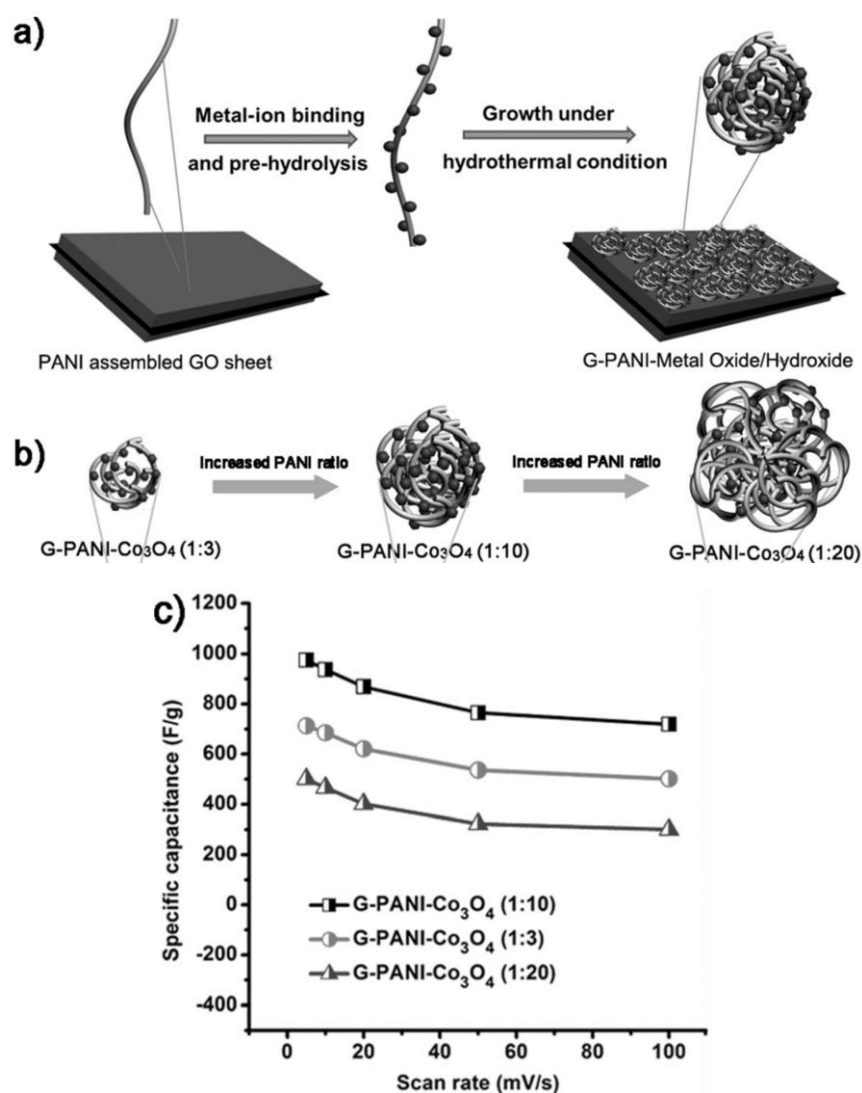


Fig. 3.14 Schematic illustration of (a) the synthesis of graphene/PANI/Co₃O₄ nanocomposite and (b) detailed growth of PANI/Co₃O₄ particles; (c) the specific capacitance of the obtained nanocomposites. Reuse with the permission from John Wiley and Sons. [110]

Similar to other conducting polymers, PANI suffers from bad electrochemical stability due to the volume change during charge/discharge cycling. In order to overcome this drawback, some researchers proposed chemical modification of PANI. Sivakkumar *et al.* successfully modified PANI into poly(*N*-methylaniline) (PNMA), in

which the proton exchange sites were blocked by the methyl groups. The PNMA owned higher redox activity and lower risk of degradation compared to PANI. [112] Another effective strategy to improve the cycle stability of PANI is producing carbon-based PANI composite. This composition can combine the outstanding conductivity and stability of carbonaceous materials with the high faradaic-capacitance of PANI. [66] The researches about the development of carbon-based PANI composites for supercapacitor electrode will be discussed in the section 3.3.

Another strategy to improve the electrochemical stability of PANI is designing asymmetric supercapacitors using PANI as the positive electrode. [113] The negative electrode can be carbonaceous materials or transition metal oxides. Mak *et al.* reported an asymmetric supercapacitor using PANI nanofibers as positive electrode, and vanadium pentoxide (V_2O_5) nanofibers as negative electrode. The PANI/ V_2O_5 asymmetric device showed a specific capacitance of 58 F g^{-1} at 0.2 A g^{-1} , which was higher than the 39 F g^{-1} of a $V_2O_5//V_2O_5$ symmetric supercapacitor. And the PANI/ V_2O_5 supercapacitor had long cycle life with around 73 % capacitance retention after 2000 cycles. [114] Heydari *et al.* synthesized PANI on the carbon cloth (CC) substrate and assembled an all-solid flexible asymmetric supercapacitor. PANI-CC and activated carbon were used as positive and negative electrodes, respectively; and H_2SO_4 -PVA gel was used as electrolyte. This asymmetric supercapacitor performed a good capacitance of 261 F g^{-1} at 1 A g^{-1} and great cycle stability (18 % decay after 5000 cycles). [115] Bivio *et al.* assembled PANI/carbon nanotube symmetric and asymmetric flexible supercapacitors as shown in Fig. 3.15. The PANI/carbon symmetric supercapacitor and the asymmetric supercapacitor using PANI/carbon nanotube as positive electrode and carbon black as negative electrode both showed good cycle stabilities, but the specific capacitance of the asymmetric supercapacitor (1566 F g^{-1} at 0.25 A g^{-1}) was higher than that of the symmetric supercapacitor (1275 F g^{-1} at 0.25 A g^{-1}). [116]

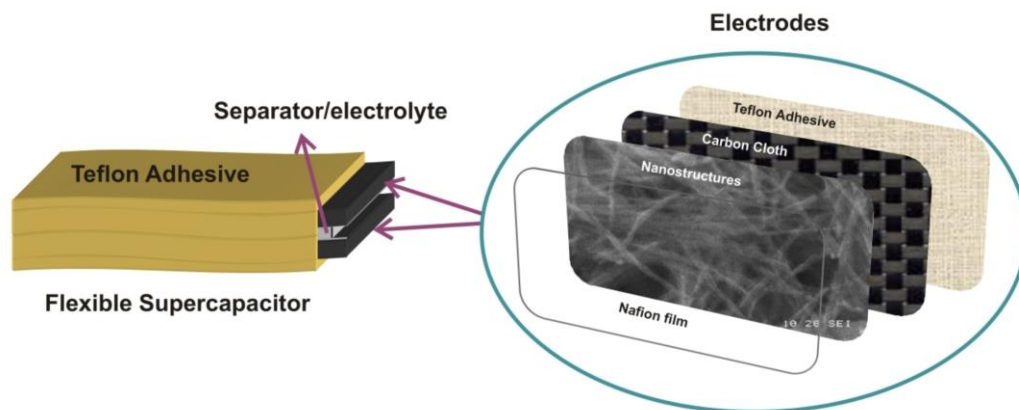


Fig. 3.15 Schematics of a flexible supercapacitor cell. Reuse with the permission from Elsevier. [116]

3.3. Carbon-based PANI composite

3.3.1. Preparation methods and electrochemical performance

Using carbon-based PANI composites as supercapacitor electrode is aimed to obtain synergistic effects, i.e. combine the high conductivity, large specific surface area, good mechanical stability and high power density of carbonaceous materials with the high energy density of PANI. Moreover, the carbonaceous materials can serve as a structural support for the PANI and allow room for the swelling and shrinking of PANI, therefore enhance the electrochemical cycle stability. [126] Various carbonaceous materials have been used to produce carbon-based PANI composites. Among them, activated carbon, carbon nanotube (CNT), and graphene have been most extensively investigated. Activated carbon own high specific surface area and moderate cost. CNT has excellent electrical conductivity and chemical stability, but is expensive, hard to purify, and own lower surface area than graphene. Graphene own unique two-dimensional sp^2 -hybridized carbonaceous nanostructure, therefore show larger specific surface area than most carbonaceous materials, high conductivity, excellent mechanical property, and a broad electrochemical window. [117] Graphene itself can be produced by various methods, such as mechanical exfoliation, epitaxial growth by chemical vapor deposition, oxidizing graphite followed by reduction, unzipping CNT, etc. Among them, the oxidation-reduction is the most commonly used method, since it is simple and suitable for mass production. Up to now, many synthesis methods of carbon-based PANI

composites have been reported. Here, the most commonly used four methods, namely in-situ polymerization, vacuum filtration, electrodeposition and chemical vapor deposition, are discussed in following text.

In-situ polymerization is the most widely used method to produce PANI/carbonaceous material composites. The main drawback of this method is the poor dispersion of carbonaceous materials in aqueous solution. In order to solve this problem, many strategies have been reported such as sonication, surface modification, preparing composites of graphite oxide (GO) and PANI followed by reducing into reduced graphite oxide (rGO)/PANI composites, and using rGO instead of graphene since some residual function groups of rGO are beneficial for its dispersion in aqueous media. [118] Mao *et al.* produced a series of surfactant-stabilized graphene/PANI composites by in-situ polymerization of aniline in the presence of surfactant (tetrabutylammonium hydroxide or sodium dodecyl benzenesulfonate)-stabilized graphene in acidic condition. The obtained composites showed high specific capacitance and good cycle stability. [119] Additionally, the carbon-based PANI composites produced by in-situ polymerization are usually powder-like; therefore, the active products need to be mixed with a binder, such as PVDF and PTFE, before the assembling of supercapacitor devices. In most cases, a conductive additive (e.g. carbon black) is also necessary to enhance the electrical conductivity in the electrode and at the interface between the electrode and substrate. [120] However, binders are non-conductive, and both of binder and conductive additive are usually electrochemically inactive. Khosrozadeh *et al.* prepared acid-treated carbon particles (TCPs) firstly, and then synthesized TCP/PANI composites by in-situ polymerization of aniline in the presence of TCP and phytic acid. The phytic acid acted as not only dopant but also crosslinker for PANI. They obtained free-standing composite films and assembled a lightweight, thin and flexible solid-state supercapacitor with a high specific capacitance of 272.6 F g^{-1} at 0.63 A g^{-1} and good cycle stability (95.7 % capacitance retention after 501 cycles). [44]

Vacuum filtration of the colloidal dispersions of CNT, graphene, graphene oxide (GO), etc. can assemble corresponding free-standing paper-like sheets. [121] This method has also been used to prepare free-standing carbon-based PANI composite films. The drawback of using as-prepared film for supercapacitor electrode is the low

accessible surface area. Yan *et al.* produced rGO paper by vacuum filtration of rGO aqueous dispersion and then prepared rGO/PANI hybrid paper by in-situ polymerization of aniline. The obtained paper-like rGO/PANI hybrid was thin, lightweight, flexible, and owned better electrochemical performance (specific capacitance of 489 F g^{-1} at 0.4 A g^{-1} and 96 % retention after 500 cycles) than the rGO paper. [122] Wu *et al.* mixed graphene colloid and PANI nanofibers aqueous dispersion, and vacuum filtered the mixture into composite film. The obtained film has a graphene-PANI-graphene sandwiched layer structure, showed good mechanical stability, high flexibility, excellent conductivity, and a good specific capacitance of 210 F g^{-1} at a current density of 0.3 A g^{-1} . [123]

Electrodeposition is a facile and straightforward method to produce carbon-based PANI composites. Moreover, the thickness of the synthesized films and the polymerization rate can be controlled by varying the synthesis parameters, such as current density, potential, content of monomer, etc. [117] Gao *et al.* have prepared reduced graphene oxide sheets/polyaniline (GNS/PANI) composites by this method. As illustrated in Fig. 3.16, the preparation process contains three main steps: synthesis of GNS; deposition of GNS on stainless steel substrate; and electrodeposition of PANI nanofibers on the GNS. The resulted GNS/PANI composites showed higher capacitance (5.16 F cm^{-2} at 10 mA cm^{-2}), better rate capability, and longer cycle life (93 % capacitance retention after 1000 charge/discharge cycles) than the pristine GNS and pristine PANI. [124] Ge *et al.* proposed a method of combining the vacuum filtration and electrodeposition together. They prepared single-walled carbon nanotube (SWCNT) film by vacuum filtration firstly, and then electrochemically deposited PANI on the obtained SWCNT film. They assembled the SWCNT/PANI film into a transparent flexible supercapacitor, which exhibited a specific capacitance of 55 F g^{-1} at a current density of 2.6 A g^{-1} . [125]

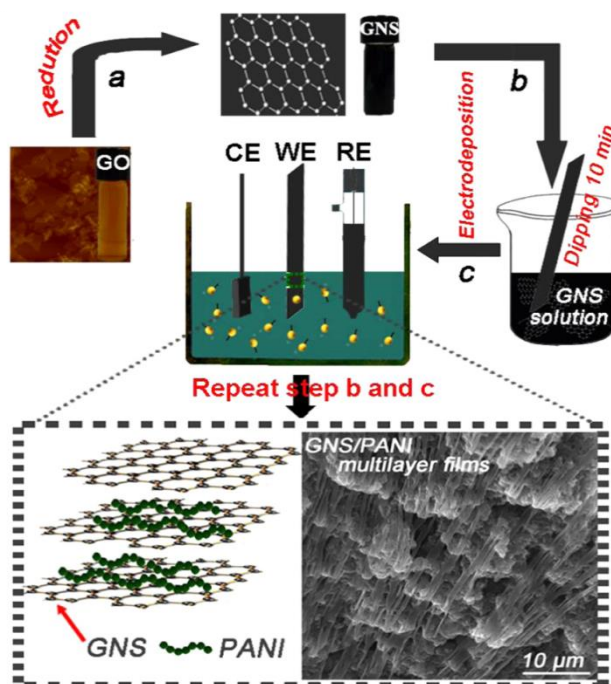


Fig. 3.16 Schematic of the preparation of GNS/PANI composites. Reuse with the permission from Elsevier. [124]

Chemical vapor deposition (CVD) can produce defect-free, fine and even graphene sheets, which do not have inter-sheet junction resistance and show high conductivity. However, a substrate is necessary to deposit the graphene sheets. The deposition is carried out at a very high temperature, and the initial graphene is in a vapor form along the targeted substrate. Dong *et al.* firstly synthesized three-dimensional (3D) graphene foams by CVD method using 3D nickel foam as template, and then in-situ polymerized aniline in the presence of the 3D graphene foam. The obtained graphene foam/PANI hybrid electrode exhibited a high specific capacitance of 346 F g^{-1} at a current density of 4 A g^{-1} but moderate cycle stability with 30 % loss of capacitance after 120 cycles. [126]

3.3.2. Strategies to improve the electrochemical properties

Up to now, many strategies have been developed to enhance the electrochemical performance of carbon-based PANI composites. Some of them are listed as follows.

Doping heteroatom, such as nitrogen (N), boron, and sulfur, etc. in the carbonaceous materials can introduce an additional pseudocapacitance. N-doping is the most

commonly used doping. It can enhance the conductivity of the carbonaceous materials and facilitate a uniform and abundant loading of PANI via serving as nucleation and anchoring sites. Yu *et al.* prepared a novel N-doped porous carbon/PANI composite, in which the N-doped porous carbon was produced using low-cost, environmental friendly and renewable wood waste. The obtained composite exhibited a high specific capacitance of 347 F g^{-1} at 2 A g^{-1} and retained 76% capacitance after 1000 cycles.

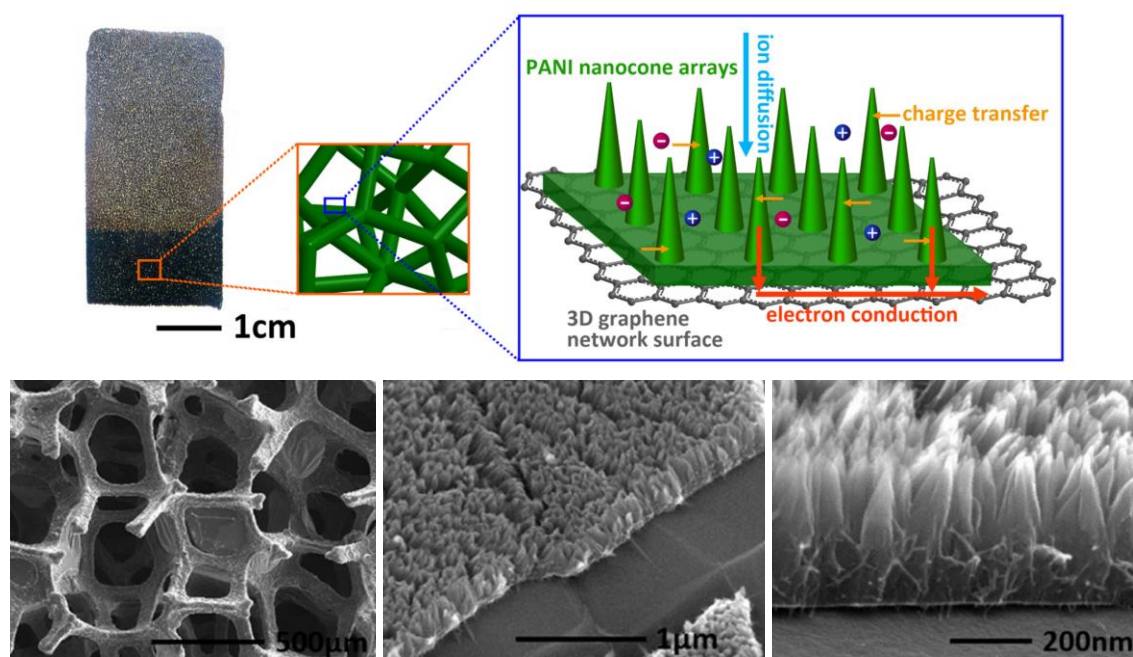


Fig. 3.17 Structural schematic and SEM images of the 3D graphene network-PANI nanocone arrays. Reuse with the permission from Elsevier. [127]

Producing PANI arrays vertical to the surface of carbonaceous materials can increase the surface area, and the obtained 3D structure of composite can increase the access sites for electron transfer and improves the rate capability. [128] Liu *et al.* fabricated 3D arrays of PANI/graphene composites by in-situ chemical oxidative polymerization of aniline in the presence of amino-functionalized graphene (AMG). The polymerization was initiated by the amino groups of AMG, and fully oriented arrays of PANI nanorods were produced at a suitable content of AMG. The prepared PANI/AMG composite showed high specific capacitance (1295 A g^{-1} at 1 A g^{-1}), low electrical resistance and excellent cycle stability (88 % capacitance retention after 1500

cyclic voltammetric cycles). [129] Yu *et al.* prepared 3D graphene network by depositing graphene on nickel foam, and then electrodeposited PANI nanocone arrays on the 3D graphene network. The morphologies of obtained materials are illustrated in Fig. 3.17. The free-standing electrode possessed specific capacitance of 751.3 F g^{-1} at 1 A g^{-1} , high rate capacitance (the capacitance at 10 A g^{-1} is 88.5 % of that at 1 A g^{-1}), and good cycle stability with 93.2 % capacitance retention over 1000 cycles of charge/discharge. [127]

Producing porous structure is another effective strategy to increase the specific surface areas and ion channels inside electrode materials. According to the size of pore, pores can be divided into micropores (<2 nm), mesopores (2-50 nm), and macropores (>50 nm). [57] Theoretically, the specific surface area of a porous material increases with the decrease of pore size. But, in practical, pores smaller than 0.5 nm are not accessible to hydrated ions; and pores smaller than 1 nm are not accessible to the solvated ions in organic electrolytes. It has been reported that the pore size for a practical supercapacitor electrode material should be in the range of 2 to 5 nm, in order to gain sufficient ion diffusion and high specific surface area. [7] Yu *et al.* prepared nanocomposites of hierarchically porous N-doped carbon (HPC) and PANI nanowire array by in-situ polymerization of aniline in the presence of HPC. The N-doping of the HPC enhanced the surface wettability and was beneficial to the growth of PANI on the internal and outer surface of the hierarchical porous HPC. The obtained HPC/PANI composite owned large accessible surface area and short ion diffusion pathway due to the interconnected meso/micropores in the 3D structure, and exhibited an excellent specific capacitance of 1080 F g^{-1} at 1 A g^{-1} in a three-electrode testing cell. The asymmetric supercapacitor, which used HPC/PANI and HPC as positive and negative electrodes, respectively, showed a high specific capacitance of 134 F g^{-1} at 1 A g^{-1} and good cycle stability with 91.6 % capacitance retention after 5000 cycles. [130] Recently, Wu *et al.* proposed a two-step self-assembling method to produce 3D porous PANI/rGO composite gels. PANI with controlled thickness was coated on GO sheets firstly by in-situ polymerization, and then the PANI/rGO was produced by reduction-assembly (Fig. 3.18 (B)). This method can avoid the pores of the composite gel being blocked by PANI as shown in Fig. 3.18 (A). The resulted PANI/rGO porous composite exhibited a high specific capacitance of 808 F g^{-1} at a current density of 53.33 A g^{-1} . [131] Fan *et al.*

produced a novel PANI hollow spheres/rGO hybrid with core-shell structure. Besides pores, the core-shell structure can also enlarge the specific surface area and shorten ion diffusion pathway. The rGO wrapped on the hollow PANI spheres can offer mechanical support for PANI and bridge the conductive pathway for individual PANI spheres. The as-prepared PANI/rGO hybrid showed a high specific capacitance of 614 F g^{-1} at 1 A g^{-1} , and retained 90 % capacitance after 500 cycles. [132]

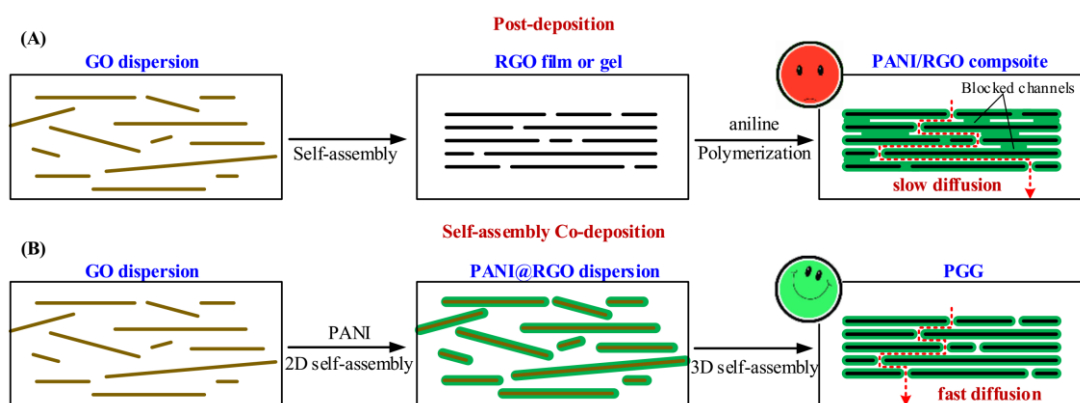


Fig. 3.18 Schematic illustration of producing PANI/rGO porous composite by (A) traditional way and (B) the method proposed by Wu *et al.* Reuse with the permission from Royal Society of Chemistry. [131]

In recent years, lots of efforts have been devoted to develop lightweight, flexible and foldable supercapacitor for portable and even wearable electronics.[120] Zang *et al.* prepared graphene/PANI woven fabric composite films by electrochemically depositing PANI on the graphene woven fabric (GWF) film. The GWF had good dimensional stability and conductivity, and its unique structure supplied additional active surface for the electrolyte ions. Then a solid-state flexible symmetric supercapacitor with a whole thickness of smaller than 1 mm was assembled by using the graphene/PANI composite as electrodes. The supercapacitor showed a high specific area capacitance of 23 mF cm^{-2} at a constant current of 0.1 mA cm^{-2} , excellent cycle stability with about 100 % capacitance retention after 2000 cycles, and superior flexibility with improved specific area capacitance to 118 % after deformation. [133] Miao *et al.* prepared a free-standing carbon nanofibers/CNT/PANI ternary composite film with a specific capacitance of 315 F g^{-1} at 1 A g^{-1} s in a three-electrode testing cell. The corresponding solid-state

symmetric supercapacitor showed a specific capacitance of around 48 F g^{-1} at 2 A g^{-1} and remarkable cycle stability with 92 % capacitance retention after 10000 charge/discharge cycles. Additionally, current collector is not necessary for the assembling of supercapacitor, since the nanofiber/CNT films own excellent conductivity. [134]

Some researchers have studied the electrochemical properties of flexible supercapacitors in rolled and folded states. Zeng *et al.* prepared CNT/PANI composites via electrochemical re-expansion of CNT film into CNT hydrogel followed by electrodeposition of PANI on the obtained CNT hydrogel. The symmetric supercapacitor using CNT/PANI composites as electrodes exhibited a high specific area capacitance of 184.6 mF cm^{-1} at 1 mA cm^{-2} , and maintained the high capacitance in the rolled state. [135] Yu *et al.* synthesized sandwich structural rGO/PANI/carbon fiber composites by coating the composite of PANI nanowire arrays-wrapped N-doped carbon fiber cloth (PANI/CFC) by rGO. The rGO coating accommodated volume change and mechanical deformation of PANI during charge/discharge, and bridged the electronic connection of every PANI/CFC units. The charge transfer resistance in the composites was low due to the interactions between the components, namely π -conjugation, hydrogen bonding and hydrogen bonding. The symmetric two-electrode rGO/PANI/CFC supercapacitor using $1 \text{ M H}_2\text{SO}_4$ as electrolyte and encapsulated by PET film showed a high specific capacitance of 1145 F g^{-1} at 1 A g^{-1} and retained 94 % capacitance after 5000 cycles. Bending of this supercapacitor had only a slight influence on its specific capacitance as illustrated in Fig. 3.19. [136] Ge *et al.* designed an interesting foldable supercapacitor using triple networks of macroporous cellulose fibers, SWCNT and PANI nanoribbons as electrodes. The electrodes were prepared by dip-adsorption of SWCNT on Kimwipes tissue followed by in-situ polymerization of aniline. The obtained hybrid exhibited a good specific volume capacitance of 40.5 F cm^{-3} and a specific area capacitance of 0.33 F cm^{-2} at a current density of 0.2 mA cm^{-2} , and could be folded back and forth up to 1000 times without loss of capacitance or mechanical failure. [137]

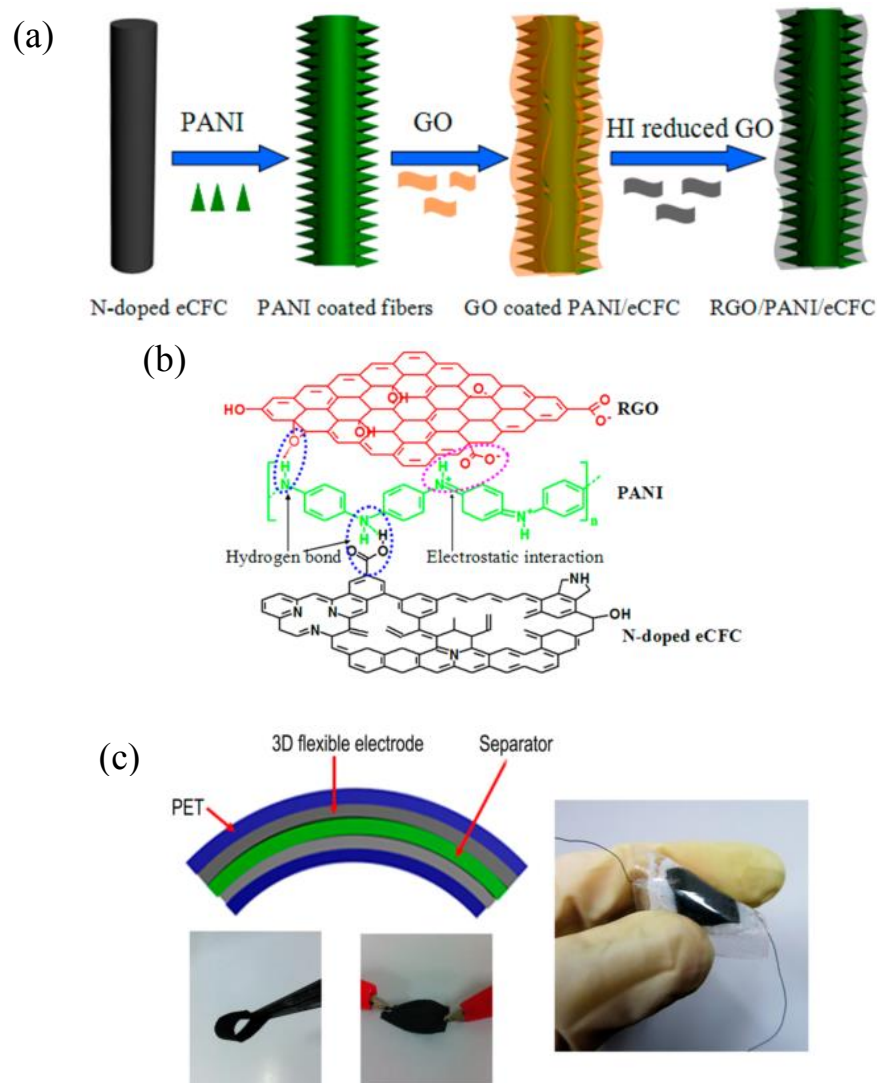


Fig. 3.19 (a) Procedure of producing rGO/PANI/CFC composites; (b) interactions among CFC, PANI, and rGO; (c) schematic of the flexible supercapacitor. Reuse with the permission from American Chemical Society. [136]

Recently, wire-shaped supercapacitors and micro-supercapacitors using carbon-based PANI composites as electrodes have been reported. Liu *et al.* prepared a flexible wire-shaped asymmetric supercapacitor, in which $\text{MnO}_2/\text{PPy}/\text{carbon}$ fiber composite and $\text{V}_2\text{O}_5/\text{PANI}/\text{carbon}$ fiber composite were used as the positive and negative electrodes, respectively (Fig. 3.20). The large difference between the work functions of MnO_2 and V_2O_5 increased the potential window to 2.0 V. The wire-shaped supercapacitor exhibited high specific capacitance (0.613 F cm^{-2} at a current density of 1.5 mA cm^{-2}) and excellent stability, and maintained the high capacitance under bending condition. [138] Xue *et al.* reported a novel method for the preparation of all-solid-state

flexible micro-supercapacitors (Fig. 3.21). GO patterns were fabricated by micromolding in capillary (MIMIC) and then reduced into rGO patterns; subsequently, PANI nanorods were in-situ electrodeposited on the rGO patterns. The symmetric two-electrode micro-supercapacitor using the as-prepared PANI/rGO hybrid as electrodes showed a high specific capacitance of 970 F g^{-1} at 2.5 A g^{-1} and good cycle stability with 90 % capacitance retention after 1700 cycles. [139]

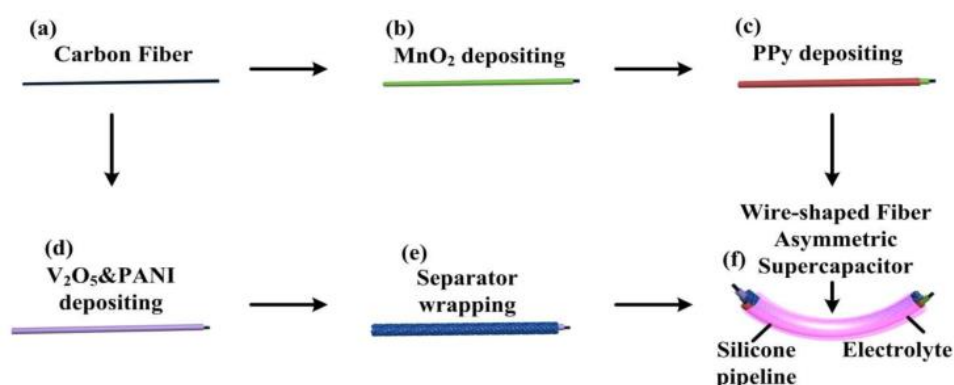


Fig. 3.20 Fabrication process of wire-shaped asymmetric supercapacitor using MnO₂/PPy/carbon fiber composite and V₂O₅/PANI/carbon fiber composite as composites. Reuse with the permission from Royal Society of Chemistry. [138]

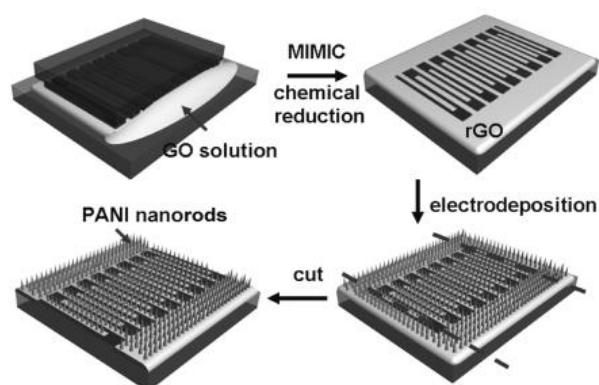


Fig. 3.21 Fabrication process of PANI/rGO microelectrodes. Reuse with the permission from John Wiley and Sons. [139]

In summary, carbon-based PANI composites are promising materials for supercapacitor electrode. Up to now, plenty of methods have been proposed to optimize the morphological structures and the surface properties (functional groups and

accessible surface area) of the carbonaceous component and PANI in order to enhance the conductivity, electrochemical and mechanical stability, and capacitive performance of the composites. Supercapacitor electrodes with new shapes and structures have been developed to meet the requirements of practical application. However, these developments of electrode materials with excellent electrochemical performance or new shapes usually suffer from high cost. In practical manufacturing, cost and environmental friendliness should be considered. Therefore, this report used the cost-effective rGO and GNP as the carbonaceous components and investigated two green ways of modification, in order to gain composites with not only good electrochemical properties but also low cost.

4. Experimental part

4.1. Materials

Aniline (99.8 wt.%) used for the preparation PANI/GNP composites (chapter 5.1) was purchased from Acros Organics; aniline used for the preparation of PANI/rGO composites (chapter 5.2 and 5.3) was purchased from Sigma Aldrich. Before use, aniline has been distilled under vacuum. Expanded graphite (EG) was supplied by SGL Carbon GmbH and has been dried in vacuum oven at 80 °C overnight before the experiment. Hydrochloric acid solution (HCl, 37 wt.% in water) was purchased from Merck. Sulfuric acid (H₂SO₄, 95-98 %), 4-dodecylbenzenesulfonic acid solution (DBSA, 70 wt.% in isopropanol), iron chloride (FeCl₃, 97 %), ammonium persulfate (APS, 98 wt.%), dopamine hydrochloride, tris (hydroxymethyl) aminomethane, tannic acid (TA), hydrogen peroxide (H₂O₂), phosphoric acid solution (H₃PO₄, 85 wt.% in water), hydrazine monohydrate (HH, 98 wt.%), polytetrafluoroethylene dispersion (PTFE, 60 wt.% in water), and polyvinyl alcohol (PVA, Mowiol 18-88) were purchased from Sigma Aldrich. Potassium permanganate (KMnO₄) was obtained from Acros Organics. All chemicals are of reagent grade. Carbon black super-P and stainless-steel mesh (SS mesh, type 304, 500 mesh) were purchased from Alfa Aesar. The SS mesh has been thoroughly washed by ethanol and then air-dried before use. Distilled water was used for the experiments related to chapter 5.1, and Millipore water was used throughout the experiment corresponding to chapters 5.2 and 5.3.

4.2. Sample Preparation

4.2.1. Synthesis of PANI/GNP composites

PANI/GNP composites were prepared by in-situ oxidative polymerization of aniline in the presence of GNP. Firstly, aniline, EG, and DBSA were added successively into a three-necked bottle with 150 mL, 1 M HCl solution and then stirred. The probe of an ultrasonic processor Hielscher (model UP400S, US finger S7) was placed into this bottle to sonicate under an amplitude of 55 for 2 h, aiming to exfoliate the EG into graphite nanoplates (GNP). Under vigorously stirring, the oxidant (FeCl₃ or APS) dissolved in 50 mL of 1 M HCl solution was subsequently added dropwise. The

polymerization process was performed in an ice bath (0-4 °C) for 4 h and then at room temperature for 20 h. The obtained green precipitate was collected by a glass frit G4, and then washed by distilled water, ethanol, acetone, and diethyl ether in sequence. Finally, the product was dried overnight at 100 °C under vacuum. The obtained PANI/GNP using FeCl₃ as oxidant were named as PANI/GNP-(mass ratio GNP:aniline)-(molar ratio FeCl₃:aniline)-(mass ratio DBSA:aniline). The composites prepared by using APS as oxidant were named as PANI/GNP-(mass ratio GNP:aniline)-(molar ratio APS:aniline)-(mass ratio DBSA:aniline)-APS. For example, the composite named as PANI/GNP-0.1-2-0-APS was prepared with a GNP to aniline weight ratio of 1 to 10 (0.1), an oxidant to aniline molar ratio of 2 to 1 (2), without the addition of dopant DBSA (0), and using APS instead of FeCl₃ as the oxidant (APS).

4.2.2. Synthesis of PANI/(GO-PDA) and PANI/GO-PDA composites

Synthesis of graphite oxide (GO): EG was chemically oxidized into GO according to the improved oxidation method developed by Marcano [140]. A concentrated H₂SO₄/H₃PO₄ (120 mL: 15 mL) solution was added to a mixture of 1 g EG and 6 g KMnO₄. Under vigorous stirring at 50 °C for 21 h, the mixture became paste with brownish grey color. After cooling down to room temperature, the paste was poured into a beaker containing approximately 200 mL ice, then 15 mL H₂O₂ was added. The final golden product was washed in succession with plenty of dilute hydrochloric acid solution (10 % in volume) and Millipore water with the aid of high speed centrifugation (Sigma 3-30KS, 10000 rpm, 20 min) until a pH value about 6 was reached. Then the GO solution was dialyzed in distilled water for one week.

Synthesis of polydopamine modified graphite oxide (GO-PDA): GO was reduced into GO-PDA0.5, GO-PDA0.8 and GO-PDA1.1 with a GO to PDA weight ratio of 1:0.5, 1:0.8 and 1:1.1, respectively. For the synthesis of GO-PDA0.5, 10.57 mL of 9.46 mg mL⁻¹ GO solution was firstly mixed with 200 mL of 20 mM Tris-HCl buffer solution (mixture of tris (hydroxymethyl) aminomethane and HCl, pH=8.5) and sonicated in water bath for 30 min. Subsequently, 50 mg dopamine hydrochloride was added into the GO dispersion. After reaction under magnetic stirring at 60 °C for 24 h, the product was precipitated from acetone by centrifugation at 10000 rpm for three

times. The precipitate was dialyzed in distilled water for 3 days, filtered, and vacuum dried at room temperature overnight.

Preparation of PANI, PANI/GO and PANI/(GO-PDA) composites: Pure PANI and PANI/GO and PANI/(GO-PDA) (1:0.1 wt./wt.) composites were synthesized by in-situ chemical oxidative polymerization of aniline. Firstly, 1 g (10.7 mmol) aniline and certain amounts of GO or GO-PDA were mixed in 150 mL of 1 M HCl solution, and sonicated in water bath at ambient temperature for 30 min. Then 50 mL of 1 M HCl solution containing 2.45 g (10.7 mmol) APS was dropwise added into the mixed solution. After reaction in ice bath for 4 h and then at ambient temperature for 20 h under vigorous stirring, the resulting green precipitate (PANI/GO or PANI/(GO-PDA) composites) were filtered, washed with plenty of Millipore water and ethanol, and then dried in a vacuum oven at 100 °C overnight. Pure PANI was produced by the same method, without the addition of GO or GO-PDA.

Synthesis of PANI/GO-PDA composites: The PANI/GO (1:0.1) composite was further processed into PANI/GO-PDA composites containing different amount of PDA. For example, PANI/GO-PDA (1/0.1-0.5) composite was synthesized by immersing 1 g PANI/GO (1:0.1) composite into 200 mL of 20 mM Tris-HCl buffer solution (pH=8.5) and sonicating in water bath for 30 min. Then 50 mg dopamine hydrochloride was added into the mixture and reacted under magnetic stirring at 60 °C for 24 h. The final product was filtered, washed by Millipore water, dialyzed in distilled water for 3 days, filtered again and dried in a vacuum oven at 60 °C overnight. The difference between the synthesis processes of PANI/(GO-PDA) and PANI/GO-PDA is shown in Fig. 4.2.1.

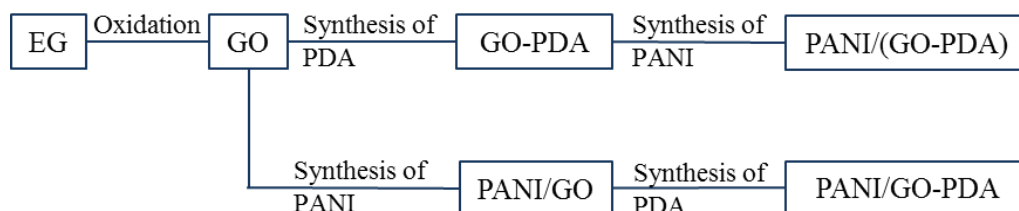


Fig. 4.2.1 Schematic diagram of the synthesis process of PANI/(GO-PDA) and PANI/GO-PDA.

4.2.3. Synthesis of PANI/(rGO-TA), PANI/(rGO-HH), and PANI/GNP composites

Reduction of GO by tannic acid or hydrazine hydrate: 220 mg tannic acid (TA) was added into 3 mL of 7.38 mg mL^{-1} as-prepared GO solution. Then the mixture was heated to 95°C under magnetic stirring for 2 h, 12 h or 24 h. After reduction, the products were collected by vacuum filtration and washed 10 times by plenty of Millipore water. The final rGO solutions were labelled as rGO-TA-2h, rGO-TA-12h, and rGO-TA-24h. Subsequently, half amount of the obtained rGO-TA-24h was further washed by ethanol for 10 times to remove TA; the product is named as rGO-TA-24h-EOH. For comparison, rGO reduced with hydrazine hydrate (HH) was synthesized and labelled as rGO-HH. The GO and HH solutions with a GO: HH weight ratio of 10:7 were mixed and then reacted at 95°C under stirring for 24 h. The final product were collected by vacuum filtration and washed successively by plenty of Millipore water and ethanol.

Preparation of graphite nanoplates (GNP): 1 g EG was immersed in an ethanol solution (70 % ethanol in volume) for 14 h and then sonicated with or without TA (0.5 g) in a Bandelin Sonorex ultrasonic bath (RK 102H, 140 W) for 10 h. The obtained GNPs with and without TA were labelled as GNP-TA and GNP, respectively. Fig. 4.2.2 illustrates the process of synthesizing rGOs and GNPs based on EG.

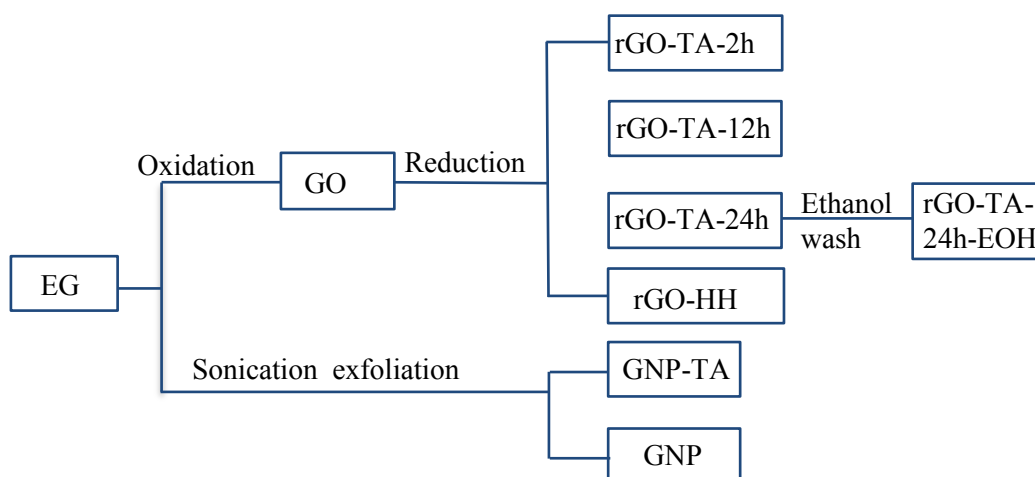


Fig. 4.2.2 Diagram of producing rGOs and GNPs from EG.

Synthesis of PANI/(rGO-TA), PANI/(rGO-HH) and PANI/GNP composites: 50 mL of 1 M HCl solution with 2.45 g APS was dropwise added into 150 mL of 1 M HCl solution containing 1 g aniline and certain amounts of rGO or GNP. The polymerization process was performed in ice bath for 4 h and then at room temperature for 20 h under vigorous stirring. The resulting green precipitate was filtered, successively washed with plenty of Millipore water and ethanol, and then dried in a vacuum oven at 100 °C overnight.

4.3. Instruments and Characterization methods

Ultraviolet-visible (UV-vis) spectra of PANI, PANI/GNP composites, GO, and GO-PDA were studied by a SPECORD 210 Plus spectrophotometer (Analytic Jena, Germany) at ambient temperature. The ethanol solution with tiny amount of the PANI or PANI/GNP samples, or the diluted GO solution was placed in 1.5 mL semi-micro cuvettes of PMMA for the UV-vis test. Fourier-transform infrared attenuated total reflectance (FTIR/ATR) spectra of powder-like solid-state samples were recorded by a Tensor 27 spectrometer (Bruker, USA) in a wavenumber range from 4000 cm^{-1} to 550 cm^{-1} . X-ray photoelectron spectroscopy (XPS) analysis was performed on an AXIS ULTRA instrument with a monochromatic Al $K_{\alpha 1,2}$ X-ray source (Kratos Analytical, England). The powder-like solid-state sample was fixed on an electrically non-conductive double-sided adhesive tape. X-ray diffraction (XRD) spectra were recorded using a two-circle diffractometer XRD 3003 TT (GE Sensing&Inspection Technology GmbH, Germany) with a Cu-K α radiation ($\lambda = 0.1542 \text{ nm}$). The fine powder-like GO and rGO samples were tested in quartz glass capillary tubes, and the platelet-like EG sample was tested in aluminum (Al) foil. Raman spectra were measured using a confocal Raman microscope alpha 300R (WITec GmbH, Germany) with a laser line at 532 nm. The measurements were performed using a $\times 20$ microscope and with a laser power of 10 mW. Thermogravimetric analysis (TGA) was tested by the TGA Q5000 (TA Instruments, USA). The powder-like samples with weights of about 5 mg were added into the testing glass tubes, and then heated from ambient temperature to 800 °C with a linear heating rate of 10 K min^{-1} under nitrogen atmosphere.

The Brunauer-Emmett-Teller (BET) specific surface areas were measured by an Autosorb-1 from Quantachrome (USA) using nitrogen as adsorbent at 77 K. Scanning electron microscopy (SEM) images were obtained using a Zeiss Ultra Plus field emission scanning electron microscope (FE-SEM, Carl Zeiss Microscopy GmbH, Germany). Few milligrams of the sample were dispersed in acetone and then a drop of the dispersion was placed on a cleaned wafer and dried in hot air oven at 50 °C for 2 hours. The sample was sputter coated with platinum before test. The energy dispersive X-ray spectrometry (EDX) was tested on an EDS Spectrometer XFlash 5060FQ (Bruker, USA), in order to analyse the distribution of PANI in PANI/GNP composites. An in-house built device together with the Testpoint™ software was employed to measure conductivity. [141] Powder-like samples were tested in a poly(methyl methacrylate) (PMMA) cylinder with a cavity diameter of 5 mm. As shown in Fig. 4.3.1, the gold-plated plunger compressed the samples into defined pressures (30 MPa), aiming to assure good contact between the particles. And the DMM 2001 multimeter (Keithley Instruments) recorded the distance and the resistivity between the plunger and the gold-plated base. Then the conductivity of sample was calculated according to the resistance values and the geometry of the system. The weight of each sample was around 50 mg.

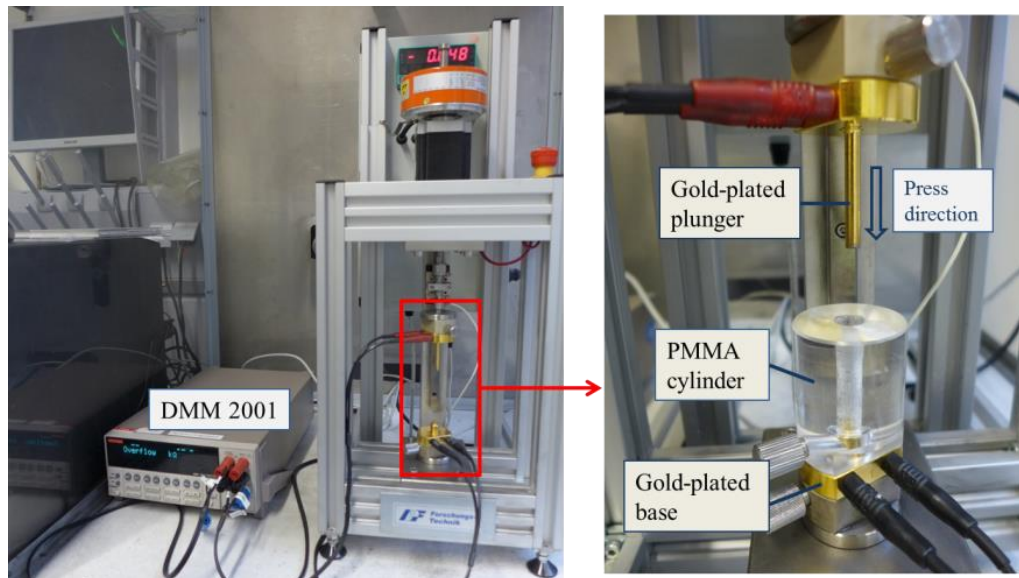


Fig. 4.3.1 Photographs of the in-house built device for powder conductivity testing.

The electrochemical properties were measured on an Ivium-n-Stat potentiostat/galvanostat (Ivium Technologies, the Netherlands). The cyclic voltammetric tests of materials performed in a conventional three-electrode system with were a potential range of -0.9 V to 0.55 V (chapter 5.1) or a range of -1.0V to 0.6V (chapter 5.2 and 5.3). As illustrated in Fig. 4.3.2 (a) and (c), the testing system was made up by working electrode (WE), reference electrode (RE), counter electrode (CE, Pt coil) and electrolyte (1 M Hg₂SO₄). The Hg/Hg₂SO₄ reference electrode has a potential of 0.613 V versus the normal hydrogen electrode. For the preparation of WE, the active materials, carbon black super-P, and PTFE with a weight ratio of 8:1:1 were firstly dispersed in Millipore water. Then the dispersion was sonicated in a water bath for 30 min and dried in a vacuum oven at 80 °C overnight. Subsequently, the dried mixture was mixed with some ethanol and then kneaded into a paste by an agate mortar and pestle. The final paste-like product was pressed on a circular stainless steel mesh with a diameter of 10 mm (current collector) under a pressure of 100 kN for 3 min. The weight of active material in the electrode varied between 3 mg and 10 mg. Based on the cyclic voltammetric results, the specific capacitances (c , F g⁻¹) of the active materials under certain potential scan rates (ν , V s⁻¹) were calculated by the equation:

$$c = \frac{\int I(V) \cdot dV}{2m \cdot \Delta V \cdot \nu} \quad (4.3.1)$$

where $I(V)$ (A) represents the magnitude of current at a potential of V (V), ΔV represents the potential window, and m (g) is the mass of active material in the WE. Some of the investigated composites, namely PANI/(rGO-TA-24h), PANI/(rGO-HH), PANI/(GNP-TA), and PANI/GNP have been further assembled into two-electrode solid-state symmetric supercapacitor devices (see Fig. 4.3.2 (b) and (d)). Electrode sheets were prepared by the same method as for the three-electrode electrochemical testing. H₂SO₄-PVA gel was used as both solid-state electrolyte and separator. Firstly, two electrode sheets with same weight and same shape were pressed on stainless steel mesh (current collector) under 200 kN for 3 min. H₂SO₄-PVA gel was prepared by mixing 3 g PVA with 30 mL of 1 M H₂SO₄ at 85 °C under stirring for 1 h. After it cooled down, the stainless steel meshes, which had been coated with the electrode material, were immersed into H₂SO₄-PVA gel for 5 min, and then the system was solidified at ambient temperature for 3 h. Finally, the two stainless steel meshes were

assembled into symmetric supercapacitors. Glass slides (top and bottom) and scotch tape were used to fix the supercapacitors. The cyclic voltammetric behavior of the as-prepared symmetric supercapacitor devices were tested in the voltage range of -0.9 V to 0.55 V. The galvanostatic charge/discharge performances of the devices were investigated between 0 V to 0.5 V.

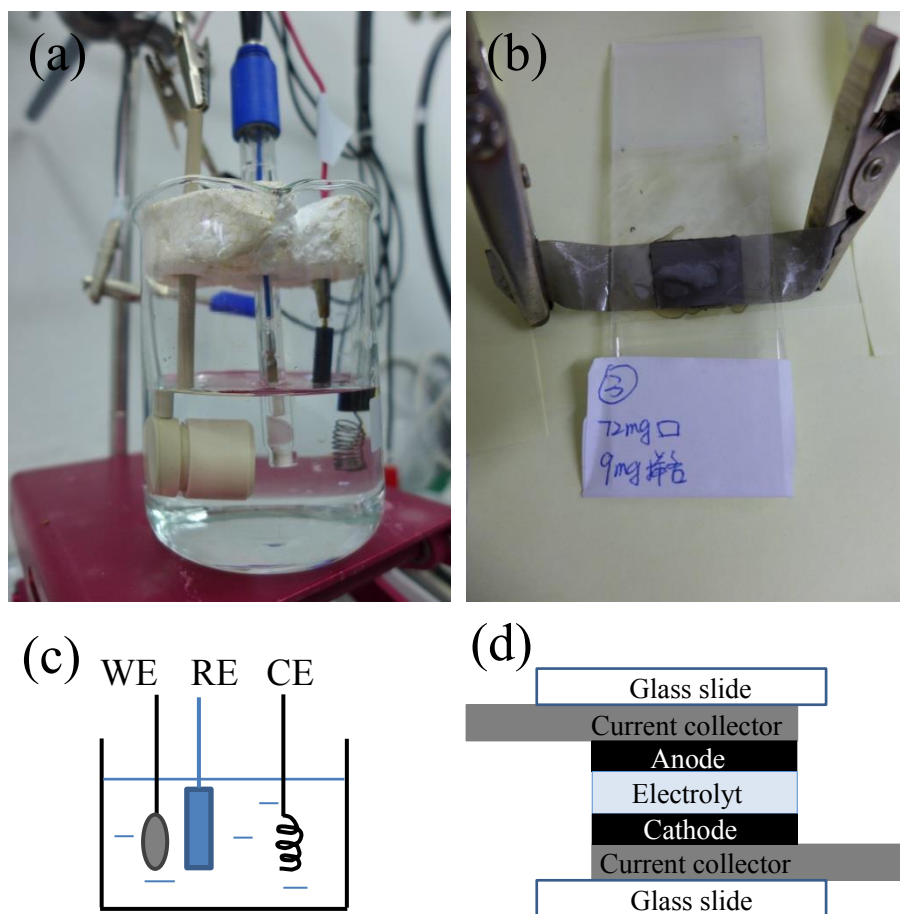


Fig. 4.3.2 (a) and (c) photograph and schematic of the three-electrode electrochemical testing setup; (b) and (d) photograph and schematic of two-electrode supercapacitor device.

5. Result and Discussions

5.1. PANI/GNP composites with different oxidant and dopant loading

Note: The results presented in chapter 5.1 are published in my paper “Effect of dopant and oxidant on the electrochemical properties of polyaniline/graphite nanoplate composites” (Polymer International, 2018. 67(10): p. 1429-1437) with the co-authors Olga Grätz and Jürgen Pionteck.

5.1.1. Introduction

Carbon-based PANI composites can be produced by numerous methods, such as electrodeposition or spraying of PANI onto carbonaceous materials, [127, 142] interfacial polymerization, [143] and the in-situ chemical-oxidative polymerization. [144, 145] Among them, the in-situ chemical polymerization of PANI on carbon fillers is easy, fruitful, and suitable for large-scale manufacturing. Many researchers have devoted their efforts to improve the properties of in-situ polymerized carbon-based PANI composites. For example, Li *et al.* fabricated orientated arrays of PANI nanorods on expanded graphite nanosheets. [146] Mao *et al.* used surfactants to increase the dispersibility of graphene. [119] Zhang *et al.* investigated the effect of mass ratio of components. [147] Some synthesis parameters, such as the dopant and oxidant, were reported to be critical to the electrochemical performance of pure PANI. [148, 149] However, the influence of these parameters on performance of the in-situ polymerized PANI/GNP composites has been scarcely reported. Therefore, in the first section of my study, the effect of dopant and oxidant on the electrochemical properties of carbon-based PANI composites was investigated. Graphite nanoplates (GNP), composed by multiple layers of graphene, were used as the carbon filler in this part. GNP has been extensively treated as an attractive alternative to the monolayer graphene. Compared to the monolayer graphene, which is difficult to produce in large scale, GNP is a cost-effective since it can be derived from natural graphite, and also has high mechanical strength, large specific surface area, and good electrical conductivity. [28, 150]

In this chapter, the conductivity, morphology and cyclic voltammetric behavior of the PANI/GNP (1:1) and (1:0.1) composites, prepared by using iron chloride (FeCl_3 , in

varying amounts) or ammonium persulfate (APS) as oxidant, with or without addition of 4-dodecylbenzenesulfonic acid (DBSA) as dopant, have been investigated. [151] The PANI/GNP composites prepared using FeCl_3 and APS as oxidant are named as PANI/GNP-(mass ratio GNP:aniline)-(molar ratio FeCl_3 :aniline)-(mass ratio DBSA:aniline) and PANI/GNP-(mass ratio GNP:aniline)-(molar ratio APS:aniline)-(mass ratio DBSA:aniline)-APS, respectively. For example, PANI/GNP-0.1-2-0-APS is a PANI/GNP (1:0.1) composite produced with an oxidant (APS) to aniline molar ratio of 2 to 1 and without the addition of DBSA.

5.1.2. Structural characterization of PANI/GNP composites

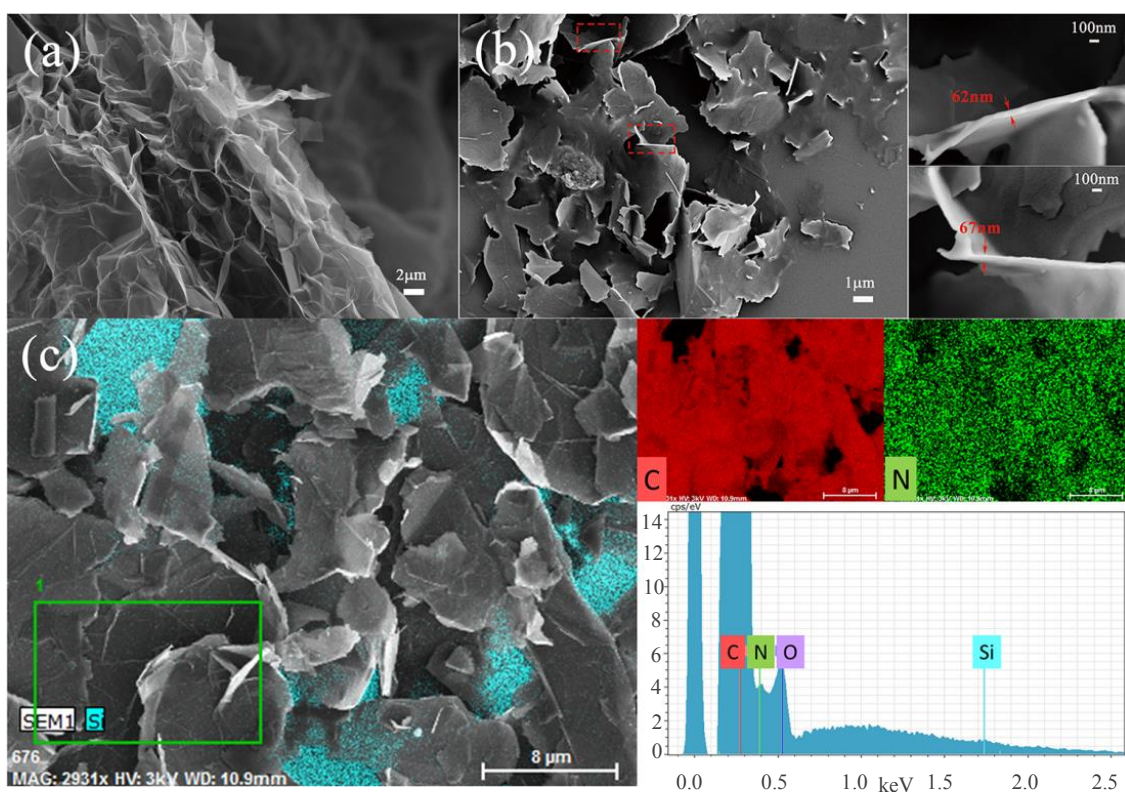


Fig. 5.1.1 (a) SEM image of EG, (b) SEM images of GNP, and (c) SEM image and EDX analysis of the PANI/GNP-1-2.3-0 composite. [151]

The morphologies of expanded graphite (EG) and GNP were illustrated in Fig. 5.1.1 (a) and (b), respectively. Obviously, in this study EG was successfully exfoliated into GNP by sonication. The thicknesses of the GNP layers shown in Fig. 5.1.1 (b) were measured to be between 10 nm and 100 nm. For example, the two GNP layers in the enlarged images own thicknesses of 62 nm and 67 nm. Fig. 5.1.1 (c) shows SEM image

of PANI/GNP-1-2.3-0 composite. The corresponding EDX analysis indicates that the carbon and nitrogen were homogeneously distributed in the composite, which means that the GNP was evenly coated with in-situ polymerized PANI.

The structures of pure PANI and PANI/GNP composites were characterized by the UV-vis, FTIR/ATR, and XPS measurements. Fig. 5.1.2 (a) shows the result of UV-vis test. The spectrum of pure PANI (PANI-0-2.3-0) owns a peak at 374 nm, corresponding to π - π^* transition absorbance. [152] The UV-vis spectra of PANI/GNP-1-2.3-0 and PANI/GNP-0.1-2.3-0 composites also show this characteristic peak, but the position moves to 389 nm and 382 nm, respectively. These red shifts indicate that π conjugation existed between the PANI chains and GNP. In Fig. 5.1.2 (b), the FTIR/ATR spectrum of pure PANI shows peaks at 1561 cm^{-1} and 1484 cm^{-1} , corresponding to the C=C stretching vibrations of quinoid ring and benzene ring, respectively. The FTIR/ATR spectra of both composites display similar bands as the spectrum of pure PANI, which demonstrates the existence of PANI in the composites. [153, 154] The both peaks of composites slightly shift to larger wavenumbers compared to the pure PANI. This phenomenon implies that the interaction between PANI and GNP is not only the π conjugation. In order to further understand the interaction between PANI and GNP, the N 1s XPS spectra of pure PANI and PANI/GNP (1:1) composites were studied (Fig. 5.1.3). The spectrum of PANI shows four characteristic peaks at 397.9 eV, 399.5 eV, 400.5 eV, and 401.5 eV, respect to the quinoid imine (=N-), benzenoid amine (-NH-), positively charged imine (=N+) and amine (-N+), respectively. [145] In the N 1s XPS spectrum of PANI/GNP-1-2.3-0 composite, the intensities of the peaks related to =N- and =N+ are increased, and the intensities of the peaks related to -NH- and -N+ become weaker. This phenomenon means the ratio of benzeoid structures to quinoid structures in the PANI was decreased. In another word, the presence of GNP changed the electron distribution in PANI.

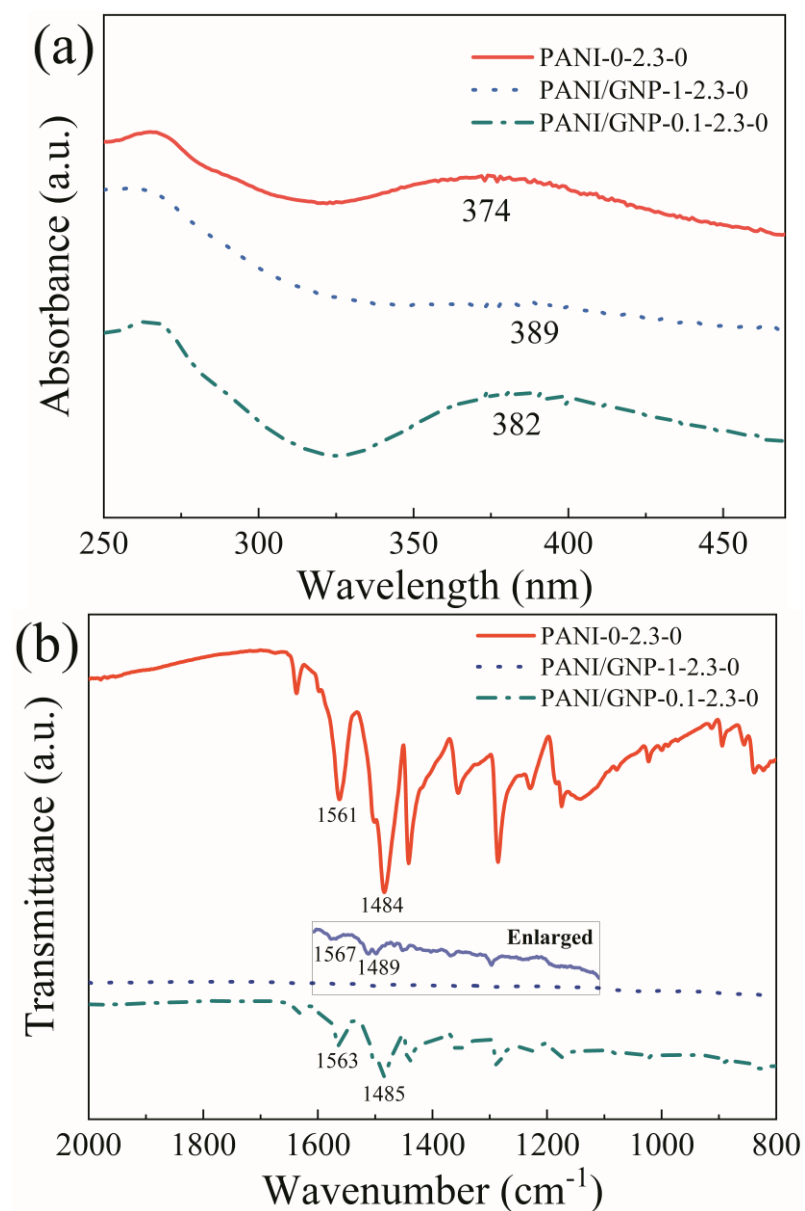


Fig. 5.1.2 (a) UV-vis and (b) FTIR/ATR spectra of pure PANI (PANI-0-2.3-0) and PANI/GNP-1-2.3-0 and PANI/GNP-0.1-2.3-0 composites. [151]

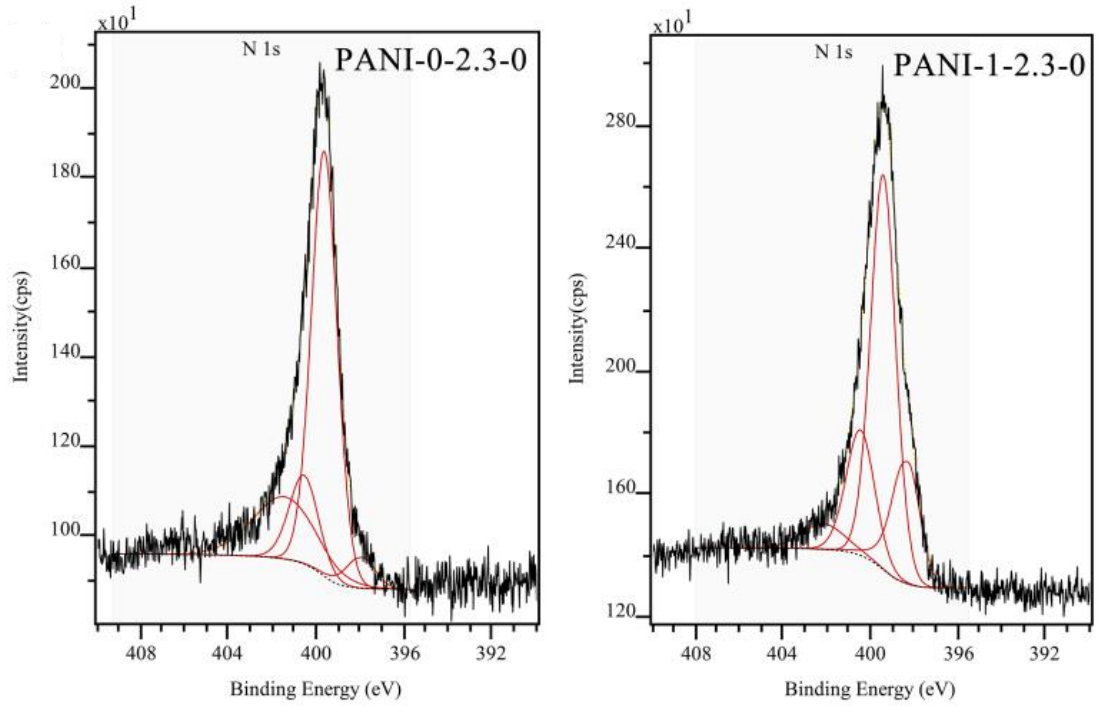


Fig. 5.1.3 N 1s XPS spectra of pure PANI (PANI-0-2.3-0) and PANI/GNP-1-2.3-0 composite. [151]

Thermogravimetric analysis was used to roughly evaluate the actual content of PANI (x_i) and GNP (y_i) in the obtained PANI/GNP (1:1) and (1:0.1) composites. Assuming that PANI and GNP components in the composites perform the same weight loss at 800 °C as the pure PANI and EG. In Equation 5.1.1 x_f and y_f present the percentage of PANI and GNP in the composite, and p_x , p_y , and p represent the residue weight of PANI, GNP and composites after TG test.

$$x_f + y_f = p(x_i + y_i) \rightarrow x_i = \left[\frac{(p_y - p)}{(p - p_x)} \right] \times y_i \quad (5.1.1)$$

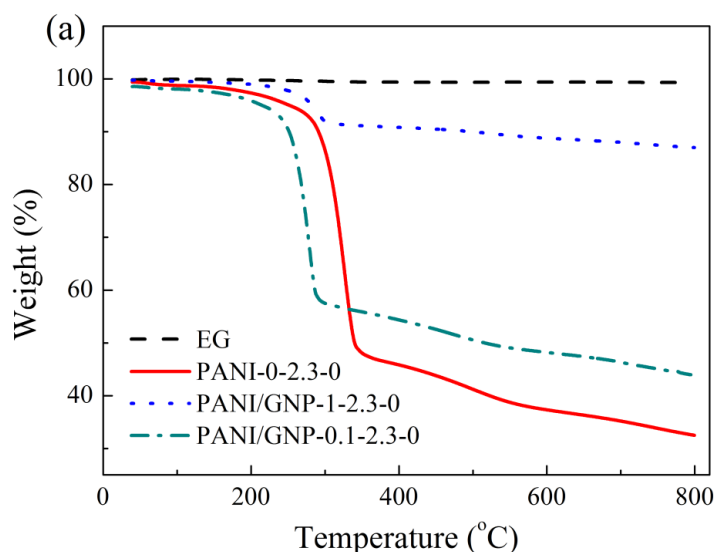
Since the sum of the percentage content of PANI and GNP in the composites is 100 (wt.%), therefore,

$$x_i + y_i = y_i \times \left[\frac{(p_y - p)}{(p - p_x)} + 1 \right] = 100 \rightarrow y_i = 100 / \left[\frac{(p_y - p)}{(p - p_x)} + 1 \right] \quad (5.1.2)$$

Exemplary, Fig. 5.1.4 (a) shows the thermogravimetric curves of EG, pure PANI (PANI-0-2.3-0), and PANI/GNP-1-2.3-0 and PANI/GNP-0.1-2.3-0 composites. EG owns a very stable thermogravimetric property. It lost only 0.7 % weight after being

heated to 800 °C. The thermogravimetric curves of pure PANI and PANI/GNP composites exhibit weight loss of up to 3 % below 150 °C, which is attributed to evaporation of moisture. Then the curves show significantly weight loss at around 280 °C to 320 °C, due to the decomposition. In this degradation step, the thermogravimetric curve of pure PANI illustrates about 50 wt.% weight loss, followed by other two mild weight loss before 800 °C. Based on the Equation 5.1.1 and Equation 5.1.2, the contents of PANI in the PANI/GNP-0.1-2.3-0 and PANI/GNP-1-2.3-0 composites were estimated to be 82.8 wt.% and 18.4 wt.%, respectively.

The calculated contents of PANI in all the PANI/GNP (1:1) and (1:0.1) composites are shown in Fig. 5.1.4 (b). Theoretically, the PANI content in a PANI/GNP (1:1) composite should be 50 wt.%, and that in a PANI/GNP (1:0.1) composites should be 91 wt.%. However, the calculated PANI contents for the PANI/GNP composites using FeCl_3 as oxidant are much lower than these values (50 wt.% and 91 wt.%). When FeCl_3 was added in a sub-stoichiometric amount (FeCl_3 : aniline=1:1), the yield of PANI is further reduced, since one aniline-aniline coupling needs 2 Fe (III) ions. Contrarily, the calculated contents of PANI in the PANI/GNP-APS (1:1) and (1:0.1) composites are almost equal to 50 wt.% and 91 wt.%, respectively. This phenomenon indicates using APS as oxidant is beneficial to a complete conversion of aniline to PANI compared to using FeCl_3 . Additionally, adding DBSA has no influence on the yield of PANI in the PANI/GNP composites.



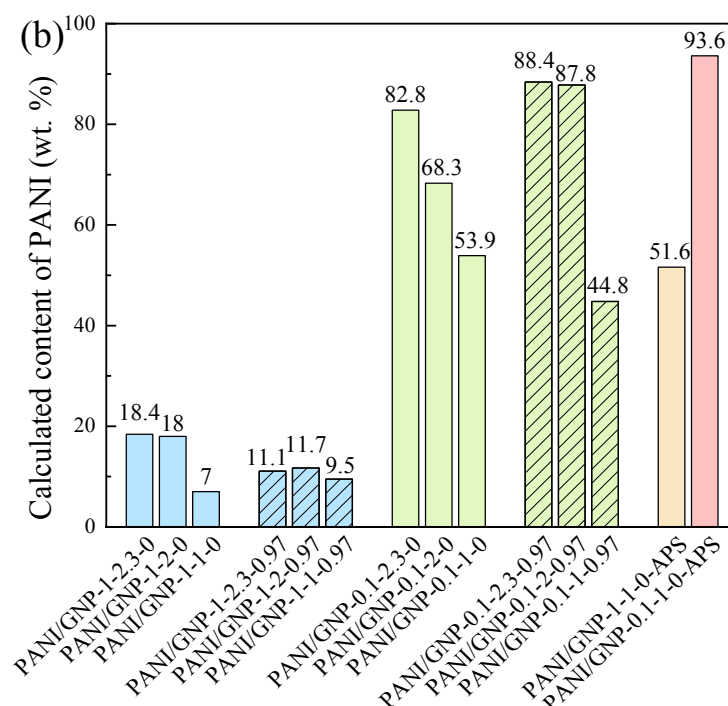


Fig. 5.1.4 (a) Thermogravimetric analysis of EG, pure PANI (PANI-0.2.3-0), and PANI/GNP-1.2.3-0 and PANI/GNP-0.1.2.3-0 composites; (b) histogram of the calculated content of PANI in the PANI/GNP composites. [151]

5.1.3. Effect of dopant and oxidant amount on electrochemical behavior

Cyclic voltammetric (CV) behavior of the PANI/GNP composites were investigated to evaluate their capacitive performance and to characterize their electrochemical properties. The CV plots of PANI/GNP (1:1) composites using different content of FeCl_3 as oxidant with and without dopant (DBSA) are shown in Fig. 5.1.5. All the CV plots illustrate reversible redox behavior. There are two pairs of typical redox peaks in the CV plots, i.e. A_1/C_1 and A_2/C_2 in Fig. 5.1.5. As the potential increasing, the state of PANI transfers from leucoemeraldine to emeraldine, and then to pernigraniline. [155] With the increase of potential scan rate, the magnitude of current increases steadily, indicating the good rate capability of PANI/GNP (1:1) composites. [156] Moreover, the anodic peaks (A_1 and A_2) and the cathodic peaks (C_1 and C_2) in the CV plots shift positively and negatively, respectively, with the potential scan rate increasing. The shifts of redox peaks are due to the internal resistance of the electrode.

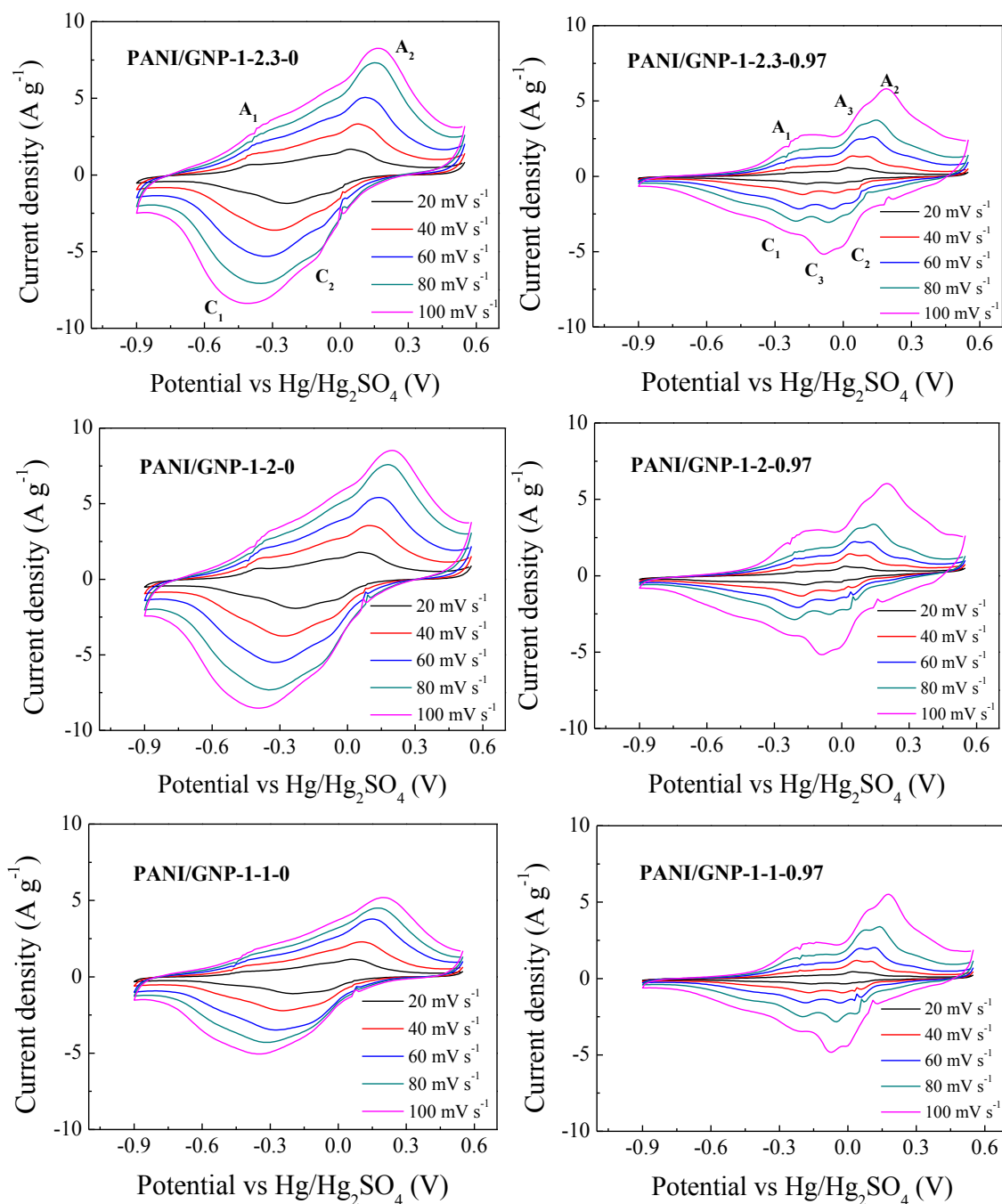


Fig. 5.1.5 Cyclic voltammograms of PANI/GNP (1:1) composites using FeCl_3 as oxidant at different scan rates. [151]

Comparing the CV plots of PANI/GNP (1:1) composites with DBSA (Fig. 5.1.5, right) and those without DBSA (Fig. 5.1.5, left), it is obvious that the CV plots of PANI/GNP (1:1) composites with DBSA own an additional pair of redox peaks (A_3/C_3). As reported by Pruneanu *et al.*, this middle pair of redox peaks is due to the degradation of PANI or the presence of ortho-coupled polymers. [157] Moreover, the addition of

DBSA reduces the integral area of the CV loops, which means the capacitive ability of PANI/GNP (1:1) composites decreased. According to the conductivities of PANI/GNP (1:1) composites with and without DBSA shown in Table 5.1.1, adding DBSA increased the conductivity of composites. In a word, the interaction between the alkyl chains of dopant (DBSA) and the PANI backbone had positive effect on the conductivity, [158, 159] but meanwhile impeded the capacitance of PANI/GNP (1:1) composites. Similar phenomenon has been reported by other researchers. Bian *et al.* found that the de-doping process can improve the electrochemical capacitance and rate capability of PANI nanofibers. [160] Misoon *et al.* has reported that the activated carbon/DBSA-doped PANI composite prepared with 0.06 M DBSA own lower capacitance than the composite prepared with 0.045 M DBSA. [161]

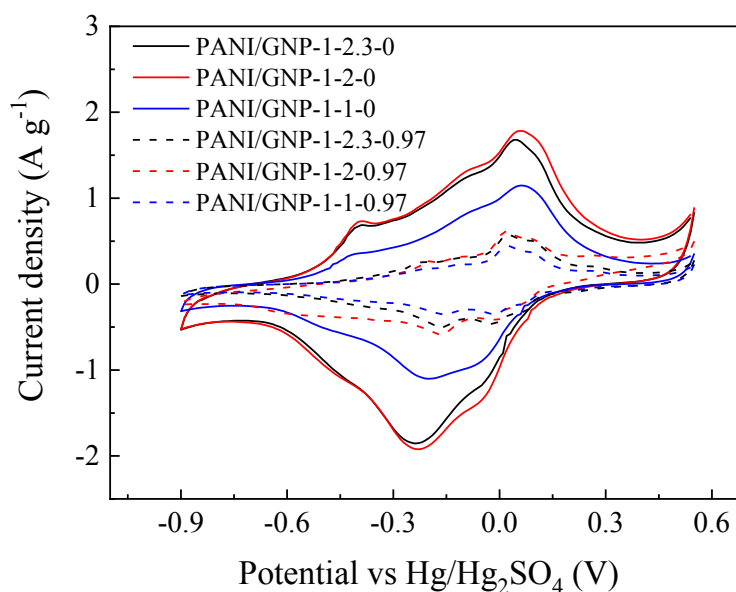


Fig. 5.1.6 Cyclic voltammograms of PANI/GNP (1:1) composites at a scan rate of 20 mV s⁻¹. [151]

Fig. 5.1.6 compares the CV plots of PANI/GNP (1:1) composites at a scan rate of 20 mV s⁻¹. With the molar ratio of FeCl₃ to aniline increase from 1 to 2 and then to 2.3, the magnitude of current density and the integral area of CV loops for both of the PANI/GNP (1:1)-DBSA composites and the PANI/GNP (1:1) composites without DBSA increase firstly, and then decrease slightly. The slight decrease of the capacitive

behavior of PANI/GNP composites with the increase of FeCl_3 to aniline molar ratio from 2 to 2.3 might be due to the over-oxidation of PANI. [149]

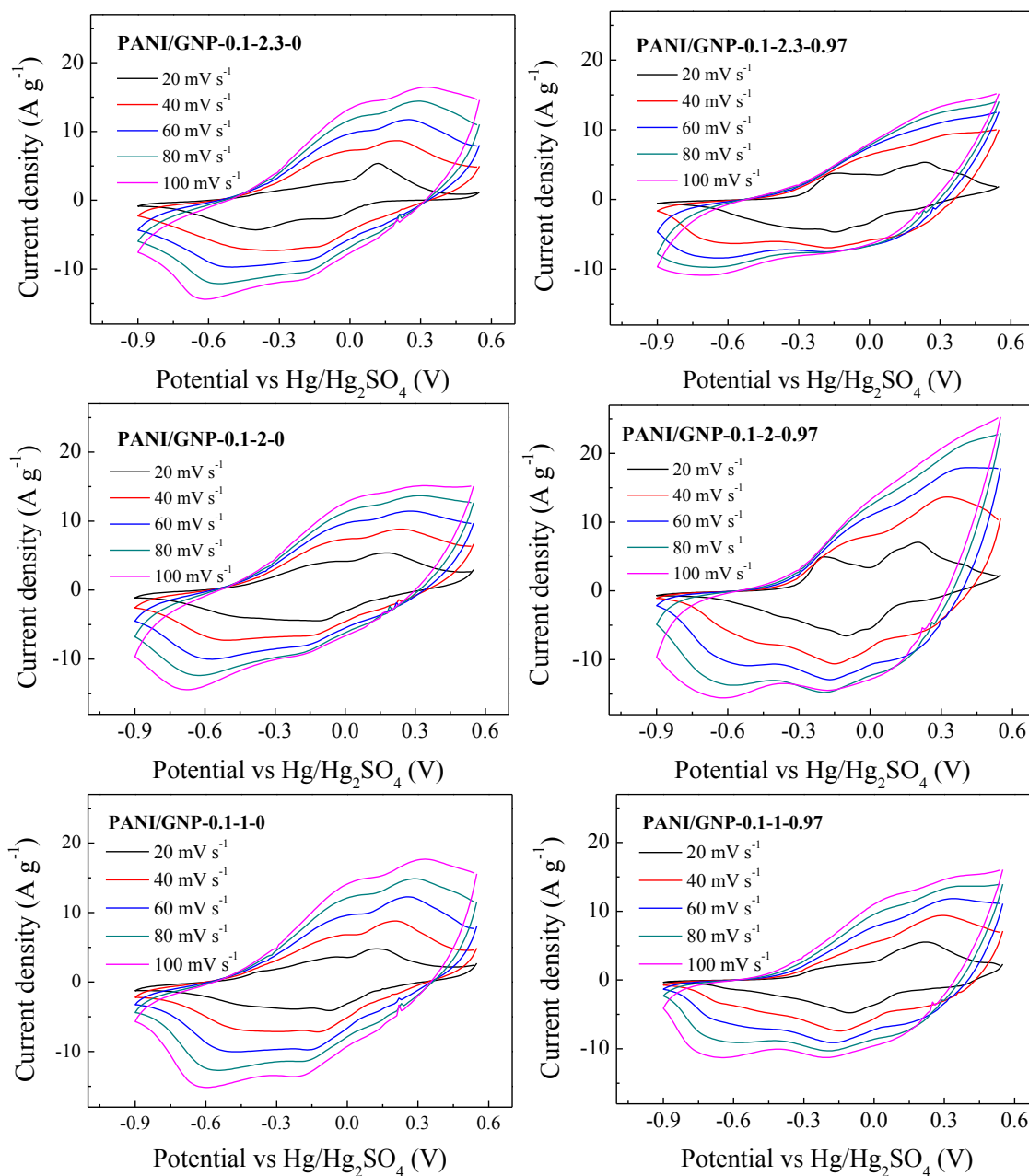


Fig. 5.1.7 Cyclic voltammograms of PANI/GNP (1:0.1) composites using FeCl_3 as oxidant. [151]

The cyclic voltammetric behavior of PANI/GNP (1:0.1) composites were also investigated (Fig. 5.1.7). Similar to the CV plots of PANI/GNP (1:1) composites shown

in Fig. 5.1.5, the CV plots of all the PANI/GNP (1:0.1) composites also show reversible redox response. With the potential scan rate increasing, the oxidation peaks and reduction peaks also shift positively and negatively, respectively. But the increasing rates of the magnitude of CV plots with the potential scan rate are no longer as steady as in the case of PANI/GNP (1:1) composites, especially for the PANI/GNP (1:0.1)-DBSA composites. This phenomenon indicates the rate capability of PANI/GNP (1:0.1) composites is worse than that of the PANI/GNP (1:1) composites.

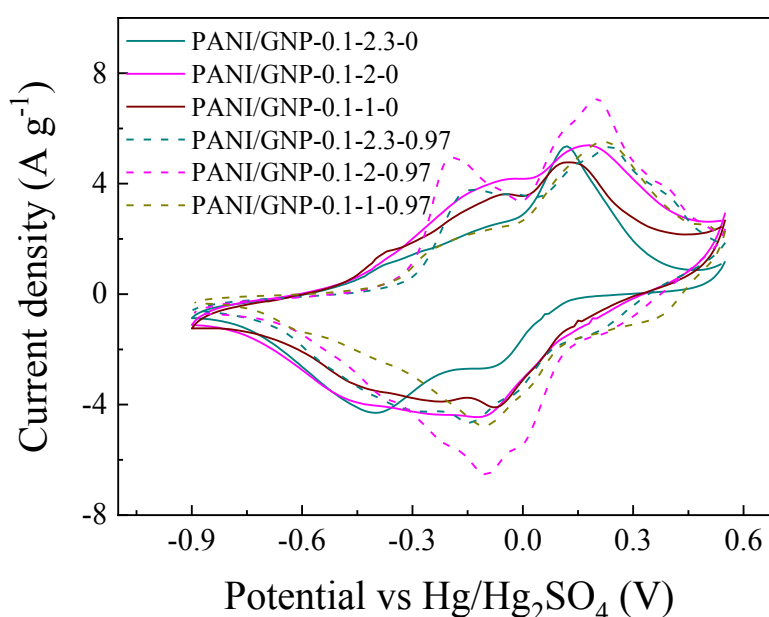


Fig. 5.1.8 Cyclic voltammograms of PANI/GNP (1:0.1) composites at a scan rate of 20 mV s⁻¹. [151]

Fig. 5.1.8 compares the CV plots of all the obtained PANI/GNP (1:0.1) composites at a potential scan rate of 20 mV s⁻¹. Inconsistent with the negative effect of DBSA on the capacitive ability of PANI/GNP (1:1) composites (Fig. 5.1.6), adding DBSA slightly increases the integral area of the CV loop of PANI/GNP-0.1-2 and PANI/GNP-0.1-2.3 composites. The opposite effect of DBSA on the cyclic voltammetric behavior of PANI/GNP (1:0.1) and PANI/GNP (1:1) composites might be attributed to different conductivities of the composites. As illustrated in Table 5.1.1, for the PANI/GNP composites without DBSA, the composites with a PANI to GNP weight ratio of 1:0.1 show lower conductivities than the corresponding composites with a PANI to GNP

weight ratio of 1:1. This result is due to the higher conductivity of GNP compared to PANI. When the DBSA is added into the composites, the conductivities of PANI/GNP (1:0.1) composite increase three to four orders of magnitude; while the conductivities of PANI/GNP (1:1) composites only increase less than or around one order of magnitude. It is well-known that the electrochemical properties are tightly connected to the conductivity. Therefore, the positive effect of DBSA on the overall capacitive behavior of PANI/GNP (1:0.1) composites might be attributed to the dramatically increase of conductivity, which offset the negative effect of DBSA on the capacitance of PANI component. Additionally, both of PANI/GNP (1:0.1)-DBSA composites and PANI/GNP (1:0.1) composites without DBSA illustrate the largest integral area of CV loop at a FeCl_3 to aniline molar ratio of 2, which is similar to the PANI/GNP (1:1)-DBSA composites and PANI/GNP (1:1) composites.

The specific capacitance of PANI/GNP (1:1) and (1:0.1) composites were calculated according to their cyclic voltammograms by the Equation 4.3.1 and shown in Table 5.1.1. Fig. 5.1.9 illustrates the plot of specific capacitance of PANI/GNP (1:1) and (1:0.1) composites to the scan rate. Obviously, the specific capacitances of PANI/GNP (1:0.1) composites are higher than those of PANI/GNP (1:1) composites. Conway *et al.* has reported that the capacitance of a pseudocapacitor could be 10 to 100 times higher than the electrostatic capacitance of an EDLC. [55] The much better capacitive ability of PANI/GNP (1:0.1) composites compared to PANI/GNP (1:1) composites indicates that the PANI, which showed pseudocapacitance, contributed more than the GNP, which exhibited EDLC, to the overall capacitance of composites. However, the rate capabilities of PANI/GNP (1:0.1) composites were worse than those of PANI/GNP (1:1) composites. As shown in Fig. 5.1.9, the specific capacitances of PANI/GNP (1:0.1) composites decrease with the increase of the potential scan rate. Contrarily, the specific capacitances of PANI/GNP (1:1) composites keep stable or even increase slightly with scan rate increasing. The extraordinary slight increase in the specific capacitance of some PANI/GNP (1:1) composites with the scan rate might be caused by experimental error. The better rate capabilities of PANI/GNP (1:1) composites compared to the PANI/GNP (1:0.1) composites are due to the higher amount of GNP. It has been reported that the carbonaceous materials can not only offer a pathway for electron transfer, but also supply a structural support for the PANI. [146] Furthermore, adding

dopant (DBSA) decreased the specific capacitances of PANI/GNP (1:1) composites but increased those of certain PANI/GNP (1:0.1) composites. This result further demonstrates that the effect of DBSA on the electrochemical properties of PANI/GNP composites relies on the composition ratio of composites.

Table 5.1.1 Conductivities and capacitive performances of PANI/GNP (1:1) and (1:0.1) composites with FeCl₃ as oxidant.

Samples	Conductivity at 30 MPa (S cm ⁻¹)	Specific capacitance at 20 mV s ⁻¹ (F g ⁻¹)	Retention of specific capacitance at 100 mV s ⁻¹ (%)
PANI/GNP-1-2.3-0	0.49±0.02	31.6	113.0
PANI/GNP-1-2-0	0.58±0.04	33.8	110.4
PANI/GNP-1-1-0	2.26±0.05	19.8	113.3
PANI/GNP-1-2.3-0.97	7.72±0.15	8.7	238.7
PANI/GNP-1-2-0.97	8.12±0.18	9.9	219.3
PANI/GNP-1-1-0.97	10.74±0.40	6.6	272.7
PANI/GNP-0.1-2.3-0	0.002±0.00005	78.8	91.1
PANI/GNP-0.1-2-0	0.003±0.0002	110.9	60.4
PANI/GNP-0.1-1-0	0.03±0.001	94.6	85.6
PANI/GNP-0.1-2.3-0.97	8.26±0.13	100.0	50.3
PANI/GNP-0.1-2-0.97	6.16±0.24	120.7	71.9
PANI/GNP-0.1-1-0.97	5.04±0.10	92.0	73.4

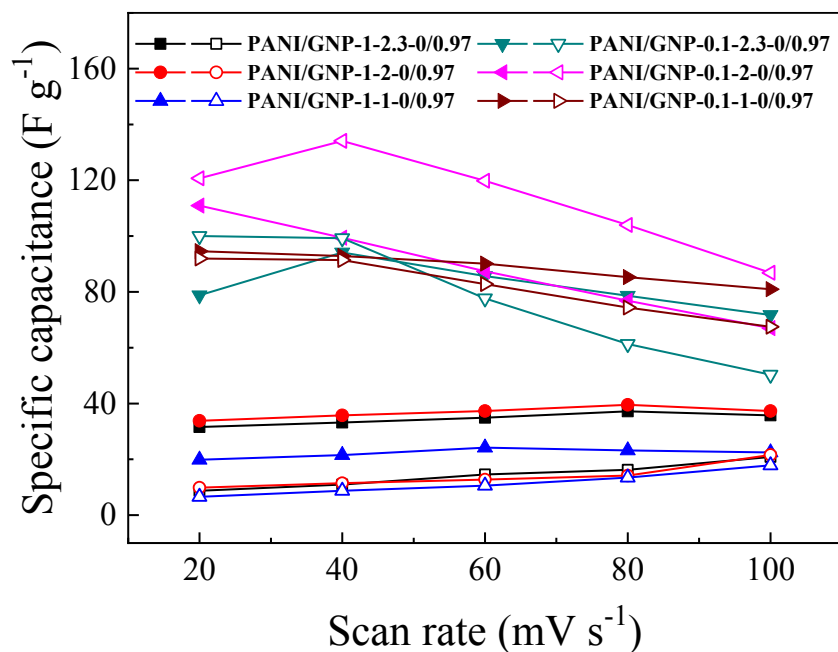


Fig. 5.1.9 Specific capacitance of PANI/GNP (1:1) and PANI/GNP (1:0.1) composites as a function of scan rate (solid symbols: without DBSA; open symbols: with DBSA). [151]

5.1.4. Effect of oxidant nature on electrochemical behavior

In this study, the electrochemical properties of PANI/GNP-APS composites, in which APS were used as oxidant, were also investigated. The cyclic voltammetric performance of PANI/GNP-APS (1:1) and (1:0.1) prepared with a aniline to oxidant molar ratio of 1:1 and without dopant (PANI/GNP-1-1-0-APS and PANI/GNP-0.1-1-0-APS) were tested and compared to that of the corresponding PANI/GNP composites, which used FeCl_3 as oxidant. In the Fig. 5.1.10 (a) and (b), the cyclic voltammograms of both PANI/GNP-1-1-0-APS and PANI/GNP-0.1-1-0-APS composites exhibit two pairs of characteristic redox peaks, which are related to the faradaic transformation of different PANI states. The anodic peaks and cathodic peak shift positively and negatively, respectively, with the increase of scan rate. The emeraldine/pernigraniline anodic peaks of PANI/GNP-APS (1:0.1) composite, marked as A2 in Fig. 5.1.10 (b), shift beyond the potential range at scan rates of 80 mV s^{-1} and 100 mV s^{-1} . In comparison, the CV plots of PANI/GNP-APS (1:1) composite are symmetric, but those of PANI/GNP-APS (1:0.1) composite are asymmetric at high potential scan rate. With the scan rate increasing, the CV loop area of PANI/GNP-APS (1:1) steadily enlarges, but the increase rate of the CV integral area for PANI/GNP-APS

(1:0.1) composite is not steady. In a word, PANI/GNP-APS (1:1) showed better rate capability than the PANI/GNP-APS (1:0.1) composite.

The CV plots of PANI/GNP-APS composites at a scan rate of 20 mV s^{-1} are compared to those of the corresponding PANI/GNP prepared using FeCl_3 as oxidant in Fig. 5.1.10 (c). It can be seen that cyclic voltammograms of PANI/GNP-APS composites show larger magnitude of current density and integral area than those of PANI/GNP composites using FeCl_3 as oxidant. The larger specific capacitances of PANI/GNP-APS composites compared to those of PANI/GNP composites illustrated in Fig. 5.1.10 (d) and Table 5.1.2 further demonstrates that using APS as oxidant is better than using FeCl_3 composites for the electrochemical performance of PANI/GNP (1:1) and (1:0.1) composites. This phenomenon can be attributed to the dependence of conductivity of PANI/GNP composites on the type of oxidant. As shown in Table 5.1.2, the conductivities of PANI/GNP-APS (1:1) and (1:0.1) composites are much higher than those of PANI/GNP (1:1) and (1:0.1) composites using FeCl_3 as oxidant (Table 5.1.1). Fig. 5.1.11 shows that the PANI in PANI/GNP-APS composites exhibit micro-fibrillar networks, but the PANI in the PANI/GNP using FeCl_3 as oxidant own drop-like structure. Basavaraja *et al.* has reported similar changes of the PANI morphologies with the type of oxidant [162]. It is obvious that compared to a drop-like morphology, a micro-fibrillar network own larger surface area and faster electron transfer, which can realize higher conductivity and better electrochemical properties. Another reason for the better capacitive behavior of PANI/GNP-APS composites than the PANI/GNP composites using FeCl_3 is the higher actual content of PANI in the composites as shown in Fig. 5.1.4 (b).

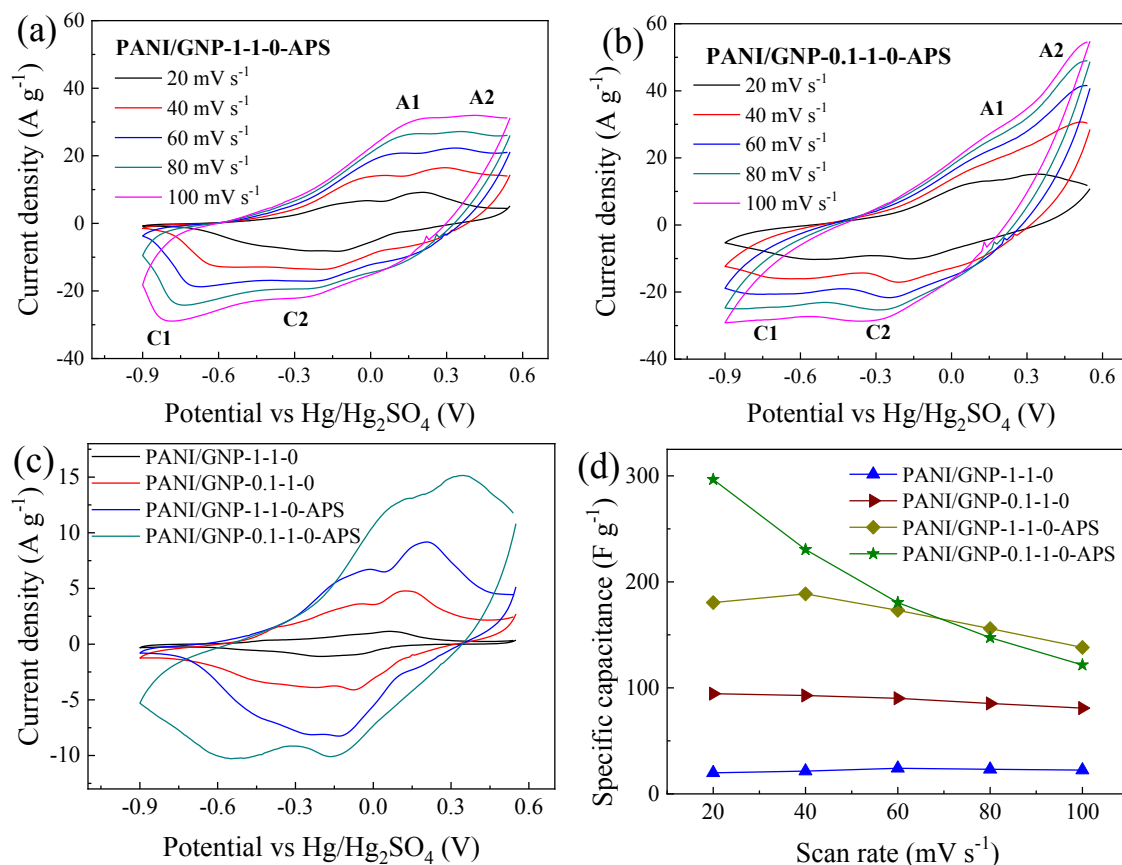


Fig. 5.1.10 (a, b) Cyclic voltammograms of PANI/GNP composites with APS as oxidant at different scan rates; (c) cyclic voltammograms of selected PANI/GNP composites with FeCl_3 or APS as oxidant at a scan rate of 20 mV s^{-1} ; (d) specific capacitance of PANI/GNP composites with FeCl_3 or APS as oxidant as a function of scan rate. [151]

Table 5.1.2 Conductivities and capacitive performances of PANI/GNP (1:1) and (1:0.1) composites with APS as oxidant.

Sample	Conductivity at 30 MPa (S cm^{-1})	Specific capacitance at 20 mV s^{-1} (F g^{-1})	Retention of specific capacitance at 100 mV s^{-1} (%)
PANI/GNP-1-1-0-APS	12.85 ± 1.59	180.5	76.6
PANI/GNP-0.1-1-0-APS	1.95 ± 0.30	296.6	41.0

In Fig. 5.1.10 (c), PANI/GNP-APS (1:0.1) composite shows larger magnitude of current density and integral areas of the CV plots at a scan rate of 20 mV s^{-1} than the PANI/GNP-APS (1:1) composite. According to Fig. 5.1.10 (d) and Table 5.1.2, the PANI/GNP-APS (1:0.1) composite exhibits larger specific capacitance than

PANI/GNP-APS (1:1) composite at low scan rates (20 mV s^{-1} and 40 mV s^{-1}), but shows worse rate capability. At a high scan rate of 100 mV s^{-1} , the specific capacitance of PANI/GNP-APS (1:1) composite becomes higher than that of PANI/GNP-APS (1:0.1) composite. The result is due to the essential role of GNP for the electrochemical stability of the PANI/GNP composites. Among the PANI/GNP and PANI/GNP-APS composites investigated in this chapter, the PANI/GNP-1-1-0-APS, which own a PANI to GNP ratio of 1 to 0.1 and use APS as oxidant, shows the best combination of high specific capacitance and good rate capability. It owns a specific capacitance of 180.5 F g^{-1} at a scan rate of 20 mV s^{-1} and still retains 76.6 % of the specific capacitance at 100 mV s^{-1} .

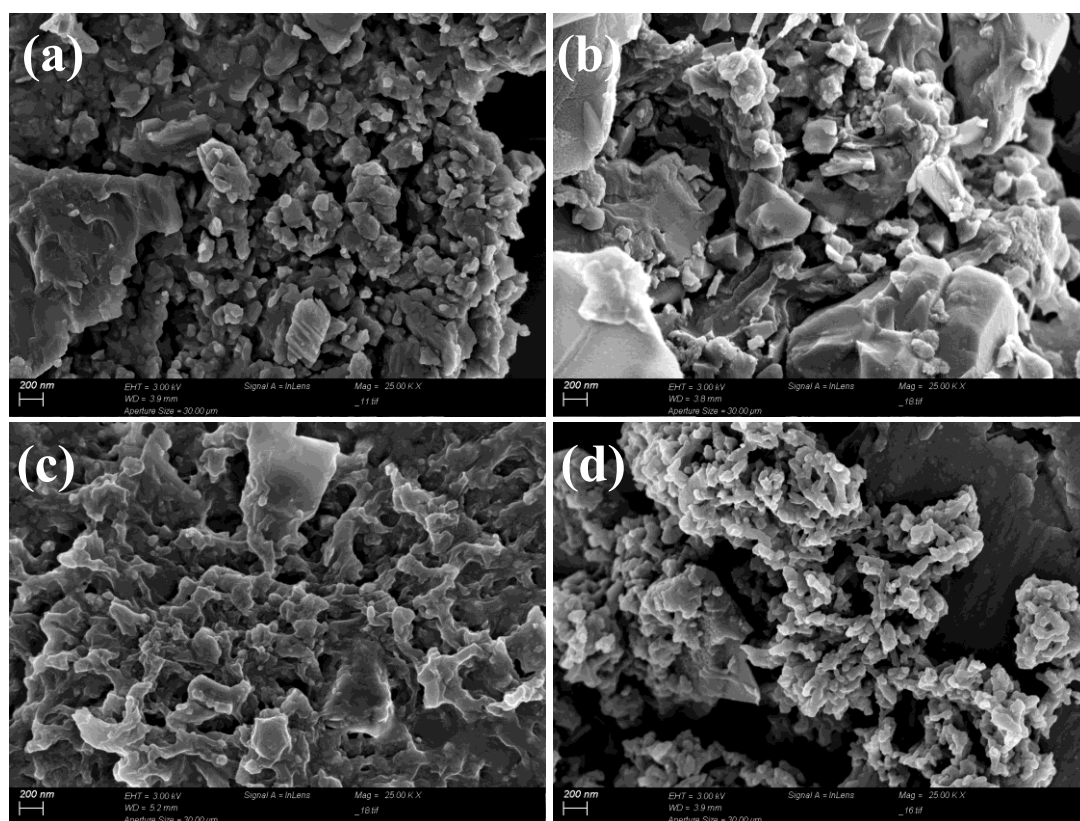


Fig. 5.1.11 SEM images of (a) PANI/GNP-1-1-0, (b) PANI/GNP-0.1-1-0, (c) PANI/GNP-1-1-0-APS and (d) PANI/GNP-0.1-1-0-APS composites. The scale bar in the figures is 200 nm. [151]

5.1.5. Summary

For the polyaniline/graphite nanoplates (PANI/GNP) composites prepared by in-situ polymerization of aniline in the presence of GNP, their electrochemical properties rely on the preparation parameters, such as oxidant, dopant and composition ratio. The relationship between the addition of dopant DBSA and the capacitance of PANI/GNP composites depends on the composition ratio, since DBSA increased the conductivities of composites on the one hand but impeded the capacitive performance of PANI on the other hand. Compared to the droplet-like morphology of PANI/GNP composites using FeCl_3 as oxidant, the PANI/GNP-APS composites with fibrillar morphology own higher conductivity. Moreover, using APS instead of FeCl_3 was beneficial to transfer of aniline into PANI, thus the obtained PANI/GNP-APS composite owned higher content of PANI and showed higher capacitance. For a PANI/GNP composite, the pseudocapacitance of PANI contributed more than the electrochemical double layer capacitance of GNP to the overall capacitance of composites. But the GNP largely enhanced the conductivity and rate capability of PANI/GNP composites. The PANI/GNP-0.1-1-0-APS composite, which owned a low weight ratio of GNP to aniline (0.1:1), without DBSA, and used APS as oxidant, exhibited the highest specific capacitance of 296.6 F g^{-1} at a low scan rate of 20 mV s^{-1} but presented low rate capability. The PANI/GNP-1-1-0-APS, which prepared with a GNP to aniline weight ratio of 1:1, is suitable to be used as supercapacitor electrodes, since it showed a combination of high specific capacitance (180.5 F g^{-1} at 20 mV s^{-1}) and good rate capability.

5.2. PANI/(GO-PDA) and PANI/GO-PDA composites

5.2.1. Introduction

In the previous section of research (chapter 5.1), the effect of synthesis parameters on the electrochemical behavior of PANI/GNP composites was investigated. The interaction between the carbon filler (GNP) and PANI is mainly the weak π conjugation. It has been reported that besides the structural instability of PANI, the poor attachment of PANI on the carbon filler also weakens the electrochemical stability of carbon-based PANI composites. [163] Herein, the graphite oxide (GO) was chosen as the carbon filler, since functional groups and structural defects on the GO were expected to show stronger interaction with PANI compared to the π conjugation. Moreover, the polydopamine (PDA) was used to functionalize and reduce the GO, aiming to further enhance the interaction between PANI and GO and increase the conductivity of GO. PDA is an eco-friendly polymer mimicking the adhesive protein in the pads of mussels. [164, 165] It can be easily synthesized via self-polymerization of dopamine in a weak alkaline solution. Interestingly, some researchers reported that the polymerization process of PDA could simultaneously reduce GO into reduced graphite oxide (rGO). The schematic diagram of the reduction process is shown in Fig. 5.2.1 (a). The reduction mechanism is the release of electrons during the oxidative polymerization of dopamine [166] and the covalent grafting between active sites of GO and molecules of dopamine. [167] Besides, the PDA coated on rGO can prevent the agglomeration of rGO. [168, 169] However, the reduction effect of PDA on GO is controversial. Some studies indicate that PDA cannot or could only partly reduce GO into rGO. [167, 170] Qu *et al.* carbonized GO-PDA hybrids by high temperature reduction method. [171] Thangavalu *et al.* reduced GO/PDA composite into rGO/PDA composite by electrochemical reduction method. [172] On the other hand, the catechol functional groups in PDA are expected to interact with the amine functional groups in PANI. [173] A possible interaction between PDA and PANI is illustrated in Fig. 5.2.1 (b). Wang and Lee [163] have reported that the modification effect of PDA can improve the electrochemical cycle stability of PANI/single wall carbon nanotube composites.

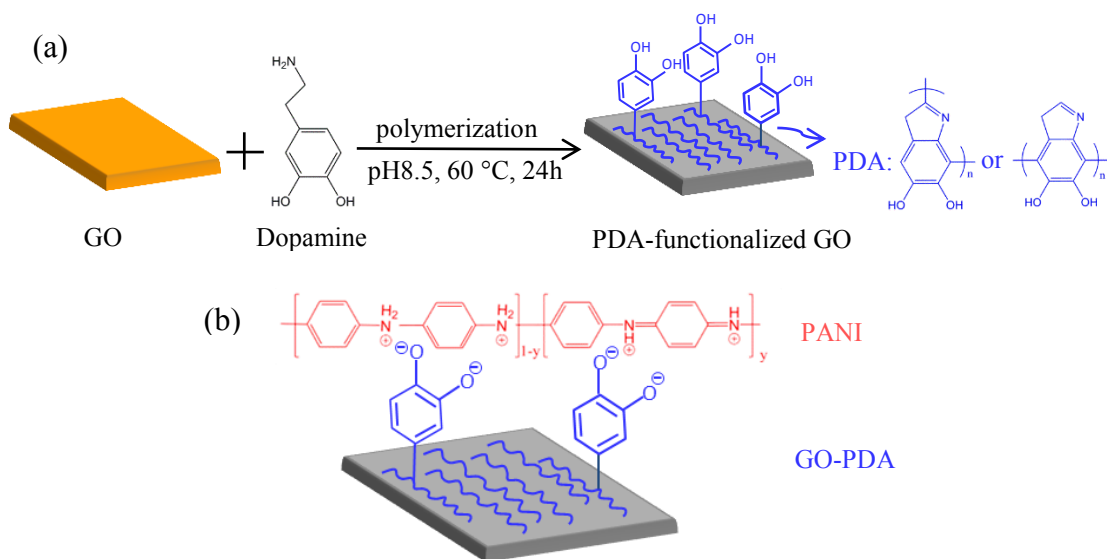


Fig. 5.2.1 Schematic illustrations of (a) the synthesis of PDA-functionalized GO (GO-PDA); (b) possible interaction between GO-PDA and PANI.

In this chapter, the reduction effect of PDA on GO and the influence of PDA on the morphology and electrochemical properties of PANI/GO composite were investigated. Considering the result of last section, PANI/GO (1:0.1) composites without dopant and using APS as oxidant were chosen for the investigations in this section. The PANI/PDA-functionalized GO composites were prepared by two different routes. The composites named as PANI/(GO-PDA) were prepared by producing GO-PDAs (the GO partly reduced during the polymerization of dopamine) in the first step and then in-situ polymerising aniline. The composites named as PANI/GO-PDA were produced by in-situ polymerization of aniline in GO solution firstly, and then the PANI/GO composites were functionalized by PDA.

5.2.2. Structural characterization of PDA-functionalized GO

GO used in this research was chemically oxidized from EG by an improved oxidation method. Then the GO was functionalized with PDA during the process of in-situ polymerization of dopamine. In the latter reaction, GO to dopamine mass ratios of 1: 0.5, 1:0.8, and 1:1.1 were selected, and the corresponding products were labelled as GO-PDA0.5, GO-PDA0.8 and GO-PDA1.1, respectively. Fig. 5.2.2 (a) shows the X-ray diffraction (XRD) spectra of EG, GO, and GO-PDAs. The fine powder-like GO and GO-PDAs samples were tested in quartz glass capillary tubes. While the platelet-like

EG sample was tested in aluminium (Al) foils, which resulted in an additional Al diffraction peak at 38.4° . The XRD pattern of EG presents peaks at $2\theta = 26.6^\circ$ and 44.6° , corresponding to (002) and (101) planes, respectively. When the EG oxidized into GO, the peak at 26.6° , which corresponds to an interlayer distance of $d=0.34$ nm, disappears and a characteristic (001) peak at $2\theta=10.7^\circ$ ($d=0.83$ nm) occurs. After the functionalization of GO by PDA, the intensity of the (001) diffraction peak of GO becomes much weaker. The position of this peak in the XRD pattern of GO-PDA0.5, which is marked by an arrow in the Fig. 5.2.2 (a), moved to smaller 2θ value compared to that of GO. With the increase of PDA amount, the 2θ value of this weak peak decrease continuously, indicating the interlayer distance increases. This change might attribute to intercalation of PDA. Except for the movement of this weak peak, the XRD patterns of GO-PDA0.5, GO-PDA0.8 and GO-PDA1.1 are similar. They all present a very broad diffraction peak around $2\theta=23.4^\circ$, assigned to an interlayer distance of $d=0.38$ nm. The appearance of this peak and the dramatically weakened GO typical peak both mean the GO has been partly reduced by PDA. But the reduction degree does not increase with increasing the PDA content in this study. The thermal stability of EG, GO, and GO-PDAs under nitrogen atmosphere with temperature increasing from ambient temperature to 800°C with a rate of $10^\circ\text{C min}^{-1}$ was investigated. The thermogravimetric (TG) curves of GNP, GO and GO-PDAs are illustrated in Fig. 5.2.2 (b). The graphite nanoplates (GNP) is exfoliated from EG by ultra-sonication method as described in the chapter 4.2.1. Therefore, the TG behavior of EG is as same as that of GNP, which is thermally stable below 800°C as shown in Fig. 5.2.2 (b). The TG curve of GO shows a slight weight loss below 130°C and an obvious weight loss at around 200°C , which are corresponding to the evaporation of physically adsorbed water and the decomposition of labile oxygen functional groups, respectively. [164] The GO-PDA0.5 shows similar thermal decomposition temperature as the GO, but exhibits much lower weight loss. The total weight losses of GO and GO-PDA0.5 below 800°C are 65.4 % and 41.4 %, respectively. On the other hand, the TG curves of GO-PDA0.5, GO-PDA0.8, and GO-PDA1.1 almost overlap. The weight losses of GO-PDA0.8 and GO-PDA1.1 below 800°C are 41.3 % and 40.1 %, respectively.

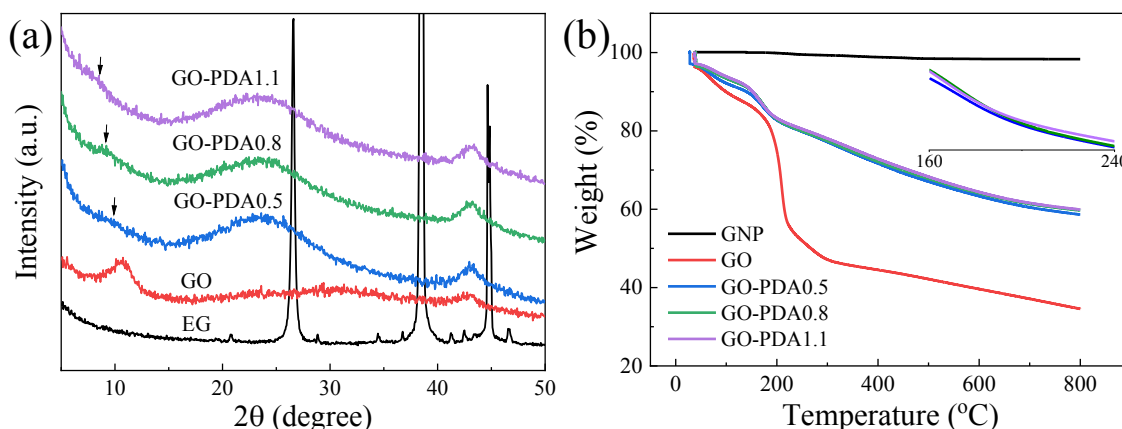


Fig. 5.2.2 XRD patterns (a) and thermogravimetric analysis (b) of EG, GO, and GO-PDAs.

Fourier-transform infrared attenuated total reflectance spectroscopy (FTIR/ATR) and ultraviolet-visible spectroscopy (UV-vis) were employed to further investigate the structure of GO and GO-PDAs. As shown in Fig. 5.2.3 (a), the FTIR/ATR spectrum of GO exhibits typical peaks of oxygen-containing functional groups. The peaks at 3196 cm^{-1} , 1730 cm^{-1} , 1617 cm^{-1} , and 1040 cm^{-1} are assigned to the stretching of OH vibration, stretching of C=O vibration, asymmetric stretching of -COO vibration, and stretching of C-O vibration, respectively. [164] After the modification with PDA, the FTIR/ATR spectrum of GO-PDA0.5 does not show the broad peak at 3250 cm^{-1} and the peak at 1617 cm^{-1} , and the typical peaks of GO at 1730 cm^{-1} and 1040 cm^{-1} also largely diminished. These changes demonstrate the GO has been partly reduced by PDA. Additionally, in the FTIR/ATR spectrum of GO-PDA0.5, a new peak at 1568 cm^{-1} appears which can be attributed to the N-H bond in the PDA. [174, 175] On the other hand, the change of PDA content has a negligible influence on the FTIR/ATR behavior of GO-PDAs. The UV-vis spectra of GO and GO-PDAs are illustrated in Fig. 5.2.3 (b). The GO sample was tested in Millipore water, and GO-PDAs were tested in N-Methyl-2-pyrrolidone (NMP) solvent. The UV-vis spectrum of GO shows a maximum absorption at around 220 nm, which is corresponding to the $\pi\text{-}\pi^*$ transition of aromatic C=C. After the functionalization with PDA, the adsorption peaks shift to 264 nm, 266 nm, and 263 nm in the spectra of GO-PDA0.5, GO-PDA0.8 and GO-PDA1.1, respectively. These shifts are attributed to the restoration of the π -conjugation network and reflect the partial reduction of GO-PDAs. [176]

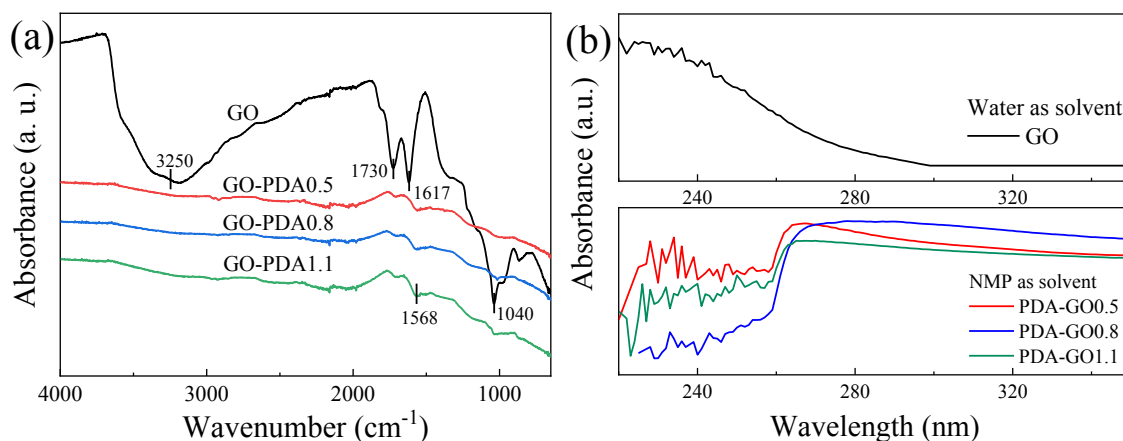


Fig. 5.2.3 FTIR/ATR (a) and UV-vis (b) spectra of GO and GO-PDAs.

It is commonly known that with the reduction of graphite oxide into rGO, it becomes conductive, and the conductivity increases with reduction degree. In terms of the electrochemical property of the carbon-based PANI composite, the conductive rGO is beneficial to the electron transformation compared to the insulating GO. Therefore, in this study, the conductivities of the powder-like GO-PDA products were tested under a pressure of 30 MPa by an in-house built device. It is interesting to see in Table 5.2.1 that even though the reduction effect of PDA endows GO-PDAs with conductivity, the conductivity of GO-PDAs decrease with the content of PDA. Moreover, the conductivities of GO-PDAs are significantly lower (five to six orders of magnitude) than the conductivity of EG. This phenomenon can be attributed to the negative effect of non-conductive PDA on the overall conductivity of GO-PDAs and the low reduction degree of GO-PDAs.

Table 5.2.1 Conductivities of GO and GO-PDAs.

Sample	Conductivity at 30 MPa (S cm ⁻¹)
EG	17.6
GO	not conductive
GO-PDA0.5	3.0E-4
GO-PDA0.8	1.1E-4
GO-PDA1.1	3.5E-5

5.2.3. Electrochemical properties and morphology of PANI/GO-PDA composites

The PANI/GO-PDA composites were synthesized by in-situ polymerization of PANI in the GO solution followed by modification of the PANI/GO (1:0.1) composites by different content of PDA. In the second step, the mass ratios of GO to PDA were set at 0.5, 0.8, and 1.1, and the final composites were labelled as PANI/GO-PDA (1/0.1-0.5), PANI/GO-PDA (1/0.1-0.8), and PANI/GO-PDA (1/0.1-1.1), respectively. Standard cyclic voltammetric (CV) test was applied to understand the electrochemical redox behavior of PANI/GO-PDA composites. Fig. 5.2.4 shows the cyclic voltammograms of pure PANI, PANI/GO composite, and PANI/GO-PDA composites. The cyclic voltammogram of PANI at 20 mV s^{-1} shows two pairs of redox peaks. The anodic peak A_1 and cathodic peak C_1 are corresponding to the reaction between the fully-reduced PANI state (leucoemeraldine) and partly-oxidized PANI state (emeraldine). The anodic peak A_2 and cathodic peak C_2 are related to the transition between emeraldine and fully-oxidized state PANI (pernigraniline). In the CV curves of PANI at scan rates of 40 mV s^{-1} , 60 mV s^{-1} , 80 mV s^{-1} , and 100 mV s^{-1} only one pair of redox peaks (A_1/C_1) can be observed. The absent of the redox peaks A_2/C_2 is because the current density of A_2/C_2 is usually much lower than that of A_1/C_1 . But it does not mean that there is no reaction between the emeraldine and pernigraniline. [163] Moreover, the current density increases with the scan rate increasing from 20 mV s^{-1} to 100 mV s^{-1} , which can be attributed to the internal resistance of electrode.

The cyclic voltammograms of PANI/GO (1:0.1) and PANI/GO-PDA (1:0.1) composites show similar shape as the CV curves of pure PANI, since the PANI is the major part in the composites. The magnitude of CV plots of PANI/GO (1:0.1) composite is lower than the magnitude of the CV plots of pure PANI at the same potential scan rates. Adding PDA with a GO to PDA mass ratio of 1 to 0.8 significantly increases the CV magnitude of PANI/GO (1:0.1) composite. But the magnitude of CV plot decrease with further increase of the GO to PDA mass ratio from 1 to 1.1. In order to intuitively compare the magnitude of CV plots, Fig. 5.2.5 (a) shows the cyclic voltammograms of PANI, PANI/GO (1:0.1) composite, and PANI/GO-PDA (1:0.1) composites at a scan rate of 20 mV s^{-1} . And Fig. 5.2.5 (b) presents the plots of specific capacitance of PANI, PANI/GO (1:0.1) composite and PANI/GO-PDA (1:0.1) composites, which were calculated based on the CV results according to Equation 4.3.1,

as a function of the potential scan rate. The magnitude of CV plots at 20 mV s^{-1} in Fig. 5.2.5 (a) and the specific capacitance value in Fig. 5.2.5 (b) are following the same sequence: PANI/GO-PDA (1/0.1-0.5) < PANI/GO (1:0.1) < PANI/GO-PDA (1/0.1-1.1) < PANI < PANI/GO-PDA (1/0.1-0.8).

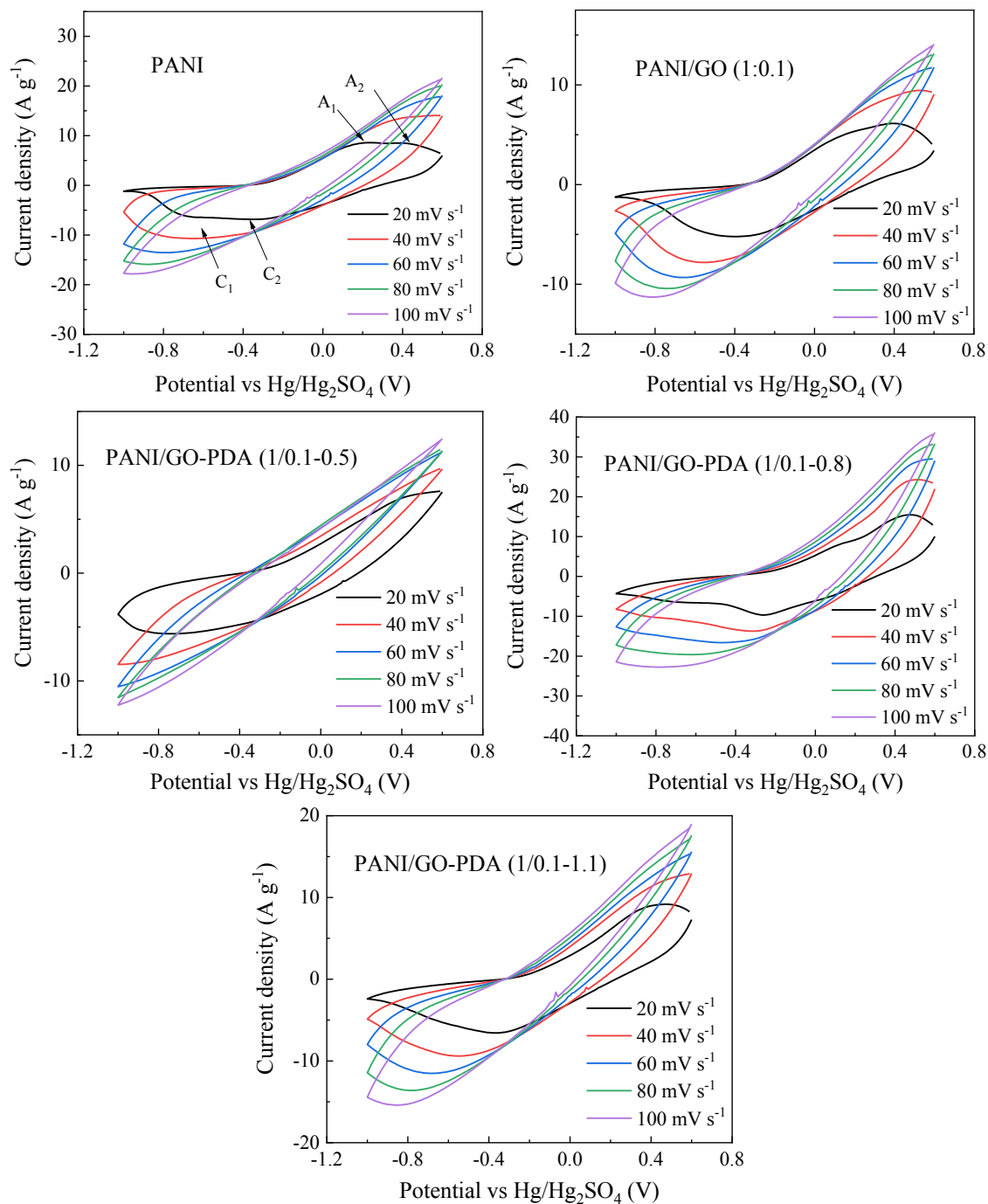


Fig. 5.2.4 Cyclic voltammograms of pure PANI and PANI/GO-PDA (1:0.1) composites at different scan rates.

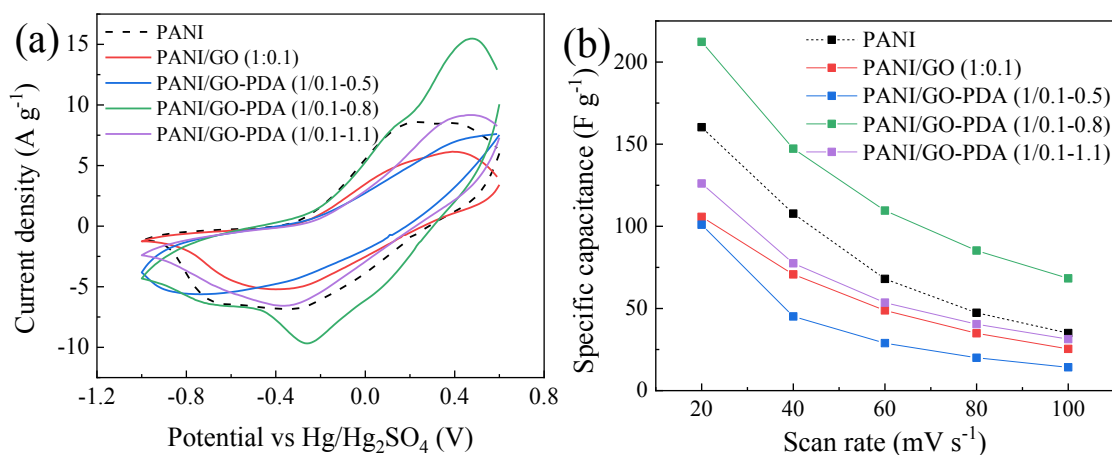


Fig. 5.2.5 (a) Cyclic voltammograms at a scan rate of 20 mV s⁻¹ and (b) the specific capacitance of PANI and PANI/GO-PDA (1:0.1) composites as a function of scan rate.

The electrochemical property of a material is tightly related to its morphology, conductivity, and specific surface area. Therefore, the morphology of PANI, PANI/GO (1:0.1), and PANI/GO-PDA (1:0.1) composites were investigated by scanning electron microscopy (SEM). As shown in Fig. 5.2.6, the pure PANI presents fibrillar network morphology. In comparison, the PANI phase in the PANI/GO (1:0.1) composites shows much different morphology. The PANI nanowire arrays are vertical to the GO sheets and form coated layers on the surface of GO sheets. Xu *et al.* has also reported this kind of morphology of PANI/GO composites. [177] They explained that the oxygen functional groups of GO and π - π interaction between phenyl of aniline and basal planes of GO were beneficial to the nucleation and growth of PANI nanowire arrays, respectively. On the other hand, the morphologies of PANI/GO-PDA (1:0.1) composites are similar to the morphology of PANI/GO (1:0.1) composite.

The conductivity and Brunauer-Emmett-Teller (BET) specific surface area of PANI/GO-PDA (1:0.1) composites were detected by an in-house built device and a Tensor 27 spectrometer, respectively. The results are illustrated in Fig. 5.2.10. With the mass ratio of GO to PDA increase from 0.5 to 0.8 and then to 1.1, the BET specific surface area of PANI/GO-PDA (1:0.1) composites increases firstly and then slightly decreases. However, all the PANI/GO-PDA (1:0.1) composites are not conductive. In summary, the method of synthesizing PANI/GO followed by reduction of GO component by dopamine polymerization can realize vertically growth of PANI arrays

on the GO-PDA surface, but the conductivity of PANI/GO-PDA composite was obstructed due to the functionalization of the insulating PDA. The order of specific capacitance of PANI/GO-PDA composites is in consistence with the order of specific surface area shown in Figure 5.2.10, i.e. PANI/GO-PDA (1/0.1-0.5) < PANI/GO-PDA (1/0.1-1.1) < PANI/GO-PDA (1/0.1-0.8).

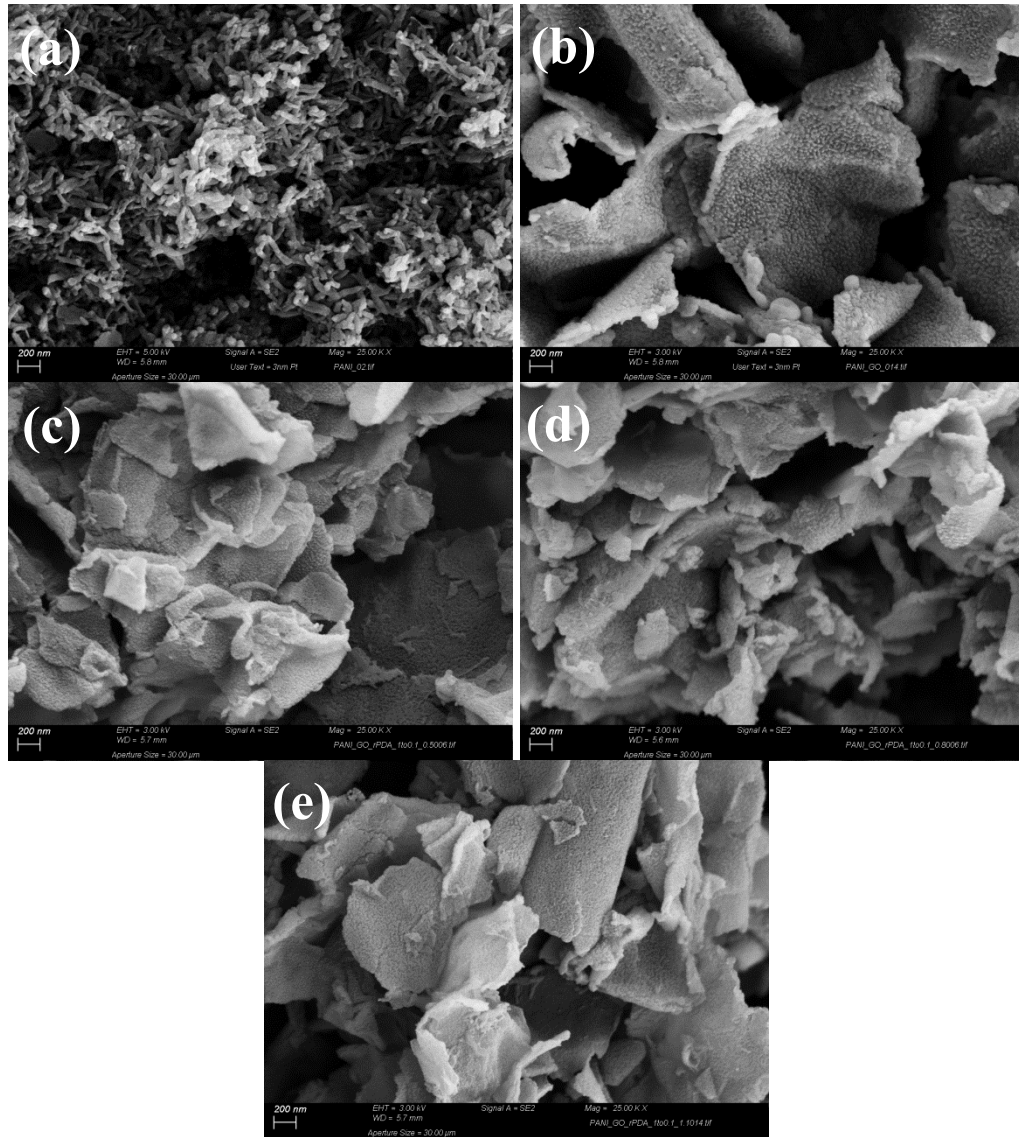


Fig. 5.2.6 SEM images of (a) PANI, (b) PANI/GO (1:0.1), (c) PANI/GO-PDA (1/0.1-0.5), (d) PANI/GO-PDA (1/0.1-0.8), and (e) PANI/GO-PDA (1/0.1-1.1) composites. The scale bar in all images is 200 nm.

5.2.4. Electrochemical properties and morphology of PANI/(GO-PDA) composites

PANI/(GO-PDA) composites were produced by modifying GO by PDA in the first step and then synthesizing the composites of PANI and the GO-PDA. Fig. 5.2.7 shows the cyclic voltammograms of PANI/(GO-PDA) composites. The CV curves present similar shapes as the CV plots of PANI and PANI/GO-PDA composites as illustrated in Fig. 5.2.4. The redox peaks A_1/C_1 and A_2/C_2 can be observed in the CV plots of PANI/(GO-PDA) composites at low potential scan rate. The scale ranges of X and Y axis of the three plots in Fig. 5.2.7 are the same. With the increase of PDA to GO mass ratio from 0.5 to 0.8 and then to 1.1, the CV plot at the same scan rate shows gradually declined integral area.

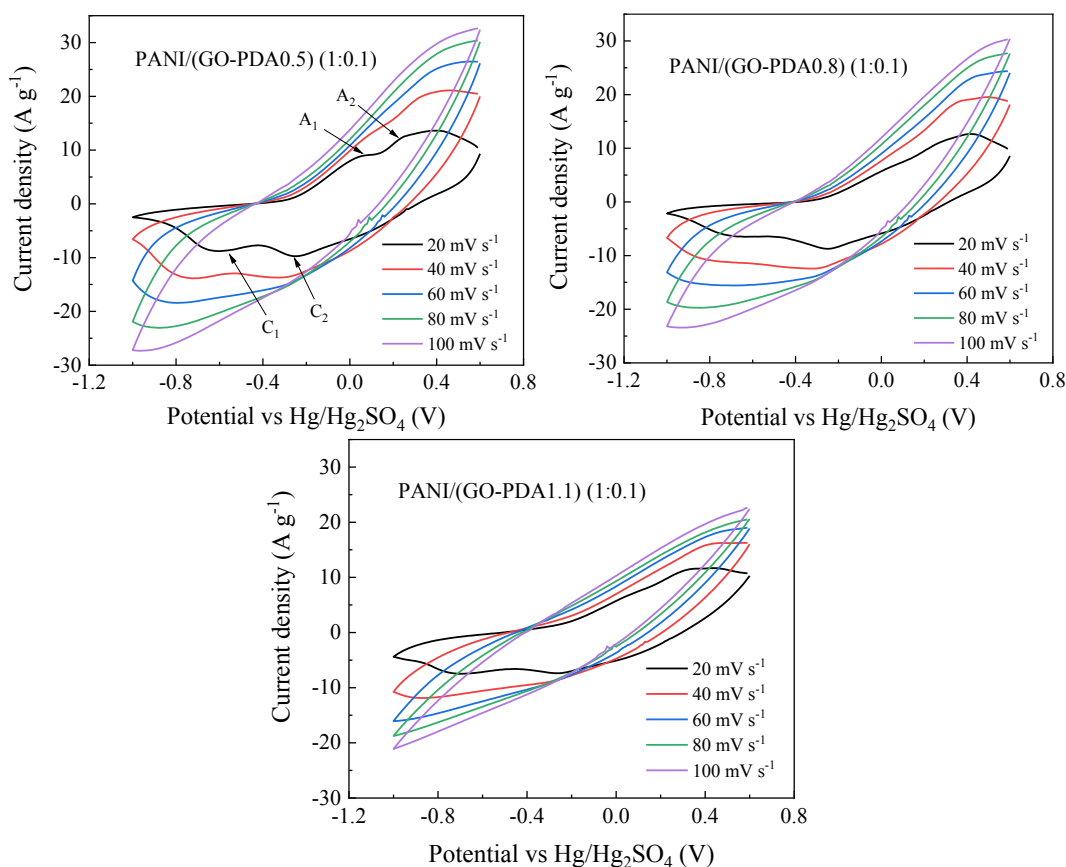


Fig. 5.2.7 Cyclic voltammograms of PANI/(GO-PDA) (1:0.1) composites at different scan rates.

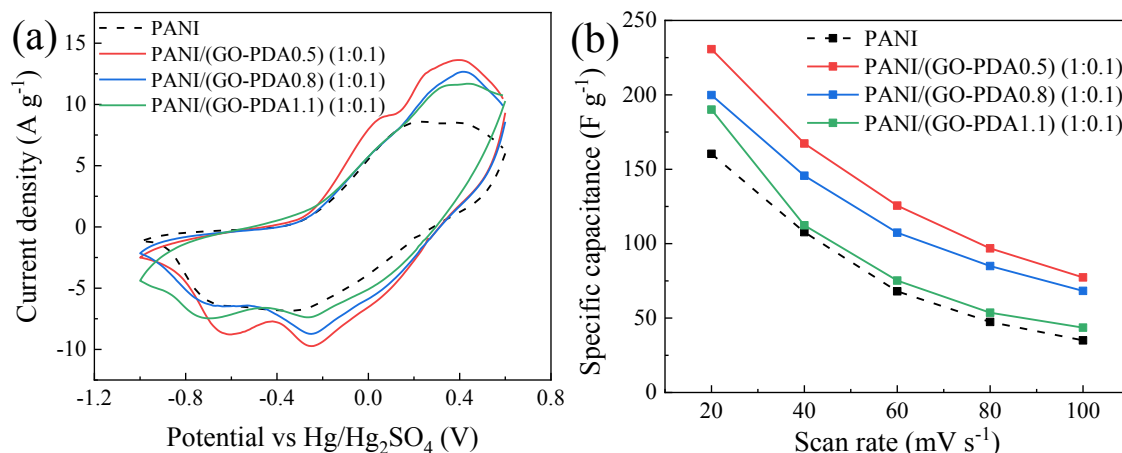


Fig. 5.2.8 (a) Cyclic voltammograms at a scan rate of 20 mV s⁻¹ and (b) the specific capacitance of PANI/(GO-PDA) (1:0.1) composites as a function of scan rate.

Table 5.2.2 Capacitive performances of PANI, PANI/GO, and PANI/GO-PDA and PANI/(GO-PDA) composites.

Sample	Specific capacitance at 20 mV s ⁻¹ (F g ⁻¹)	Retention of specific capacitance at 100 mV s ⁻¹ (%)
PANI	160.3	21.8
PANI/GO (1:0.1)	105.8	24.0
PANI/GO-PDA (1/0.1-0.5)	101.0	14.1
PANI/GO-PDA (1/0.1-0.8)	212.3	32.2
PANI/GO-PDA (1/0.1-1.1)	126.1	24.8
PANI/(GO-PDA0.5) (1:0.1)	230.7	33.5
PANI/(GO-PDA0.8) (1:0.1)	199.8	34.2
PANI/(GO-PDA1.1) (1:0.1)	190.1	22.9

The cyclic voltammograms of PANI/(GO-PDA) composites at a potential scan rate of 20 mV s⁻¹ are compared in Fig. 5.2.8 (a). The specific capacitance of PANI/(GO-PDA) composites at different potential scan rates were calculated according to the CV plots by Equation 4.3.1. Since the specific capacitance was calculated based on the CV plot, the integral area of CV plots shown in Fig. 5.2.8 (a) and the value of specific capacitance at 20 mV s⁻¹ illustrated in Fig. 5.2.8 (b) and Table 5.2.2 follow the same sequence, i.e. PANI < PANI/(GO-PDA1.1) (1:0.1) < PANI/(GO-PDA0.8) (1:0.1) < PANI/(GO-PDA0.5) (1:0.1). Moreover, the specific capacitances at other scan rates illustrated in Fig. 5.2.8 (b) also follow this order. The specific capacitance of PANI/(GO-PDA0.5) (1:0.1) is 230.7 F g⁻¹ at 20 mV s⁻¹ and retains 33.5 % of the specific capacitance at the scan rate of 100 mV s⁻¹. In comparison, the PANI/GO-PDA

(1/0.1-0.8) composite, which shows the highest specific capacitance in Fig. 5.2.5 (b), owns a lower specific capacitance at 20 mV s^{-1} (212.3 F g^{-1}) and a similar rate capability (retains 32.2 % of specific capacitance at 100 mV s^{-1}).

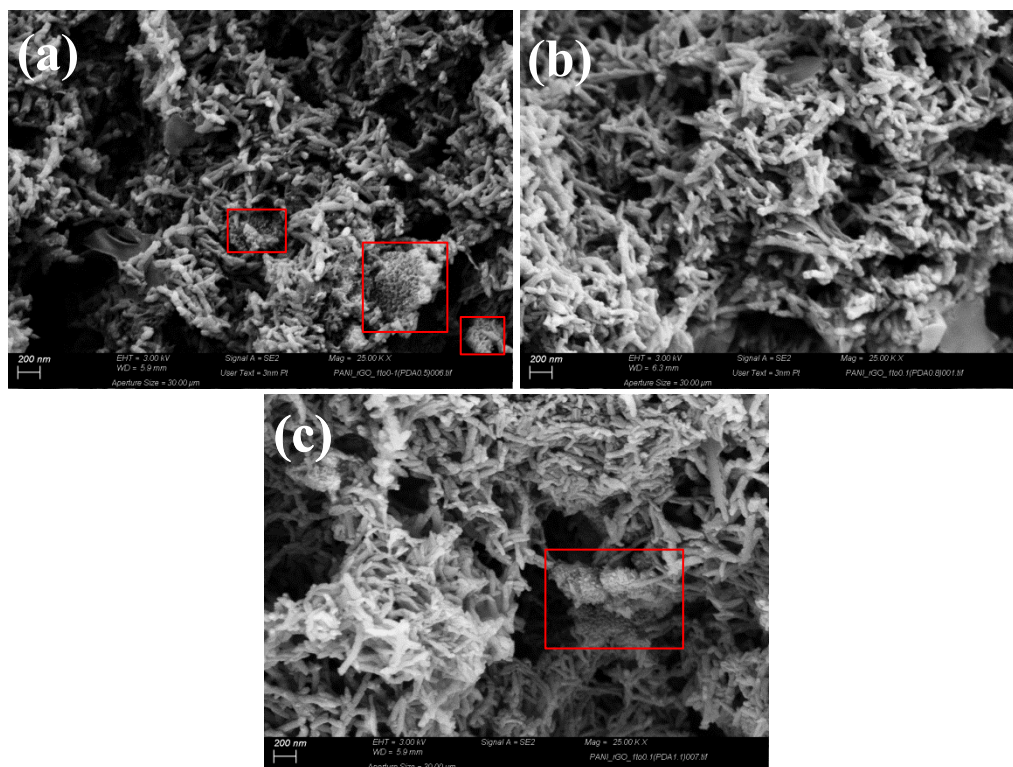


Fig. 5.2.9 SEM images of (a) PANI/(GO-PDA0.5) (1:0.1), (b) PANI/(GO-PDA0.8) (1:0.1), and (c) PANI/(GO-PDA1.1) (1:0.1) composites. The scale bar in all images is 200 nm.

The morphology of PANI/(GO-PDA0.5) (1:0.1), PANI/(GO-PDA0.8) (1:0.1), and PANI/(GO-PDA1.1) (1:0.1) composites were studied by SEM. Their morphologies shown in Fig. 5.2.9 are much different from the morphologies of PANI/GO-PDA composites shown in Fig. 5.2.6. The overwhelming majority of PANI in the PANI/(GO-PDA) composites are fibrillar networks. As marked by the red rectangles in Fig. 5.2.9, there are only few parts of PANI showing a similar morphology as the PANI in PANI/GO and PANI/GO-PDA composites, i.e. nanowire arrays vertically grown on the surface of GO-PDA sheets. The different PANI morphologies in PANI/(GO-PDA) and PANI/GO-PDA composites can be attributed to different surface properties of GO-PDA and GO. After the modification of PDA, lots of oxygen functional groups have been reduced. Therefore, in the polymerization process of aniline, most active

nucleation sites were generated in the bulky solution instead of on the surface of GO-PDA. This phenomenon is in consistence with the study of Xu *et al.* [177] They reported that even for the PANI/GO composites, when the content of aniline is high enough, random connected PANI nanowire were produced by homogeneous nucleation.

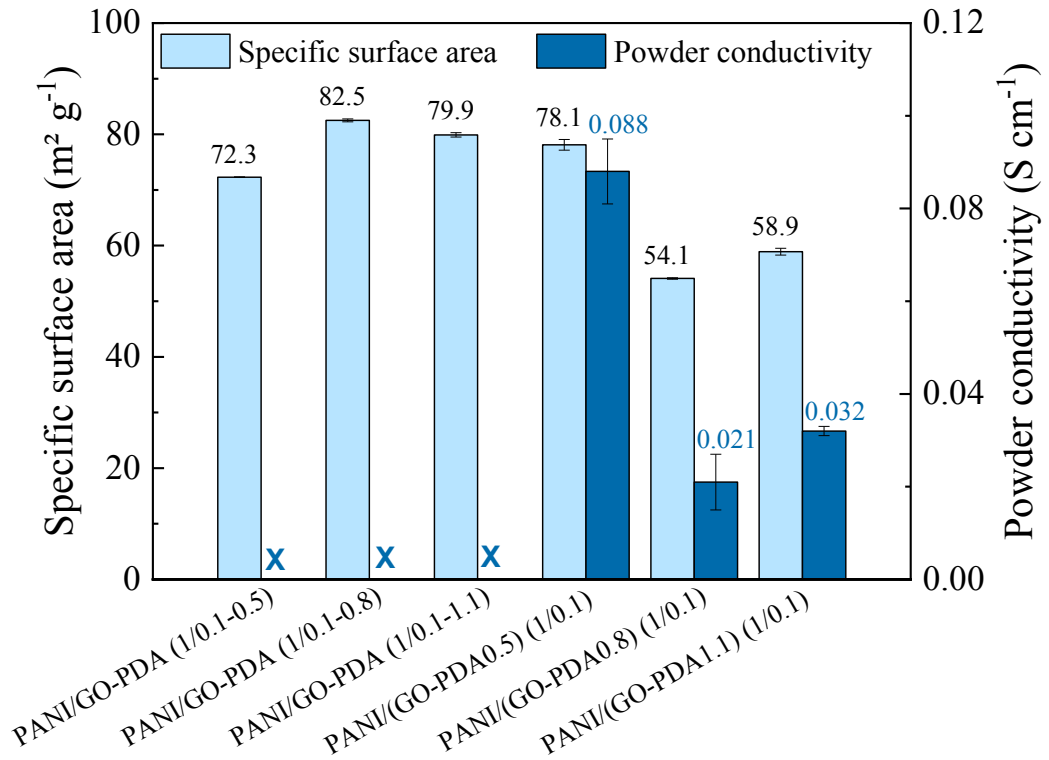


Fig. 5.2.10 Specific surface areas and powder conductivities measured at 30 MPa of PANI/GO-PDA and PANI/(GO-PDA) composites.

Fig. 5.2.10 shows the conductivity measured at 30 MPa and BET specific surface area of all the investigated PANI/(GO-PDA) and PANI/GO-PDA composites. It can be found that except of PANI/GO-PDA (1/0.1-0.5), the PANI/GO-PDA composites show higher specific surface area than the corresponding PANI/(GO-PDA) composites with the same PDA content. The PANI/(GO-PDA) composites show various conductivities; while all the PANI/GO-PDA (1:0.1) composites, which prepared by polymerization of dopamine in the presence of PANI/GO (1:0.1) composite, are not conductive. Among the PANI/(GO-PDA) composites, the PANI/(GO-PDA0.5) (1:0.1) composite exhibits the highest conductivity and the largest specific surface area. These advantages can

explain why the PANI/(GO-PDA0.5) (1:0.1) composite shows the highest specific capacitance in Fig. 5.2.8. However, the lower specific capacitance of PANI/(GO-PDA1.1) (1:0.1) composite compared to PANI/(GO-PDA0.8) (1:0.1) composite cannot be explained from the aspect of specific surface area and conductivity. One possible reason for the higher specific surface area and conductivity but lower specific capacitance of PANI/(GO-PDA1.1) (1:0.1) composite might be some chemical interaction occurring between the excess PDA and PANI. Further investigations are still needed to explain this phenomenon.

5.2.5. Summary

The eco-friendly polydopamine (PDA) was used in this chapter in order to improve the electrochemical property of polyaniline/graphite oxide (PANI/GO 1/0.1) composite. The structural characterization of GO and GO-PDAs by X-ray diffraction, thermogravimetric analysis, Fourier-transform infrared spectroscopy, and ultraviolet-visible spectroscopy indicated that GO has been partly reduced during the synthesis of PDA. Therefore, GO-PDA was conductive, but its conductivity decreased with the increase of dopamine content due to the electrical non-conductivity of PDA. The PANI/GO composites were synthesized by different methods. PANI/GO-PDA composites were produced by functionalizing PANI/GO (1:0.1) composites with different contents of PDA. Their morphologies were similar to PANI/GO composites, i.e. the PANI nanowire array were grown vertically on the GO sheets. Consequently, the specific surface area was large, but they showed non-conductive behavior. PANI/(GO-PDA) composites were synthesized by functionalizing GO by PDA in the first step, and then synthesizing PANI. The PANI in the obtained composites mainly presented fibrillar network morphology. All the PANI/(GO-PDA) composites were conductive. In comparison, the latter synthesis method was more beneficial to the electrochemical property of composites. PANI/(GO-PDA0.5) (1:0.1) composite showed the highest specific capacitance (230.7 F g^{-1} at a scan rate of 20 mV s^{-1}) in this study. Additionally, different from expectation, the addition of PDA could not increase the electrochemical stability of PANI/GO (1:0.1) composites.

5.3. PANI/TA-doped rGO and PANI/TA-doped GNP composites

Note: The work described in chapter 5.3 has been submitted for publication: “Green and Facile Synthesis of Polyaniline/Tannic Acid-rGO Composites for Supercapacitor Purpose” with Minoj Gnanaseelan, Dieter Jehnichen and Jürgen Pionteck as co-authors.

5.3.1. Introduction

Pure PANI supercapacitor electrodes usually show weak long-term cycle stability because of swelling and shrinking caused by the insertion and removal of ions. Adding carbon filler can offer a mechanical support for PANI, promote the internal charge transport and perform an additional EDLC. [178, 179] However, some carbon fillers such as rGO and graphite nanoplates (GNP) tend to agglomerate or restack. [180] Therefore, they cannot uniformly disperse in the composites. Surface modification and adding surfactant are commonly used effective strategies to solve this problem. [28, 181] Coskun *et al.* [182] sulfonated rGO before the synthesis of PANI/rGO composite. Cho *et al.* [183] prepared nanocomposites of poly(4-styrenesulfonic acid) (PSS)-doped PANI and PSS-coated rGO. The PSS acted as dopant for the PANI and as dispersion stabilizer for the rGO. Cai *et al.* [184] used different surfactants to modify rGO and compared the electrochemical properties of final rGO/PANI composites. Tannic acid (TA) is a natural hydrolysable polyphenol which can be extracted from oak, walnut, mahogany and others. TA has been recently demonstrated to be a dispersion stabilizer for graphite. Moreover, it is an effective environmental friendly reducing agent for GO. [176] Yoo *et al.* produced TA-reduced graphene oxide and the as-prepared rGO could be used to detect ammonia gas. [185] Luo *et al.* synthesized three-dimensional TA-reduced rGOs and used them as adsorbents in water purification. [186] However, as far as we know, using TA to prepare PANI/rGO composites for supercapacitor purpose has not been reported.

Besides the advantages of TA mentioned above, the abundant phenolic hydroxyl in tannic acid molecules is expected to present electrostatic interaction with the amine groups of PANI, [187] thereby enhancing the interaction between graphite and PANI (Fig. 5.3.1). In this study, GO reduced by TA (rGO-TA) with different reduction time

and GNP-TA using TA as dispersion stabilizer were synthesized. Their structures were studied by thermogravimetric analysis, X-ray diffraction, and Raman spectroscopy, and compared to structures of rGO-HH (GO reduced by hydrazine hydrate) and GNP. The corresponding PANI/(rGO-TA) (1:0.1 wt./wt.) and PANI/GNP (1:0.1 wt./wt.) composites were produced by in-situ polymerization of aniline in the presence of rGO-TA or GNP. The electrochemical properties and some related influencing factors such as conductivity, specific surface area, and morphology of the obtained PANI/(rGO-TA) and PANI/GNP composites were investigated.

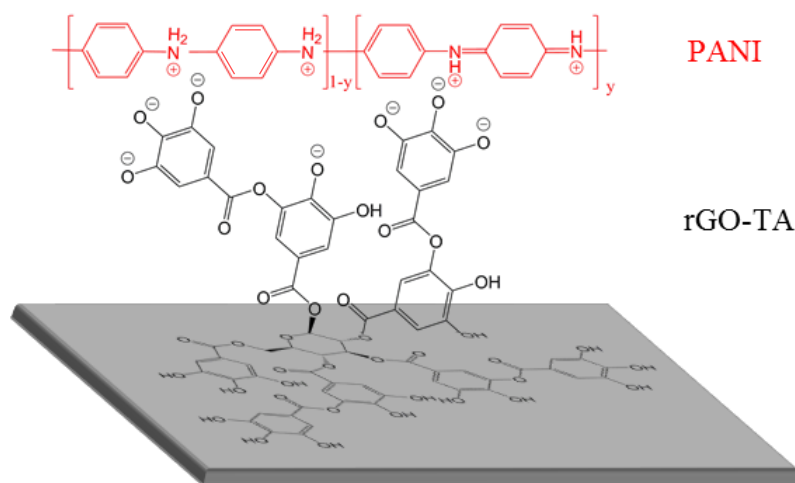


Fig. 5.3.1 Schematic diagram of a possible interaction between PANI and rGO-TA.

5.3.2. Structural characterization of TA-doped rGO and GNP

The rGO-TAs reduced by TA with a time of 2 h, 12 h, and 24 h, and rGO-HH using hydrazine hydrate as reducing agent were synthesized before the production of PANI/rGO composites. Fig. 5.3.2 illustrates the digital photographs of rGO aqueous dispersions, which have stood at ambient temperature for four days. It is obvious that rGO-TA-2h, rGO-TA-12h, and rGO-TA-24h still maintained the homogeneous dispersion in water; while the photographs of rGO-HH and rGO-TA-24h-EOH aqueous dispersions, in which no TA exist, show that rGO-HH and rGO-TA-24h-EOH precipitated out after four days. This phenomenon demonstrates that TA stabilized the aqueous dispersion of rGO. Because dispersion stability of rGO also relies on its reduction degree, here the stabilities of GNP-TA and GNP aqueous dispersions were

investigated. The difference between the photographs of GNP-TA and GNP aqueous dispersions in Fig. 5.3.2 indicates that TA stabilized aqueous dispersion of GNP; this also demonstrates the role of TA as dispersion stabilizer for the rGO.

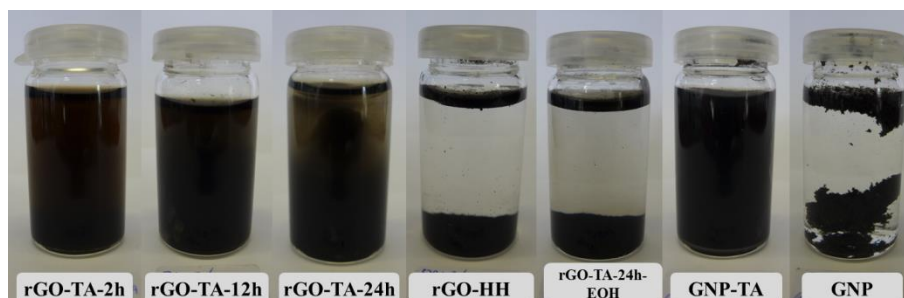


Fig. 5.3.2 Digital photographs of rGOs and GNPs aqueous dispersions after staying four days.

The effects of TA on structural properties of rGO were investigated by different methods. Fig. 5.3.3 (a) illustrates the XRD patterns of EG, GO, and rGOs. An aluminium diffraction peak at 38.4° presents in the XRD spectrum of EG, since EG was tested in an aluminium foil, while other powder-like samples were tested in quartz glass capillary tubes. Besides the Al peak, the XRD pattern of EG shows a sharp peak at $2\theta = 26.6^\circ$ and a small peak at 44.6° , which are corresponding to (002) and (101) planes, respectively. After oxidation, the (002) diffraction peak disappears and the XRD pattern of GO exhibits a broad (001) peak at $2\theta = 10.7^\circ$, assigned to an interlayer distance (d) of 0.83 nm. After modifying GO by TA for 2h, the obtained rGO-TA-2h still owns this (001) diffraction peak but slightly moves to $\sim 10^\circ$, which is corresponding to an interlayer distance of 0.88 nm. This phenomenon indicates that GO has not been reduced by TA after 2 h, and the increase of interlayer distance can be explained by the intercalation of TA. In the XRD spectrum of rGO-TA-12h, the peak at around 10° is moved to around 6° and the intensity of peak strongly decreased. Simultaneously, a very broad peak at 26.2° ($d = 0.34$ nm) appeared, which is similar to carbon black, indicates the loss of the former layered structures. The broadness is indicative for non-uniform layer distance. This broad peak is more intense in the case of rGO-TA-24h, which indicates that the uniformity is increased when the reduction degree is enhanced. Similar broad diffraction peaks at around 26.2° are also shown in the XRD patterns of rGO-HH and rGO-TA-24h-EOH. In addition, the XRD curves of rGO-TA-2h, rGO-TA-

12h, and rGO-TA-24h own sharp reflections at $2\theta = 28.3^\circ$, 25.1° , 20.6° , 17.4° , 13.5° , 12.2° , 9.6° , and few smaller peaks, and the intensity of these reflections raise with reduction time increasing. These reflections disappear in the XRD patterns of rGO-TA-24h-EOH and rGO-HH. These peaks might be attributed to some crystalline impurities in TA. It can be seen in Fig. 5.3.3 (a) that except for a characteristic wide diffraction peak at $2\theta = 25.4^\circ$, the XRD pattern of amorphous TA contains crystalline peaks at $2\theta = 27.8^\circ$ and 16.3° . Another possible reason for those sharp peaks in the XRD patterns of rGO-TAs might be conversion products of TA and the residue manganese ions in the synthesized GO. Li *et al.* reported similar XRD crystalline diffraction peaks of metal-TA nanocomplexes. [188]

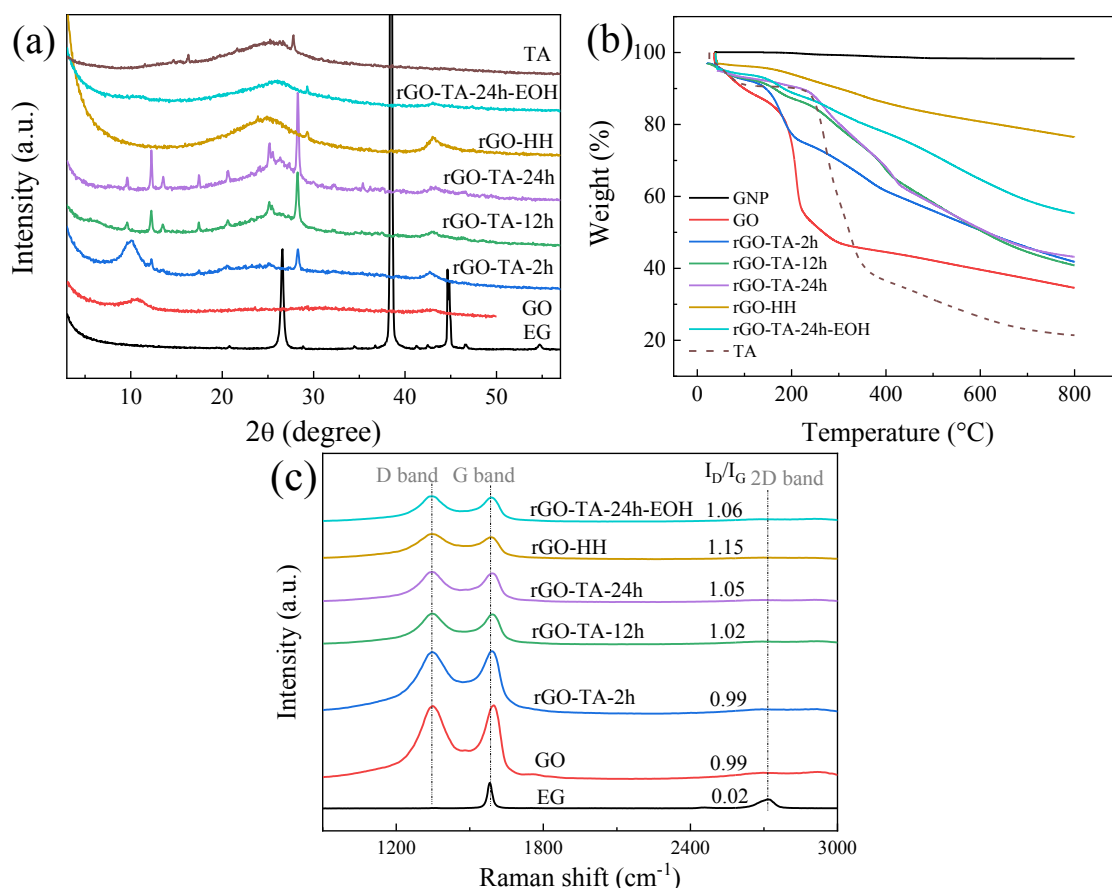


Fig. 5.3.3 (a) XRD patterns, (b) thermogravimetric analysis and (c) Raman spectra of EG, GO, and rGOs.

The thermogravimetric (TG) curves of GNP, GO, rGOs, and TA are shown in Fig. 5.3.3 (b). The TG curve of GO owns a sharp weight loss at around 210°C . This weight

loss is also shown in the TG plots of rGO-TAs, but the intensity decreases steadily with the increase of reduction time. Moreover, the TG curves of rGO-TAs (except for rGO-TA-24h-EOH) present various degrees of weight loss at around 300 °C, consistent to the weight loss temperature of TA. On the other hand, the TG curves of GO, rGO-TA-24h, and rGO-TA-24h-EOH show weight residues of 34.6 %, 43.2 %, and 55.3 %, respectively, at 800 °C. This phenomenon not only indicates the reduction effect of TA, but also demonstrates that TA and some impurities formed during reduction process have been removed by washing with ethanol. The weight residue at 800 °C shown in the TG plot of rGO-HH is 76.5 %, indicating some oxygen-containing functional groups still remain, and the reduction degree of rGO-HH is higher than that of rGO-TA-24h. Raman spectroscopy was used to evaluate the carbonaceous structure. Fig. 5.3.3 (c) illustrates the Raman spectra of EG, GO, and rGOs. The Raman spectra show three characteristic peaks. D band appeared at around 1340 cm^{-1} is related to the sp^3 defects due to the existence of hydroxyl and epoxide groups. G band at around 1587 cm^{-1} is associated with the in-plane vibration of sp^2 carbon atoms. And the 2D band at around 2710 cm^{-1} is a second-order overtone caused by second scattering. [189] The intensity ratio of D band to G band (I_D/I_G) can reflect the extent of structural defects. When the EG was oxidized into GO, the I_D/I_G ratio increased from 0.02 to 0.99 due to the oxidation-induced defects. After GO was reduced into rGO, the I_D/I_G ratio further increased to 1.02, 1.05 and 1.15 for rGO-TA-12h, rGO-TA-24h, and rGO-HH, respectively. After washing away the TA in the rGO-TA-24h by ethanol, the I_D/I_G ratio of rGO-TA-24h-EOH slightly increased to 1.06. Compared with GO, the increase of I_D/I_G ratio of rGOs can be attributed to the decrease of average size of sp^2 domains and the increase of graphene edges. [190, 191] Moreover, the I_D/I_G ratio of rGO-TA was lower than that of rGO-HH, which means using TA caused less structural destruction compared to using HH.

Fig. 5.3.4 illustrates the FTIR/ATR spectra of TA, GO, rGO-TA-24h, rGO-HH, and rGO-TA-24h-EOH. In the FTIR/ATR spectrum of GO, a broad peak at 3250 cm^{-1} is corresponding to the stretching of OH vibration; the peaks at 1730 cm^{-1} , 1184 cm^{-1} , and 1040 cm^{-1} are caused by the C=O, C-OH, and C-O stretching, respectively. [192] After reduced by TA for 24h, the C=O and C-O peaks weakened and the OH adsorption peak in of disappeared in the FTIR/ATR spectrum of rGO-TA-24h. This result demonstrated

the effective reducing effect of TA on GO. Additionally, the increased intensity of C-OH stretching vibration peak at around 1184 cm^{-1} can be explained by the presence of TA in the rGO-TA-24h. Besides, the $\text{-C-C}_{\text{aromatic}}$ stretching vibration peak at 1442 cm^{-1} and distortion vibration of C=C in benzene rings at 750 cm^{-1} also attributed to the existence of TA. [193, 194] In the FTIR/ATR spectrum of rGO-TA-24h-EOH, the C=O, C-OH, and C-O peaks further weakened, and the peaks at 1442 cm^{-1} and 750 cm^{-1} totally or almost disappeared. This phenomenon was because ethanol has been washed away the TA in rGO-TA-24h. When using HH as reducer, all the oxygenous group-related peaks in the spectrum of GO became weaker or even disappeared, indicating strong reduction effect of HH.

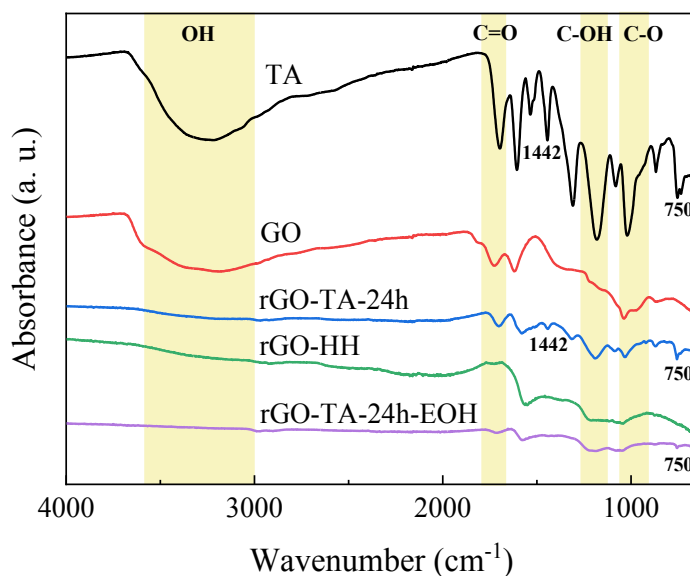


Fig. 5.3.4 FTIR/ATR spectra of TA, GO, rGO-TA-24h, rGO-HH, and rGO-TA-24h-EOH.

5.3.3. Electrochemical properties and morphology of PANI/rGO

Standard cyclic voltammograms of PANI/rGO (1:0.1) composites were recorded in a potential window of -1.0 to 0.6 V versus Hg/Hg₂SO₄ reference electrode, in order to evaluate their electrochemical properties and their potential of being used as supercapacitor electrode. It can be seen in Fig. 5.3.5 that the cyclic voltammograms of most PANI/rGO composites at a potential scan rate of 10 mV s^{-1} present two anodic peaks (A1 and A2) and one cathodic peak. These redox peaks are corresponding to the faradaic transformations between different redox states of PANIs (the fully-reduced

leucoemeraldine, the fully-oxidized pernigraniline, and the middle-state emeraldine). As the scan rate gradually increases to 100 mV s^{-1} , the magnitude of current density increases steadily because of internal resistance. In comparison, the magnitude of cyclic voltammograms of PANI/(rGO-TA-2h) and PANI/(rGO-TA-24h) are the lowest and highest, respectively.

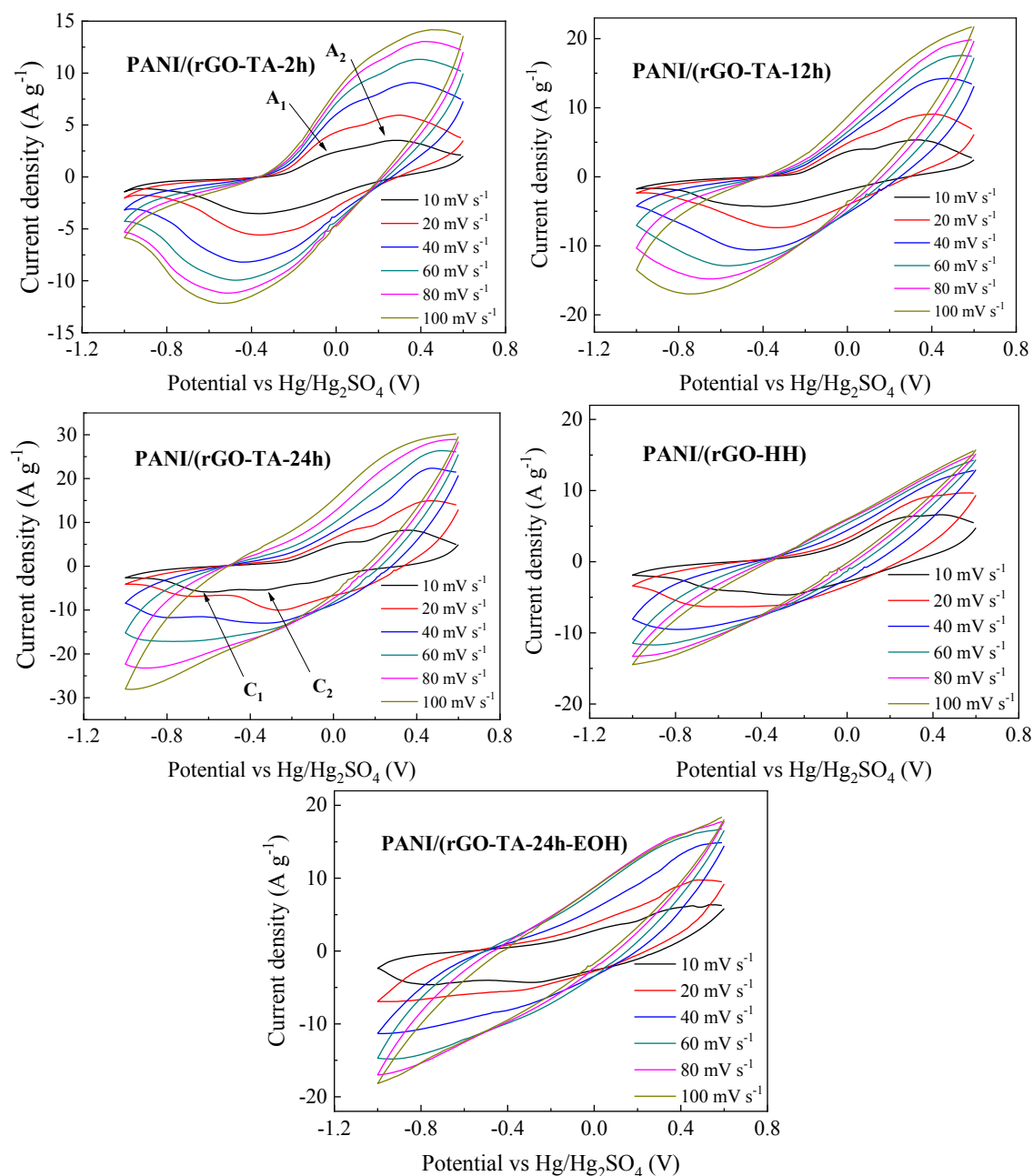


Fig. 5.3.5 Cyclic voltammograms of PANI/(rGO-TA) (1:0.1), PANI/(rGO-HH) (1:0.1), and PANI/(rGO-TA-24h-EOH) (1:0.1) composites at different scan rates.

The CV plots of PANI/rGO (1:0.1) composites at the scan rate of 20 mV s^{-1} are intuitively compared in Fig. 5.3.6 (a). Obviously, the cyclic voltammograms of PANI/(rGO-TA-24h) composite shows the highest magnitude and the most obvious redox peaks. The specific capacitances of the PANI/rGO composites at different scan rates according to the CV results were calculated by the Equation 4.3.1. The plots of as-calculated specific capacitance of the PANI/rGO (1:0.1) composites against the potential scan rate are shown in Fig. 5.3.6 (b). The magnitude of specific capacitance of PANI/(rGO-TA) composites increases with the reduction time of TA. At a scan rate of 10 mV s^{-1} , the specific capacitance of PANI/(rGO-TA-24h-EOH) composite, in which TA has been washed away by ethanol before the synthesis of composite, is higher than those of PANI/(rGO-TA-2h) and PANI/(rGO-TA-12h) composites. However, PANI/(rGO-TA-24h-EOH) composite no longer shows this advantage at high scan rates. Compared to the PANI/(rGO-HH) composite, whose CV plot showed a specific capacitance of 215.1 F g^{-1} at 10 mV s^{-1} but only 11.5 % retention (24.7 F g^{-1}) at 100 mV s^{-1} , the PANI/(rGO-TA-24h) composite owned a higher specific capacitance (268.1 F g^{-1} at 10 mV s^{-1}) and better rate capability with a 31.1 % retention (83.5 F g^{-1}) at 100 mV s^{-1} . This difference indicated that using TA as reducing agent not only gained a higher specific capacitance, but also a relatively better rate capability than using HH.

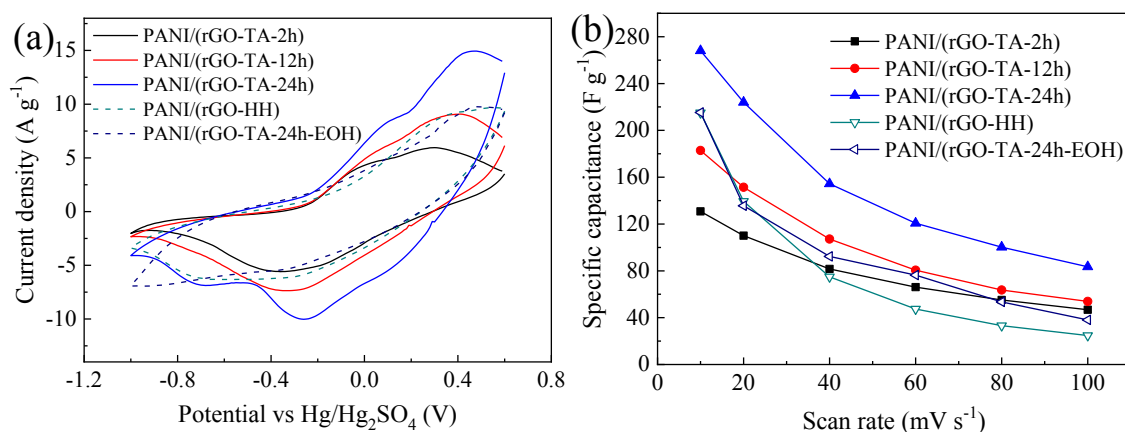


Fig. 5.3.6 (a) CV plots at a scan rate of 20 mV s^{-1} and (b) the specific capacitance at different scan rates of PANI/(rGO-TA) (1:0.1), PANI/(rGO-HH) (1:0.1), and PANI/(rGO-TA-24h-EOH) (1:0.1) composites.

It is commonly known that the electrochemical performance of a material is related to the conductivity and specific surface area. Therefore, the conductivity of the PANI/rGO composites under a pressure of 30 MPa and their specific surface area were investigated, aiming to analysis their electrochemical performance. For the test of specific surface area, even though the testing tube was sealed with a cotton ball, the light fine powder-like samples still tend to fly out. Therefore, the tested values of specific surface area shown in Fig. 5.3.7 are lower than the real surface areas due to the experimental error. As can be seen in the histogram of Fig. 5.3.7, with the reduction time increasing from 2 h to 12 h and then to 24 h, the conductivities of PANI/(rGO-TA) composites gradually increased. While the specific surface area of PANI/(rGO-TA) composites firstly slightly increased and then sharply decreased. Among all the composites, the PANI/(rGO-HH) composite showed the lowest specific surface area, followed by PANI/(rGO-TA-24h-EOH) composite. This result is due to the restacking and bad dispersion of rGO-HH and rGO-TA-24h-EOH. And the worse dispersion of rGO-TA-24h-EOH compared with rGO-TA-24h can also explain the lower conductivity of PANI/(rGO-TA-24h-EOH) composite compared with that of the PANI/(rGO-TA-24h) composite. Interestingly, the conductivity of PANI/(rGO-HH) composite was not affected by the bad dispersion of rGO-HH; it even presented the highest conductivity among the PANI/rGO composites. This phenomenon can be attributed to the higher reduction degree of rGO-HH compared to that of the rGO-TAs. Based on the results shown in Fig. 5.3.7, the combination of a medium magnitude of specific surface area and a relatively high conductivity of PANI/(rGO-TA-24h) could explain its highest specific capacitance illustrated in Fig. 5.3.6 (b).

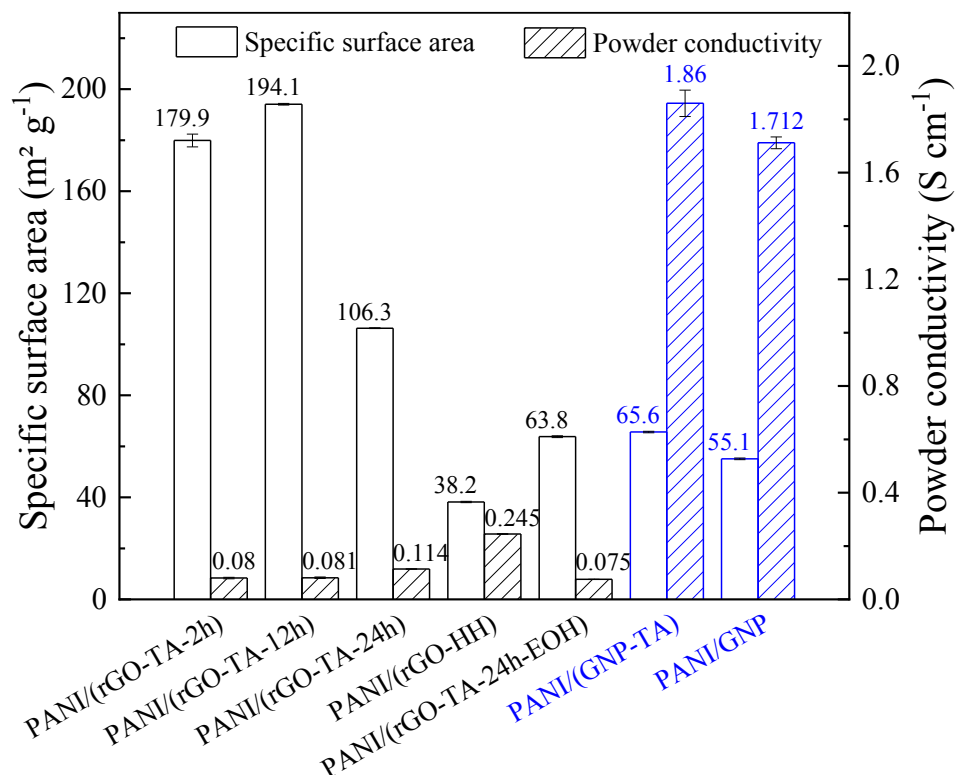


Fig. 5.3.7 Specific surface areas and powder conductivities measured under 30 MPa of PANI/rGO (in black color) and PANI/GNP (in blue color) composites.

The morphologies of the PANI/rGO (1:0.1) composites and pure PANI are illustrated in Fig. 5.3.8. Obviously, the PANI components in PANI/(rGO-TA-12h), PANI/(rGO-TA-24h), PANI/(rGO-HH), and PANI/(rGO-TA-24h-EOH) composites showed microfibrillar networks, which is similar to the morphology of pure PANI. In comparison, the fibrillar PANI in PANI/(rGO-TA-12h) composite owned much higher aspect ratio than the PANI in other composites. This phenomenon might be the reason for the largest specific surface area of PANI/(rGO-TA-12h) composite shown in Fig. 5.3.7. Compared to the PANI in PANI/(rGO-HH) and PANI/(rGO-TA-24h-EOH) composites, the PANI microfibers in the PANI/(rGO-TA-12h) and PANI/(rGO-TA-24h) composites showed more homogenous distributions on the surface of rGO. Otherwise, the PANI components in PANI/(rGO-TA-2h) composite illustrated drop-like morphologies and clustered together. As has been reported in some literatures, the morphology of PANI produced by in-situ polymerization could be influenced by aniline concentration, solution acidity, reaction temperature, mole ratio of oxidant to aniline, and so on. [33, 34] In this study, the pure PANI and all the composites were produced

under the same aniline concentration, temperature, and with same content of oxidant. Therefore, the different morphologies of PANI in the PANI/rGO (1:0.1) composites might be attributed to the different surface functionality of the rGOs and the different acidity, which was caused by the residue conversion products and impurities formed during the reduction of GO.

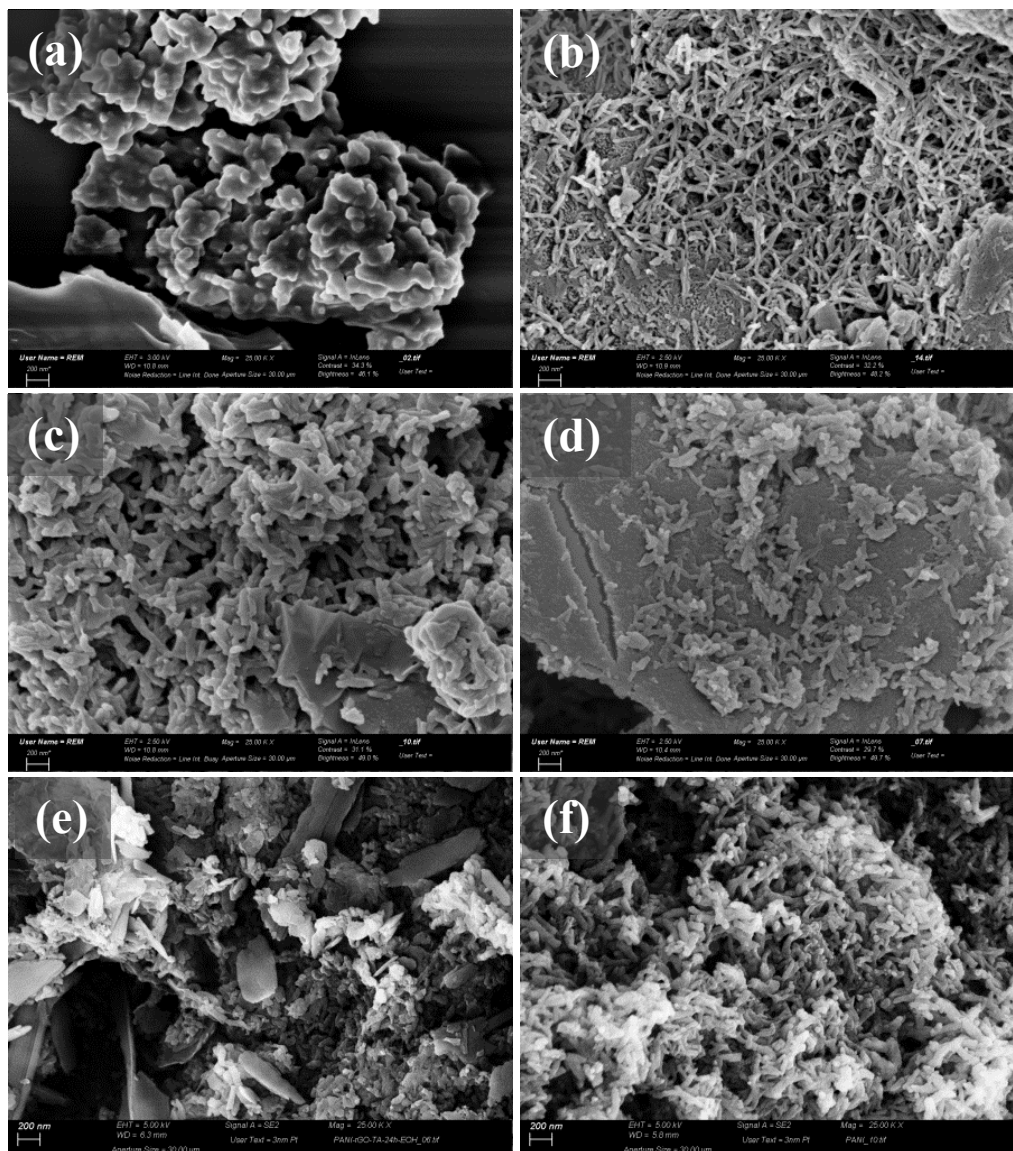


Fig. 5.3.8 SEM images of (a) PANI/(rGO-TA-2h), (b) PANI/(rGO-TA-12h), (c) PANI/(rGO-TA-24h), (d) PANI/(rGO-HH), (e) PANI/(rGO-TA-24h-EOH) composites, and (f) pure PANI. The scale bar in all images is 200 nm.

5.3.4. Electrochemical properties and morphology of PANI/GNP

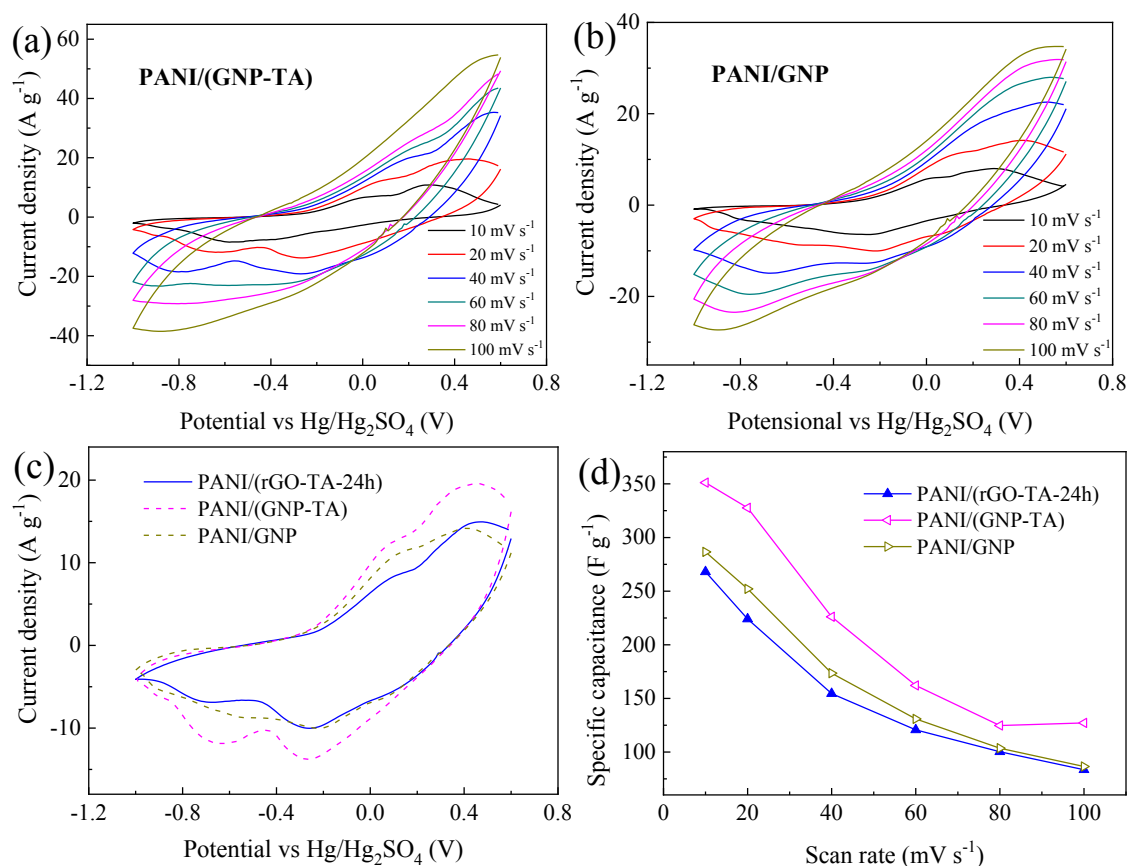


Fig. 5.3.9 (a, b) Cyclic voltammograms of PANI/GNP (1:0.1) composites with and without TA under different scan rates; (c) cyclic voltammograms at a scan rate of 20 mV s⁻¹ and (d) the specific capacitance of PANI/(rGO-TA-24h) (1:0.1), PANI/(GNP-TA) (1:0.1), and PANI/GNP (1:0.1) composites.

The effect of TA on the electrochemical properties of PANI/GNP composites was also investigated in this study. Fig. 5.3.9 (a) and (b) show the cyclic voltammetric behavior of PANI/(GNP-TA) and PANI/GNP composites, respectively. The shape of these CV plots is similar to the CV plots of PANI/rGO composites illustrated in Fig. 5.3.5. However, it is clear that the magnitude of the CV plots of PANI/GNP composites is much higher than that of PANI/rGO composites. This result is further demonstrated in Fig. 5.3.9 (c), where the cyclic voltammograms of PANI/GNP composites at a scan rate of 20 mV s⁻¹ are compared with that of PANI/(rGO-TA-24h) composite. Based on the CV plots, the specific capacitance of PANI/(GNP-TA) and PANI/GNP composites at different scan rate were calculated. As can be seen in Fig. 5.3.9 (d) and Table 5.3.1, both of PANI/(GNP-TA) and PANI/GNP composites exhibited higher specific

capacitances than PANI/(rGO-TA-24h) composite. Moreover, the specific capacitances of PANI/(GNP-TA) at all the tested scan rates were higher than those of PANI/GNP composite, which demonstrated the addition of TA during the sonication-exfoliation process of GNP was beneficial to the electrochemical property of PANI/GNP composites.

Table 5.3.1 Capacitive performances of PANI/(rGO-TA) and PANI/GNP composites.

Sample	Specific capacitance at 20 mV s ⁻¹ (F g ⁻¹)	Retention of specific capacitance at 100 mV s ⁻¹ (%)
PANI/(rGO-TA-2h)	130.7	35.8
PANI/(rGO-TA-12h)	182.9	29.5
PANI/(rGO-TA-24h)	268.1	31.1
PANI/(rGO-HH)	215.1	11.5
PANI/(rGO-TA-24h-EOH)	215.3	17.7
PANI/(GNP-TA)	351.2	36.2
PANI/GNP	286.6	30.2

The data of specific surface area and conductivity of the different PANI/GNP (1:0.1) composites are shown in Fig. 5.3.7 in blue color, and compared with those of PANI/rGO (1:0.1) composites (in black color). The specific surface areas of PANI/GNP composites were smaller than those of the PANI/(rGO-TA) composites, but the conductivities of PANI/GNP composites were significantly higher than those of all the PANI/rGO composites. This largely enhanced conductivity can be attributed to the higher conductivity of GNP compared to the rGO, since the carbonaceous structure of rGO has been defected to some degree during the oxidation and reduction process. On the other hand, the presence of TA in the GNP enlarged the specific capacitance and increased the conductivity of the PANI/GNP composite. Here, the morphologies of PANI/(GNP-TA) and PANI/GNP composites were also investigated. As shown in Fig. 5.3.10 (a) and (c), PANI was relatively homogeneously distributed on the surface of TA-modified GNP in the PANI/(GNP-TA) composite, but clustered together in the PANI/GNP composite. It can be inferred that TA could interact with aniline due to its plenty of catechol and pyrogallol units, and then promote a homogeneous distribution of

PANI on the surface of GNP-TA. Furthermore, it is obvious in the enlarged SEM images (Fig. 5.3.10 (b) and (d)) that the PANI in both of PANI/(GNP-TA) and PANI/GNP composites show fibrillar networks, indicating the morphology of PANI component has not been influenced by the TA. Therefore, the drop-like morphological PANI in some PANI/rGO composites illustrated in Fig. 5.3.8 was more likely caused by some impurities in the rGO solution rather than by the existence of TA.

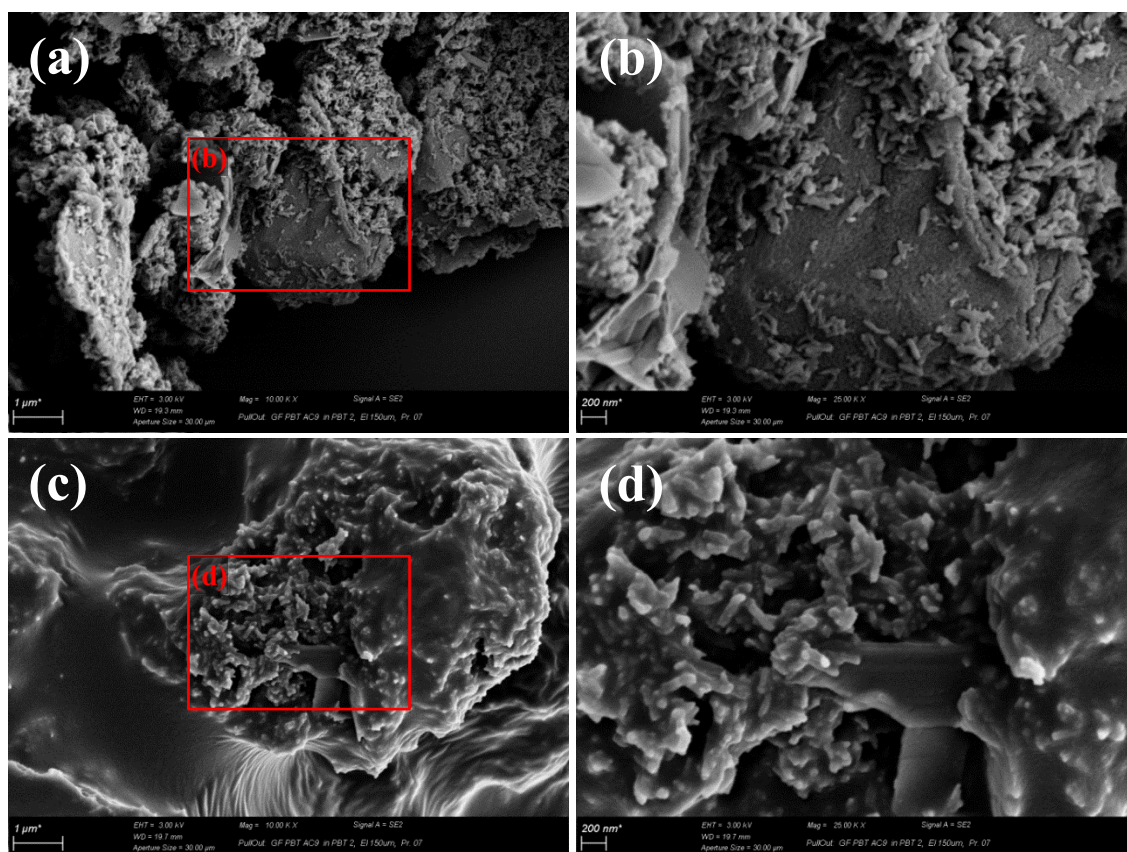


Fig. 5.3.10 SEM images of (a, b) PANI/(GNP-TA) and (c, d) PANI/GNP composites. The scale bars are 1 μm in (a) and (c), and 200 nm in (b) and (d).

5.3.5. Solid-state symmetric supercapacitor device

The results in the sections 5.3.3 and 5.3.4 indicate that TA showed positive effect on the electrochemical properties of PANI/rGO and PANI/GNP composites. In order to further test the electrochemical performance of the PANI/(rGO-TA) and PANI/(GNP-TA) in practical use, solid-state supercapacitor devices were assembled by using PANI/(rGO-TA) or PANI/(GNP-TA) as the electrodes. The photograph and

structural schematic of the device are shown in Fig. 4.3.2. The supercapacitor has a symmetric structure, namely, the anode and cathode electrode were the same material with similar weight and shape. Electrodes were prepared by the same method as for the electrodes for the three-electrode electrochemical tests, but with a rectangle shape. 1 M H₂SO₄-PVA gel was used as electrolyte, and the current collectors were rectangle stainless steel mesh with a length of 4 cm and a width of around 1 cm. Besides PANI/(rGO-TA) and PANI/(GNP-TA), PANI/(rGO-HH) and PANI/GNP were also assembled into this kind of supercapacitor device. Fig. 5.3.11 illustrates the CV plots of the supercapacitor devices using the four different composites as electrode. The weight and area of each electrode in the symmetric supercapacitor devices were controlled to be similar. Weights (*m*) of PANI/(rGO-TA), PANI/(GNP-TA), PANI/(rGO-HH) and PANI/GNP electrode were 9 mg, 9 mg, 10 mg, and 9 mg, respectively; and the areas (*S*) were 1.235 cm², 1.523 cm², 1.43 cm², and 1.3 cm², respectively. Noting different Y-axis scale ranges between the former two plots and the latter two plots in Fig. 5.3.11, it is obvious that PANI/(GNP-TA) and (PANI/GNP) supercapacitors exhibit larger CV integral area than the PANI/rGO supercapacitors. Moreover, the CV integral area of the PANI/(rGO-TA-24h) supercapacitor is larger than that of the PANI/(rGO-HH) supercapacitor, and the CV integral area of PANI/(GNP-TA) supercapacitor is larger than that of PANI/GNP supercapacitors.

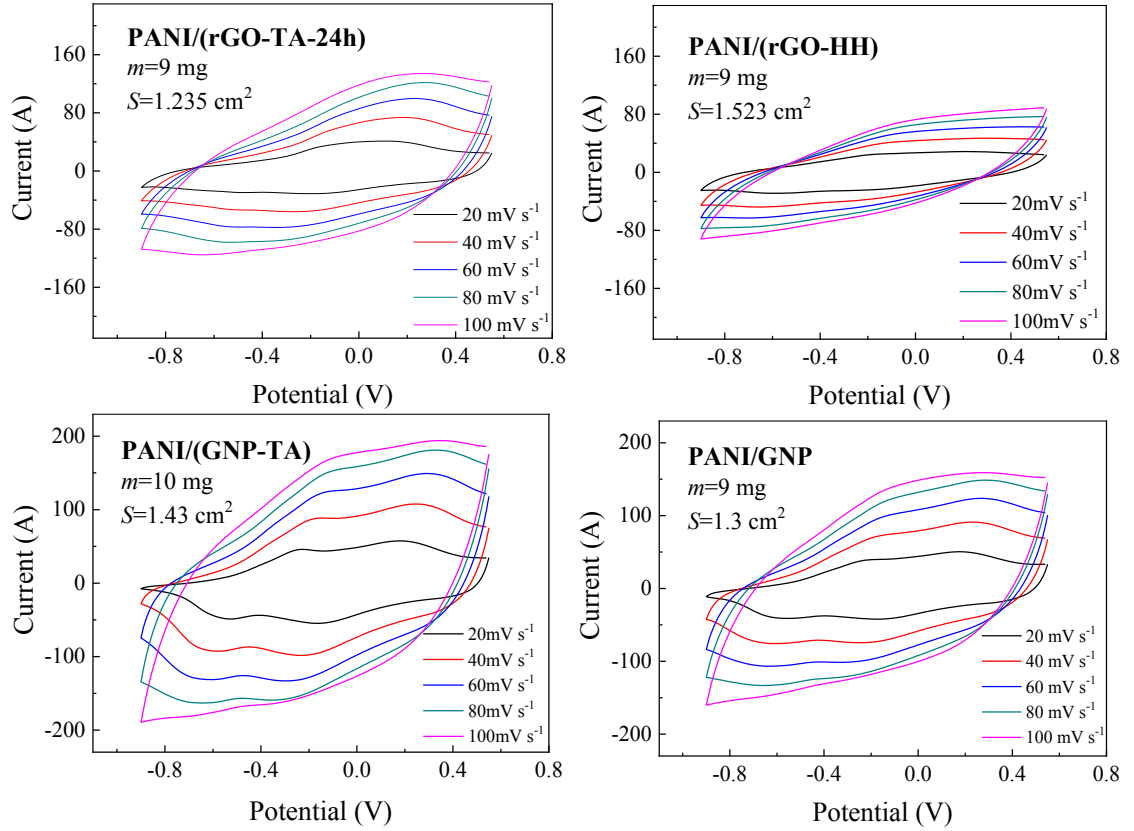


Fig. 5.3.11 Cyclic voltammograms of the symmetric supercapacitor devices.

The mass (C_M , $F g^{-1}$) and area specific capacitance (C_S , $F cm^{-2}$) of the supercapacitor devices were calculated based on the CV results shown in Fig. 5.3.11 by the following equations:

$$C_M = \frac{\int I(V) \cdot dV}{M \cdot \Delta V \cdot \nu} \quad (5.1.3)$$

$$C_S = \frac{\int I(V) \cdot dV}{S \cdot \Delta V \cdot \nu} \quad (5.1.4)$$

where the M represent the total mass weight of anode and cathode, equal to two fold of m . And the S is the area of the electrode. The calculated C_M and C_S at different scan rates are shown in Fig. 5.3.12 (a) and (b). Obviously, both of the cell mass specific capacitance and the area specific capacitance follow the same sequence, i.e. PANI/(GNP-TA) > (PANI/GNP) > PANI/(rGO-TA-24h) > PANI/(rGO-HH). The PANI/(rGO-TA-24h) symmetric supercapacitor showed a specific mass capacitance of

121.3 F g⁻¹ and a specific area capacitance of 1.8 F cm⁻². The PANI/(GNP-TA) symmetric supercapacitor exhibited specific capacitances of 158.1 F g⁻¹ and 2.2 F cm⁻². Moreover, the cycle stabilities of the symmetric supercapacitor devices at a scan rate of 100 mV s⁻¹ were also investigated. Fig. 5.3.12 (c) compares the 1st CV plots and the 190th CV plots of the four supercapacitor devices. The CV plots of all the four supercapacitors show a decrease in the integral area after 190 times CV cycles. The plot of specific mass capacitance to the CV cycle time is shown in Fig. 5.3.12 (d). Obviously, the PANI/(GNP-TA) supercapacitor owned the highest specific capacitance at all the CV cycles. The magnitudes of specific capacitance of PANI/GNP supercapacitors were higher than those of the PANI/rGO supercapacitor. And the addition of TA had positive effect on the capacitance of both PANI/GNP and PANI/rGO supercapacitors. Fig. 5.3.12 (d) also reflects the cycle stability of the four supercapacitor devices. At the beginning, PANI/(GNP-TA) and PANI/(rGO-HH) supercapacitors showed the highest and the lowest decrease rate of specific capacitance, respectively. After ~50 CV cycles the decrease rates of the four supercapacitors became similar. The retentions of specific capacitance after 190 times of CV cycles of PANI/(rGO-TA-24h), PANI/(rGO-HH), PANI/(GNP-TA), and PANI/GNP supercapacitors were 76.6%, 88.2%, 72.9%, and 76.9%, respectively. Additionally, the initial specific capacitances shown in Fig. 5.3.12 (d) (scan rate was 100 mV s⁻¹) were a bit smaller than the specific capacitances at the scan rate of 100 mV s⁻¹ shown in Fig. 5.3.12 (a). It is because the cycle stability tests (Fig. 5.3.12 (d)) were done after the CV tests at different scan rates (Fig. 5.3.12 (a)) and the galvanostatic charge/discharge tests (Fig. 5.3.13), and each test was accompanied with some extent of decline in the capacitive ability of the electrode material.

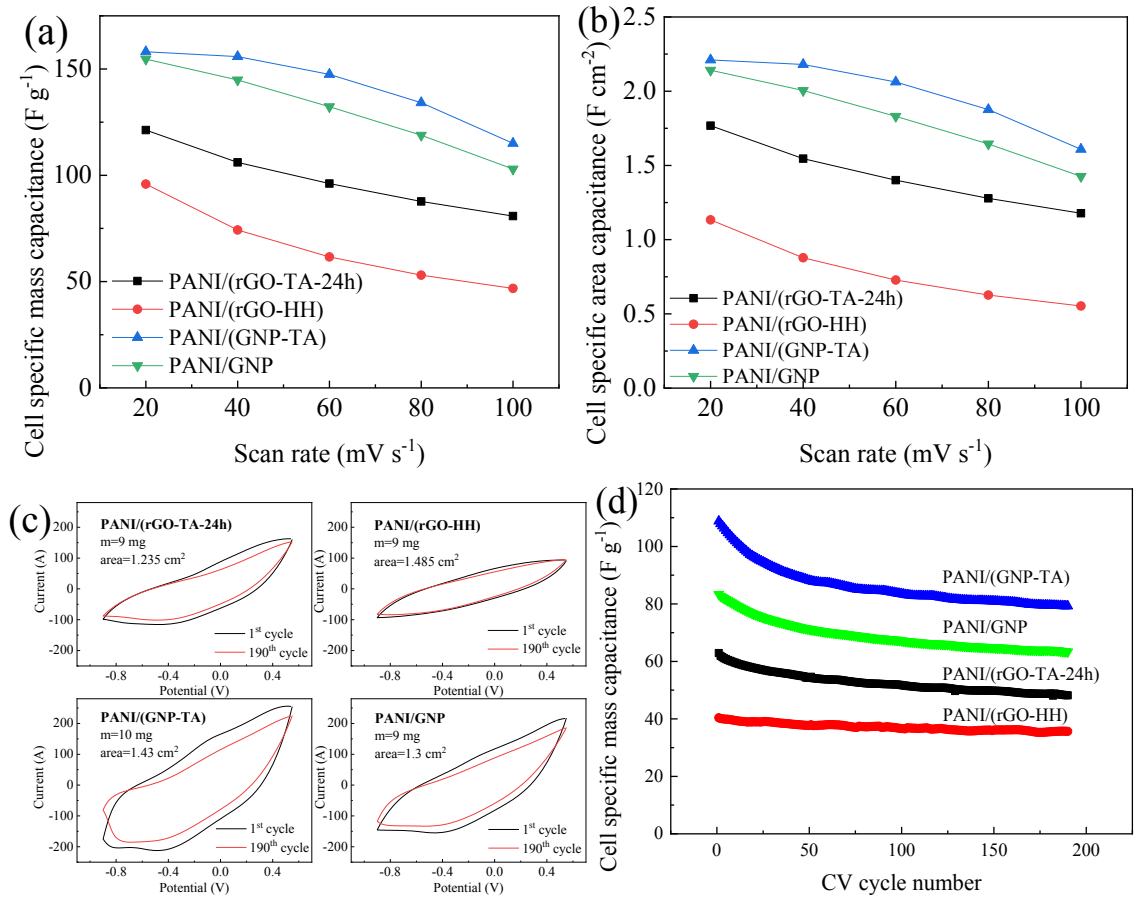


Fig. 5.3.12 Specific mass (a) and area capacitance (b) at different scan rates and (c) the CV plots at a scan rate of 100 mV s⁻¹ of the 1st and 190th cycles and (d) the specific mass capacitance during CV cycle of the symmetric supercapacitor devices.

The galvanostatic charging-discharging (GCD) behavior of the supercapacitor devices using PANI/(rGO-TA-24h), PANI/(rGO-HH), PANI/(GNP-TA), or PANI/GNP as electrodes are shown in Fig. 5.3.13 (a). The current density was set at 0.5 A g⁻¹, namely, 9 mA for the test of PANI/(rGO-TA-24h), PANI/(rGO-HH), and PANI/GNP supercapacitors, and 10 mA for the GCD test of PANI/(GNP-TA) supercapacitor. The energy density (E , Wh kg⁻¹) and power density (P , W kg⁻¹) of the supercapacitor devices were calculated using the equations:

$$C_{cell} = \frac{I \cdot t}{V_{max}} \quad (5.1.5)$$

$$E = \frac{1}{2} \cdot \frac{10^3 \cdot C_{cell} \cdot V_{max}^2}{3.6 \cdot M} \quad (5.1.6)$$

$$P = \frac{3600 \cdot E}{t} \quad (5.1.7)$$

The C_{cell} is the capacitance of the supercapacitor calculated according to the GCD plots. V_{max} is the maximum voltage for discharging after the IR drop. The plot of the calculated energy density to the power density (Ragone plot) of the supercapacitor devices are illustrated in Fig. 5.3.13 (b). The supercapacitors with PANI/GNP composites as electrodes showed higher energy and power densities than those using PANI/rGO composite as electrodes. Moreover, using TA for the preparation of composites enhanced the energy and power density of the supercapacitors, especially for the PANI/rGO composites. The PANI/(GNP-TA) symmetric supercapacitor device owned an high energy density of 2.3 Wh kg^{-1} and a power density of 119 W kg^{-1} ; and PANI/(rGO-TA-24h) supercapacitor presented an good energy density and a power density of 1.7 Wh kg^{-1} and 115.3 W kg^{-1} , respectively.

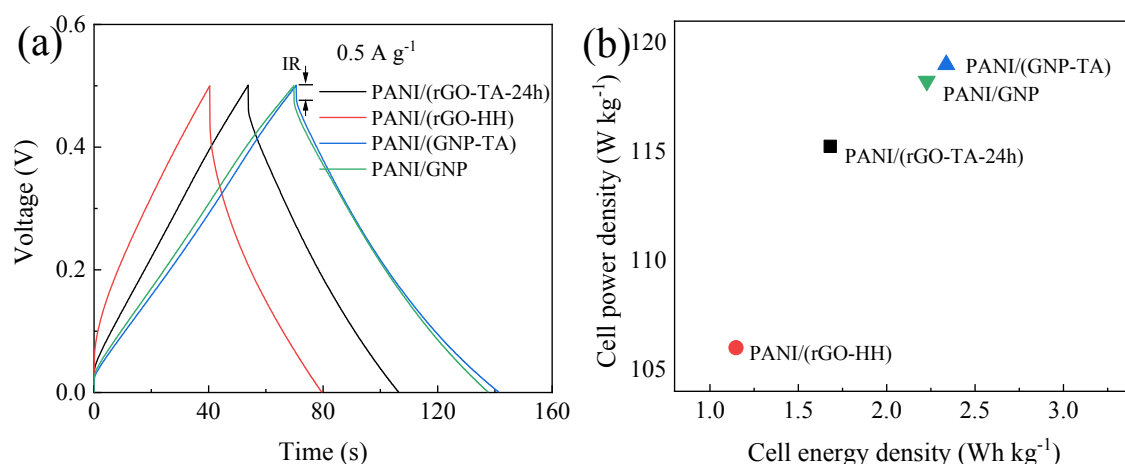


Fig. 5.3.13 (a) Galvanostatic charge/discharge diagram and (b) the Ragone plot of the symmetric supercapacitor devices.

5.3.6. Summary

Environment-friendly tannic acid (TA) was used to develop the electrochemical properties of PANI/rGO (1:0.1) and PANI/GNP (1:0.1) composites. With a reduction time of 24h, GO was effectively reduced by tannic acid into rGO-TA-24h. Compared with rGO-HH, which was reduced by hydrazine hydrate, rGO-TA-24h showed a lower reduction degree but higher dispersion stability. Besides, TA also played a role of

dispersion stabilizer for rGO-TA and GNP, and its interaction with aniline is beneficial to a homogeneous distribution of PANI on the surface of rGO-TA. As a result, PANI/(rGO-TA-24h) (1:0.1) composite showed a little bit lower conductivity but much larger specific surface area and higher specific capacitance than the PANI/(rGO-HH) (1:0.1) composite. Furthermore, PANI/(GNP-TA) (1:0.1) composite presents higher conductivity, larger specific surface area, and higher specific capacitance than PANI/GNP (1:0.1) composite. TA-modified PANI/rGO and PANI/GNP composites exhibited a specific capacitance of 268.1 F g⁻¹ and 351.2 F g⁻¹ at 10 mV s⁻¹, respectively. The assembled two-electrode solid-state supercapacitor device using TA-modified PANI/rGO or PANI/GNP composites as electrodes showed high energy densities of 1.7 Wh kg⁻¹ and 2.3 Wh kg⁻¹, respectively.

6. Conclusions

Composites of polyaniline (PANI) and carbonaceous material are promising to be used as supercapacitor electrode. Among the carbonaceous materials, graphene has attracted lots of attention due to its high specific surface area and excellent conductivity. However, the difficulty and high cost of producing monolayer graphene are hard to meet the requirement of large-scale manufacturing. Therefore, cost-effective reduced graphite oxide (rGO) and graphite nanoplates (GNP) were used as the carbonaceous fillers in this study. With the aim to optimize the overall electrochemical performance of PANI/rGO and PANI/GNP composites, the interactions between certain synthesis parameters and the electrochemical behavior of the obtained PANI/graphite composites were investigated; and then two green chemicals (polydopamine, PDA and tannic acid, TA) were used to pre-modify the rGO or GNP.

Firstly, the effects of synthesis parameters on the actual composition ratio, electrochemical properties, conductivities, and morphologies of PANI/GNP (1:0.1 wt./wt.) and (1:1 wt./wt.) composites have been systematically studies. The PANI/GNP composites were produced by in-situ oxidative polymerization in an acidic aqueous solution with or without dopant (4-dodecylbenzenesulfonic acid, DBSA). SEM image and the corresponding EDX analysis indicated that PANI/GNP composite has been successfully produced. Structural characterizations, namely UV-vis, FTIR/ATR, and N 1s XPS, indicated that PANI and GNP components interacted with each other by π -conjugation. And the presence of GNP changed the electron distribution of PANI, thus the quinoid/benzenoid ratio in PANI molecular decreased. The morphologies and yield of PANI in the composites varied with the type of oxidant. When FeCl_3 was used as oxidant, the PANI component showed a drop-like morphology; when ammonium persulfate (APS) was used as oxidant, PANI formed a micro-fibrillar network in the composite. According to the actual composition ratio calculated from thermogravimetric behavior of pure PANI, GNP, and the PANI/GNP composites, aniline only partly transferred into PANI when using FeCl_3 as oxidant but almost fully polymerized into PANI when using APS as oxidant. Moreover, the conductivity of PANI/GNP-APS was higher than that of the corresponding PANI/GNP composites produced with FeCl_3 as

oxidant. These differences resulted in a higher specific capacitance of PANI/GNP-APS compared to the PANI/GNP using FeCl_3 . Additionally, too much content of oxidant might cause over-oxidation of PANI, therefore sacrificed the electrochemical property of PANI/GNP composites.

The effect of DBSA on the electrochemical properties of PANI/GNP composites varied with the component ratio. The interaction between the PANI backbone and the alkyl chains of DBSA was beneficial to the conductivity, which was important for the overall electrochemical property, but impeded the capacitance of PANI component. For the PANI-dominated PANI/GNP (1:0.1) composites, whose conductivity was rather low, adding DBSA increased the conductivities and thus largely increased the overall specific capacitance of the composite. For the PANI/GNP composite with a weight ratio of 1 to 1, the conductivity was dominated by GNP. Therefore, adding DBSA could not obviously increase the conductivity and showed negative effect on the electrochemical property of composites. Additionally, the different conductivities and specific capacitances of PANI/GNP (1:0.1) and (1:1) composites indicated that faradaic PANI contributed more to the overall capacitance of composites than the capacitive GNP. But GNP was important for the rate capability of composites, since it can enhance the stability of PANI component and increase electron transfer.

In the second and third parts of research, two chemicals were used to enhance the electrochemical properties of PANI/graphite composite. Based on the results of the first research part, the synthesis parameters used in the second and third parts were set as follows: a PANI to graphite weight ratio of 1:0.1, use of APS as oxidant, and without the addition of DBSA. In the second part, the polymerization of dopamine was used to reduce and functionalize graphite oxide (GO). The catechol functional groups of PDA were expected to prevent the restacking of the obtained GO-PDA and enhanced the interaction between GO-PDA and PANI. Two synthesis routes were used in this section. The composites named as PANI/(GO-PDA) were obtained by polymerization of aniline in the presence of GO-PDA; the composites named as PANI/GO-PDA were produced by polymerizing dopamine in the presence of PANI/GO composite. In the third part, TA has been used to modify the rGO and GNP before the synthesis of composites. The PANI/(rGO-HH) composite, in which hydrazine hydrate (HH) was used as reducing

agent, and PANI/GNP composite were also synthesized as comparison for the PANI/(rGO-TA) and PANI/GNP composites, respectively. Fig. 6.1 summarised the differences among the four different PANI/rGO composites investigated in the second and third research parts, i.e. PANI/GO-PDA, PANI/(GO-PDA), PANI/(rGO-TA) and PANI/(rGO-HH), with the aspects of the synthesis procedures and the structure of final products.

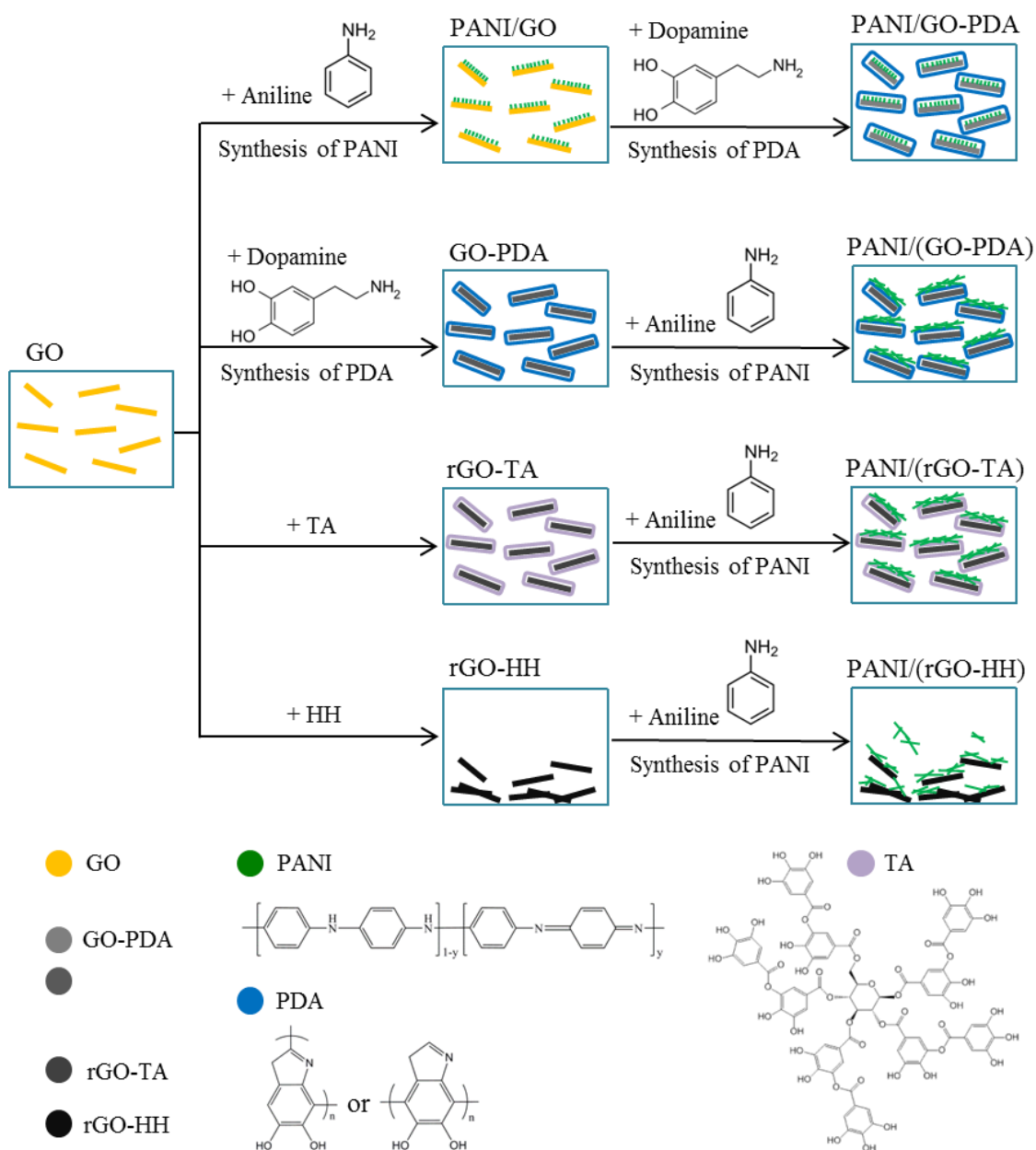


Fig. 6.1 Schematic illustration of the synthesis of PANI/GO-PDA, PANI/(GO-PDA), PANI/(rGO-TA) and PANI/(rGO-HH). The different shades of black represent the different reduction degrees of the GO-PDAs, rGO-TA, and rGO-HH.

The XRD, TGA, FTIR/ATR, and UV-vis results showed that GO has been only partly reduced during the polymerization of dopamine, and the reduction degree of the GO-PDA product did not increase with the increase of dopamine content. In Fig. 6.1, the GO-PDAs were marked with lighter black compared to rGO-TA and rGO-HH, representing the lower reduction degree of GO-PDAs. Moreover, different synthesis routes resulted in composites with different morphologies and properties. Similar to the PANI/GO composite, the PANIs (green color in Fig. 6.1) in the PANI/GO-PDA composites were short nanowire arrays grown vertically on the surface of GO. On the contrary, the morphologies of PANIs in the PANI/(GO-PDA) composites were mainly fibrillar networks. The main drawback of using dopamine in the preparation of composites for supercapacitor purpose was the non-conductivity of PDA. The conductivity of the obtained GO-PDA was much lower than the conductivity of GNP and decreased with the increase of dopamine content. All the PANI/GO-PDA composites were non-conductive, since the non-conductive PDA (blue color in Fig. 6.1) has coated on the composites. Therefore, even though the PANI showed a homogenous distribution in the PANI/GO-PDA composites, and most of PANI/GO-PDA composites have higher specific surface areas than the corresponding PANI/(GO-PDA) composites, the PANI/GO-PDA composites still showed worse electrochemical properties. On the other hand, the conductivities of PANI/(GO-PDA) composites were low, due to the low reduction degree of GO-PDA and the non-conductivity of PDA. As a result, the rate capabilities of PANI/(GO-PDA) composites were similar to that of pure PANI.

For TA, the structural characterizations (XRD, Raman spectra, and FTIR/ATR) demonstrated that it effectively reduced GO into rGO-TA. The carbonaceous structure of the obtained rGO-TA had fewer defects than that of the rGO-HH. TA also acts as dispersion stabilizer for rGO and GNP. Therefore, rGO-TA (shown in Fig. 6.1) and GNP-TA could keep a homogeneous dispersion in the aqueous acid solution during the in-situ polymerization of aniline. Additionally, the phenolic hydroxyl in TA could interact with the amine groups of PANI, thus promoted a homogeneous distribution of PANI on the surface of rGO or GNP. Among the PANI/rGO composites shown in Fig. 6.1, the PANI/(rGO-TA-24h) composites showed the highest specific capacitance (268.1 F g^{-1} at 20 mV s^{-1}). The PANI/(GNP-TA) composite also showed higher specific

capacitance than the PANI/GNP composites. In comparison, PANI/(GNP-TA) composite exhibited better electrochemical performance than the PANI/(rGO-TA-24h) composite in the three-electrode testing system as well as in the two-electrode supercapacitor device. This result can be attributed to the higher conductivity and a carbonaceous structure with fewer defects in the case of GNP-TA compared to the rGO-TA. Based on this part of research, the environmental friendly TA is an attractive and effective material to be used for the purpose of developing the electrochemical properties of PANI/rGO and PANI/GNP composites.

In summary, combination of PANI and the cost-effective graphite can obtain composites with good electrochemical performance. For the synthesis method of in-situ polymerization of aniline in presence of GNP, the type and content of oxidant can affect the electrochemical properties of PANI/GNP composites. Besides, the addition of excess dopant can influence the electrochemical properties of a PANI-dominated system. The two eco-friendly reduction ways, namely polymerization of dopamine and adding TA, both produced graphite with good dispersion stability and enhanced interaction with PANI. But the reduction effect of dopamine polymerization was weak, and the non-conductivity of PDA has negative effect on the electrochemical performance of the composites. Using the environmental friendly TA is an effective and facile way to produce cost-effective PANI/graphite composites for supercapacitor purpose. Comparing the two types of graphite, rGO showed lower conductivity and more defects in the carbonaceous structure compared to GNP. In my study, the PANI/(GNP-TA) (1:0.1) composites, which was prepared by using APS as oxidant and without dopant, exhibited the highest capacitive ability. In a three-electrode testing system, the PANI/(GNP-TA) composite showed a high specific capacitance of 351.2 F g^{-1} at 10 mV s^{-1} . The corresponding two-electrode solid-state supercapacitor device exhibited a promising energy density of 2.3 Wh kg^{-1} at 0.5 A g^{-1} , which was comparable to the commercially available supercapacitors (around 5 Wh kg^{-1}) [195]. But for application the rate capability of the composite needs to be enhanced, in order to maintain the good capacitive performance at high current density.

7. Outlook

This work focused on the study of the effect of some synthesis parameters, polydopamine (PDA) and tannic acid (TA) on the electrochemical properties of in-situ polymerized PANI/GNP and PANI/rGO composites. For the further development of the overall electrochemical performance of PANI/graphite composites, some other research works are worth to be done in the future.

First of all, the electrochemical stability should be improved. In this study, PANI/GNP (1:0.1) composites showed higher specific capacitance than the corresponding PANI/GNP (1:1) composites, but with the sacrifice of rate capability. If the effect of GNP, i.e. transferring electrons and supplying structural support for PANI, could be enhanced without changing its content, then the obtained PANI/GNP (1:0.1) composites would achieve the goal of balancing excellent specific capacitance and high rate capability. For this purpose, one should prevent the restacking of GNP and enhance the interaction between PANI and GNP. rGO owns better dispersion stability than GNP, but it suffers from the drawbacks of worse conductivity and more carbonaceous structural defects. Therefore, in the future work, GNP should be used as the carbonaceous component. Surface pre-modification of GNP is necessary, since GNP tend to restack and interact only weakly with PANI. The preparation of GNP by electrochemical exfoliation method reported by Yang *et al.* [196] may be a suitable method. This method is environmental friendly, fast, possible for mass production and can simultaneously functionalize the GNP product.

Secondly, the PANI/GNP and PANI/rGO composites studied in this thesis were all synthesized by the in-situ oxidative polymerization of aniline in the presence of the graphitic structures. In the future study, one may produce binder-free PANI/GNP or PANI/rGO composites by electrochemically depositing PANI on 3D structural graphitic basement. It has been reported that electrochemically synthesized PANI presents better purity than the in-situ chemical polymerized PANI. On the other hand, the graphitic basement can promise a high conductivity of the composite; therefore, a separate current collector would be non-necessary. The elimination of binder and current collector can decrease the internal resistance and enhance the electrochemical

performance of the composites. The growth direction of PANI should be controlled. The morphologies of PANI/GO and PANI/GO-PDA composites reported in the second section of this research demonstrated the possibility of producing PANI nanotubes vertically to the surface of GO or partially reduced GO. The aim of future work is to realize the control of this vertical growth of PANI on GNP.

Finally, in order to increase the electrochemical performance of PANI/GNP composites, efforts are also worth to be devoted on controlling the orientation of GNP on the current collector. Up to now, most of the reported supercapacitor electrode films are very thin, since the vertical transfer ability of ions in thick electrode cannot meet the requirement of practical use. In other words, parts of the electrode materials were not active since the ions cannot reach them. Few articles have demonstrated that vertical alignment of two-dimensional carbonaceous materials can realize thickness-independent electrochemical performance in thick electrode films. [197] Even though it is still a challenge to produce such kind of vertical oriented GNP, it is a worth to be investigated. A smooth transfer of ions can not only realize the production of thick composite electrodes, but also make most of the PANI component active to store and release energy, which can increase the overall energy density and power density.

Bibliography

1. Wang, Y., Song, Y., and Xia, Y., *Electrochemical capacitors: mechanism, materials, systems, characterization and applications*. Chemical Society Reviews, 2016. **45**(21): p. 5925-5950.
2. Guan, C., et al., *Iron oxide-decorated carbon for supercapacitor anodes with ultrahigh energy density and outstanding cycling stability*. ACS nano, 2015. **9**(5): p. 5198-5207.
3. Moosavifard, S.E., et al., *Designing 3D highly ordered nanoporous CuO electrodes for high-performance asymmetric supercapacitors*. ACS applied materials & interfaces, 2015. **7**(8): p. 4851-4860.
4. You, Y., et al., *Galvanic displacement assembly of ultrathin Co₃O₄ nanosheet arrays on nickel foam for a high-performance supercapacitor*. Nanotechnology, 2017. **28**(10): p. 105604.
5. Guo, X.L., et al., *Monodispersed plum candy-like MnO₂ nanosheets-decorated NiO nanostructures for supercapacitors*. Ceramics International, 2016. **42**(6): p. 7787-7792.
6. Zhang, Z., et al., *One-pot synthesis of hierarchically nanostructured Ni₃S₂ dendrites as active materials for supercapacitors*. Electrochimica Acta, 2014. **149**: p. 316-323.
7. Simon, P. and Gogotsi, Y., *Materials for electrochemical capacitors*, in *Nanoscience And Technology: A Collection of Reviews from Nature Journals*, 2010. p. 320-329.
8. Wang, G., Zhang, L., and Zhang, J., *A review of electrode materials for electrochemical supercapacitors*. Chemical Society Reviews, 2012. **41**(2): p. 797-828.
9. González, A., et al., *Review on supercapacitors: technologies and materials*. Renewable and Sustainable Energy Reviews, 2016. **58**: p. 1189-1206.
10. Zuo, X., et al., *One-step electrochemical preparation of sulfonated graphene/polypyrrole composite and its application to supercapacitor*. Journal of Alloys and Compounds, 2016. **688**: p. 140-148.
11. Du, W., et al., *A surfactant-free water-processable all-carbon composite and its application to supercapacitor*. Electrochimica Acta, 2014. **146**: p. 353-358.
12. Basnayaka, P.A. and Ram, M.K., *A Review of Supercapacitor Energy Storage Using Nanohybrid Conducting Polymers and Carbon Electrode Materials*, in *Conducting Polymer Hybrids*, 2017, Cham. p. 165-192.
13. Simon, P., Brousse, T., and Favier, F., *Electrochemical Double-Layer Capacitors (EDLC)*, in *Supercapacitors Based on Carbon or Pseudocapacitive Materials*, 2017, Hoboken, NJ, USA. p. 1-25.
14. Asif, M., et al., *Improved performance of a MnO₂@ PANI nanocomposite synthesized on 3D graphene as a binder free electrode for supercapacitors*. RSC Advances, 2016. **6**(52): p. 46100-46107.
15. Abdelhamid, M.E., O'Mullane, A.P., and Snook, G.A., *Storing energy in plastics: a review on conducting polymers & their role in electrochemical energy storage*. Rsc Advances, 2015. **5**(15): p. 11611-11626.

16. Grover, S., *et al.*, *Polyaniline all solid-state pseudocapacitor: role of morphological variations in performance evolution*. *Electrochimica Acta*, 2016. **196**: p. 131-139.
17. Eftekhari, A., Li, L., and Yang, Y., *Polyaniline supercapacitors*. *Journal of Power Sources*, 2017. **347**: p. 86-107.
18. Li, Z., *et al.*, *Doping effects of cerium ion on structure and electrochemical properties of polyaniline*. *Polymer International*, 2018. **67**(1): p. 121-126.
19. Arslan, A. and Hür, E., *Supercapacitor applications of polyaniline and poly (N-methylaniline) coated pencil graphite electrode*. *International Journal of Electrochemical Science*, 2012. **7**: p. 12558-12572.
20. Zhang, L., *et al.*, *Skeleton networks of graphene wrapped double-layered polypyrrole/polyaniline nanotubes for supercapacitor applications*. *Journal of Materials Science*, 2018. **53**(1): p. 787-798.
21. Hong, X., *et al.*, *Three-dimensional reduced graphene oxide/polyaniline nanocomposite film prepared by diffusion driven layer-by-layer assembly for high-performance supercapacitors*. *Journal of Power Sources*, 2017. **343**: p. 60-66.
22. Zhang, Y., *et al.*, *Progress of electrochemical capacitor electrode materials: A review*. *International journal of hydrogen energy*, 2009. **34**(11): p. 4889-4899.
23. Zhao, T., *et al.*, *In situ synthesis of interlinked three-dimensional graphene foam/polyaniline nanorod supercapacitor*. *Electrochimica Acta*, 2017. **230**: p. 342-349.
24. Li, Y., *et al.*, *Oriented arrays of polyaniline nanorods grown on graphite nanosheets for an electrochemical supercapacitor*. *Langmuir*, 2012. **29**(1): p. 493-500.
25. Meng, Y., *et al.*, *Hierarchical porous graphene/polyaniline composite film with superior rate performance for flexible supercapacitors*. *Advanced Materials*, 2013. **25**(48): p. 6985-6990.
26. Bhoyate, S., *et al.*, *Recent Development on Nanocomposites of Graphene for Supercapacitor Applications*. *Curr. Graphene Sci*, 2017. **1**: p. 26-43.
27. Memon, M.A., *et al.*, *Conjunction of Conducting Polymer Nanostructures with Macroporous Structured Graphene Thin Films for High-Performance Flexible Supercapacitors*. *ACS applied materials & interfaces*, 2016. **8**(18): p. 11711-11719.
28. Tung, N.T., *et al.*, *The effects of dopant on morphology formation in polyaniline graphite nanoplatelet composite*. *Synthetic Metals*, 2011. **161**(1-2): p. 177-182.
29. Li, B. and Zhong, W.-H., *Review on polymer/graphite nanoplatelet nanocomposites*. *Journal of materials science*, 2011. **46**(17): p. 5595-5614.
30. Abdolhosseinzadeh, S., Asgharzadeh, H., and Kim, H.S., *Fast and fully-scalable synthesis of reduced graphene oxide*. *Scientific reports*, 2015. **5**: p. 10160.
31. Winter, M. and Brodd, R.J., *What are batteries, fuel cells, and supercapacitors?* *Chemical Reviews*, 2004. **104**(10): p. 4245-4270.
32. Eftekhari, A. and Fang, B., *Electrochemical hydrogen storage: opportunities for fuel storage, batteries, fuel cells, and supercapacitors*. *International Journal of Hydrogen Energy*, 2017. **42**(40): p. 25143-25165.
33. Faraji, S. and Ani, F.N., *The development supercapacitor from activated carbon by electroless plating—A review*. *Renewable and Sustainable Energy Reviews*, 2015. **42**: p. 823-834.

34. Burke, A., *Ultracapacitors: why, how, and where is the technology*. Journal of power sources, 2000. **91**(1): p. 37-50.
35. Whittingham, M.S., *Materials challenges facing electrical energy storage*. MRS Bulletin, 2008. **33**(4): p. 411-419.
36. Xiong, G., *et al.*, *A review of graphene-based electrochemical microsupercapacitors*. Electroanalysis, 2014. **26**(1): p. 30-51.
37. Jayalakshmi, M. and Balasubramanian, K., *Simple capacitors to supercapacitors-an overview*. International Journal of Electrochemical Science, 2008. **3**(11): p. 1196-1217.
38. Halper, M.S. and Ellenbogen, J.C., *Supercapacitors: A brief overview*. MITRE Nanosystems Group, 2006.
39. Béguin, F., *et al.*, *Carbons and electrolytes for advanced supercapacitors*. Advanced materials, 2014. **26**(14): p. 2219-2251.
40. Xia, H., *et al.*, *A symmetric RuO₂/RuO₂ supercapacitor operating at 1.6 V by using a neutral aqueous electrolyte*. Electrochemical and Solid-State Letters, 2012. **15**(4): p. A60-A63.
41. Chen, W., Rakhi, R., and Alshareef, H.N., *Facile synthesis of polyaniline nanotubes using reactive oxide templates for high energy density pseudocapacitors*. Journal of Materials Chemistry A, 2013. **1**(10): p. 3315-3324.
42. Brandt, A., *et al.*, *Ionic liquids in supercapacitors*. MRS bulletin, 2013. **38**(7): p. 554-559.
43. Choudhury, N., Sampath, S., and Shukla, A., *Hydrogel-polymer electrolytes for electrochemical capacitors: an overview*. Energy & Environmental Science, 2009. **2**(1): p. 55-67.
44. Khosrozadeh, A., Xing, M., and Wang, Q., *A high-capacitance solid-state supercapacitor based on free-standing film of polyaniline and carbon particles*. Applied Energy, 2015. **153**: p. 87-93.
45. Tsay, K.C., Zhang, L., and Zhang, J., *Effects of electrode layer composition/thickness and electrolyte concentration on both specific capacitance and energy density of supercapacitor*. Electrochimica Acta, 2012. **60**: p. 428-436.
46. Gualous, H., *et al.*, *Experimental study of supercapacitor serial resistance and capacitance variations with temperature*. Journal of power sources, 2003. **123**(1): p. 86-93.
47. Portet, C., *et al.*, *Modification of Al current collector surface by sol-gel deposit for carbon-carbon supercapacitor applications*. Electrochimica Acta, 2004. **49**(6): p. 905-912.
48. Chmiola, J., *et al.*, *Effect of pore size and surface area of carbide derived carbons on specific capacitance*. Journal of Power Sources, 2006. **158**(1): p. 765-772.
49. He, Y., *et al.*, *Freestanding three-dimensional graphene/MnO₂ composite networks as ultralight and flexible supercapacitor electrodes*. ACS nano, 2012. **7**(1): p. 174-182.
50. He, S. and Chen, W., *3D graphene nanomaterials for binder-free supercapacitors: scientific design for enhanced performance*. Nanoscale, 2015. **7**(16): p. 6957-6990.

51. Jiang, S., *et al.*, *High-performance binder-free supercapacitor electrode by direct growth of cobalt-manganese composite oxide nanostructures on nickel foam*. *Nanoscale research letters*, 2014. **9**(1): p. 492.
52. Xiao, X., *et al.*, *Freestanding mesoporous VN/CNT hybrid electrodes for flexible all-solid-state supercapacitors*. *Advanced Materials*, 2013. **25**(36): p. 5091-5097.
53. Chun, S.-E., *et al.*, *Design of aqueous redox-enhanced electrochemical capacitors with high specific energies and slow self-discharge*. *Nature communications*, 2015. **6**.
54. Wang, G.P., Zhang, L., and Zhang, J.J., *A review of electrode materials for electrochemical supercapacitors*. *Chemical Society Reviews*, 2012. **41**(2): p. 797-828.
55. Conway, B., Birss, V., and Wojtowicz, J., *The role and utilization of pseudocapacitance for energy storage by supercapacitors*. *Journal of Power Sources*, 1997. **66**(1): p. 1-14.
56. Zhi, M., *et al.*, *Nanostructured carbon-metal oxide composite electrodes for supercapacitors: a review*. *Nanoscale*, 2013. **5**(1): p. 72-88.
57. Zhang, L.L. and Zhao, X., *Carbon-based materials as supercapacitor electrodes*. *Chemical Society Reviews*, 2009. **38**(9): p. 2520-2531.
58. Borenstein, A., *et al.*, *Carbon-based composite materials for supercapacitor electrodes: a review*. *Journal of Materials Chemistry A*, 2017. **5**(25): p. 12653-12672.
59. Brousse, T., *et al.*, *Long-term cycling behavior of asymmetric activated carbon/MnO₂ aqueous electrochemical supercapacitor*. *Journal of Power Sources*, 2007. **173**(1): p. 633-641.
60. Salinas-Torres, D., *et al.*, *Asymmetric hybrid capacitors based on activated carbon and activated carbon fibre-PANI electrodes*. *Electrochimica Acta*, 2013. **89**: p. 326-333.
61. Amatucci, G.G., *et al.*, *An asymmetric hybrid nonaqueous energy storage cell*. *Journal of the Electrochemical Society*, 2001. **148**(8): p. A930-A939.
62. Zhang, F., *et al.*, *A high-performance supercapacitor-battery hybrid energy storage device based on graphene-enhanced electrode materials with ultrahigh energy density*. *Energy & Environmental Science*, 2013. **6**(5): p. 1623-1632.
63. Lu, P., *et al.*, *Supercapacitor and nanoscale research towards electrochemical energy storage*. *International Journal of Smart and Nano Materials*, 2013. **4**(1): p. 2-26.
64. Bhadra, S., *et al.*, *Progress in preparation, processing and applications of polyaniline*. *Progress in polymer science*, 2009. **34**(8): p. 783-810.
65. Snook, G.A., Kao, P., and Best, A.S., *Conducting-polymer-based supercapacitor devices and electrodes*. *Journal of Power Sources*, 2011. **196**(1): p. 1-12.
66. Baker, C.O., *et al.*, *Polyaniline nanofibers: broadening applications for conducting polymers*. *Chemical Society Reviews*, 2017. **46**(5): p. 1510-1525.
67. Santiago, E., Pereira, E., and Bulhoes, L., *Characterization of the redox processes in polyaniline using capacitance-potential curves*. *Synthetic metals*, 1998. **98**(2): p. 87-93.
68. Boeva, Z.A. and Sergeev, V.G., *Polyaniline: Synthesis, properties, and application*. *Polymer Science Series C*, 2014. **56**(1): p. 144-153.

69. Wu, X., *et al.*, *Hydrogen bonding of graphene/polyaniline composites film for solid electrochromic devices*. Synthetic Metals, 2016. **212**: p. 1-11.
70. Gospodinova, N. and Terlemezyan, L., *Conducting polymers prepared by oxidative polymerization: polyaniline*. Progress in Polymer Science, 1998. **23**(8): p. 1443-1484.
71. Li, C., Bai, H., and Shi, G., *Conducting polymer nanomaterials: electrosynthesis and applications*. Chemical Society Reviews, 2009. **38**(8): p. 2397-2409.
72. Gao, H., *et al.*, *Aqueous/ionic liquid interfacial polymerization for preparing polyaniline nanoparticles*. Polymer, 2004. **45**(9): p. 3017-3019.
73. Liu, H., *et al.*, *Structure, conductivity, and thermopower of crystalline polyaniline synthesized by the ultrasonic irradiation polymerization method*. Macromolecules, 2002. **35**(25): p. 9414-9419.
74. Wei, Z. and Wan, M., *Hollow microspheres of polyaniline synthesized with an aniline emulsion template*. Advanced Materials, 2002. **14**(18): p. 1314-1317.
75. Colak, N. and Sökmen, B., *Doping of chemically synthesized polyaniline*. Designed monomers and polymers, 2000. **3**(2): p. 181-189.
76. Carswell, A.D., O'Rea, E.A., and Grady, B.P., *Adsorbed surfactants as templates for the synthesis of morphologically controlled polyaniline and polypyrrole nanostructures on flat surfaces: from spheres to wires to flat films*. Journal of the American Chemical Society, 2003. **125**(48): p. 14793-14800.
77. Wang, X., *et al.*, *Synthesis of PANI nanostructures with various morphologies from fibers to micromats to disks doped with salicylic acid*. Synthetic Metals, 2010. **160**(17-18): p. 2008-2014.
78. Stejskal, J., Sapurina, I., and Trchová, M., *Polyaniline nanostructures and the role of aniline oligomers in their formation*. Progress in Polymer Science, 2010. **35**(12): p. 1420-1481.
79. Xing, S., *et al.*, *Morphology and conductivity of polyaniline nanofibers prepared by 'seeding' polymerization*. Polymer, 2006. **47**(7): p. 2305-2313.
80. Stejskal, J., *et al.*, *Oxidation of aniline: polyaniline granules, nanotubes, and oligoaniline microspheres*. Macromolecules, 2008. **41**(10): p. 3530-3536.
81. Chen, W.C., Wen, T.C., and Teng, H., *Polyaniline-deposited porous carbon electrode for supercapacitor*. Electrochimica Acta, 2003. **48**(6): p. 641-649.
82. Li, S., *et al.*, *Flexible supercapacitors based on bacterial cellulose paper electrodes*. Advanced Energy Materials, 2014. **4**(10): p. 1301655.
83. Zhou, S., Wu, T., and Kan, J., *Effect of methanol on morphology of polyaniline*. European Polymer Journal, 2007. **43**(2): p. 395-402.
84. Kan, J., Lv, R., and Zhang, S., *Effect of ethanol on properties of electrochemically synthesized polyaniline*. Synthetic Metals, 2004. **145**(1): p. 37-42.
85. Chiou, N.R. and Epstein, A.J., *Polyaniline nanofibers prepared by dilute polymerization*. Advanced Materials, 2005. **17**(13): p. 1679-1683.
86. Chen, J., *et al.*, *Novel interfacial polymerization for radially oriented polyaniline nanofibers*. Materials letters, 2007. **61**(6): p. 1419-1423.
87. Huang, J. and Kaner, R.B., *Nanofiber formation in the chemical polymerization of aniline: a mechanistic study*. Angewandte Chemie, 2004. **116**(43): p. 5941-5945.
88. Yang, C.H., *et al.*, *Molecular assembled self-doped polyaniline copolymer ultra-thin films*. Polymer, 2007. **48**(11): p. 3237-3247.

89. Kim, J.Y., Lee, J.H., and Kwon, S.J., *The manufacture and properties of polyaniline nano-films prepared through vapor-phase polymerization*. Synthetic metals, 2007. **157**(8-9): p. 336-342.
90. Kumar, S., *et al.*, *Synthesis of polyaniline nanostructures via reverse microemulsion technique*. Soft Materials, 2009. **7**(3): p. 150-163.
91. Jang, J., Ha, J., and Kim, S., *Fabrication of polyaniline nanoparticles using microemulsion polymerization*. Macromolecular research, 2007. **15**(2): p. 154-159.
92. Rao, P.S., Sathyanarayana, D., and Palaniappan, S., *Polymerization of aniline in an organic peroxide system by the inverted emulsion process*. Macromolecules, 2002. **35**(13): p. 4988-4996.
93. Zhou, Q., *et al.*, *The relationship of conductivity to the morphology and crystallinity of polyaniline controlled by water content via reverse microemulsion*. Colloid and Polymer Science, 2007. **285**(4): p. 405-411.
94. Lu, X., *et al.*, *Fabrication of polyaniline nanostructures under ultrasonic irradiation: from nanotubes to nanofibers*. Macromolecular Chemistry and Physics, 2006. **207**(22): p. 2142-2152.
95. Mi, H., *et al.*, *Polyaniline nanofibers as the electrode material for supercapacitors*. Materials Chemistry and Physics, 2008. **112**(1): p. 127-131.
96. Li, G.R., *et al.*, *Electrochemical synthesis of polyaniline nanobelts with predominant electrochemical performances*. Macromolecules, 2010. **43**(5): p. 2178-2183.
97. Bian, C. and Yu, A., *De-doped polyaniline nanofibres with micropores for high-rate aqueous electrochemical capacitor*. Synthetic Metals, 2010. **160**(13-14): p. 1579-1583.
98. Kuang, H., *et al.*, *Influence of the reaction temperature on polyaniline morphology and evaluation of their performance as supercapacitor electrode*. Journal of Applied Polymer Science, 2013. **130**(5): p. 3753-3758.
99. Wang, Z.L., *et al.*, *Polyaniline nanotube arrays as high-performance flexible electrodes for electrochemical energy storage devices*. Journal of Materials Chemistry, 2012. **22**(6): p. 2401-2404.
100. Yang, W., *et al.*, *Synthesis of hollow polyaniline nano-capsules and their supercapacitor application*. Journal of Power Sources, 2014. **272**: p. 915-921.
101. Liu, J., *et al.*, *Porous polyaniline exhibits highly enhanced electrochemical capacitance performance*. Electrochimica Acta, 2010. **55**(20): p. 5819-5822.
102. Deshmukh, P., *et al.*, *Polyaniline–RuO₂ composite for high performance supercapacitors: chemical synthesis and properties*. RSC Advances, 2015. **5**(36): p. 28687-28695.
103. Li, X., *et al.*, *Preparation and electrochemical properties of RuO₂/polyaniline electrodes for supercapacitors*. Synthetic Metals, 2012. **162**(11-12): p. 953-957.
104. Hu, Z.A., *et al.*, *Polyaniline/SnO₂ nanocomposite for supercapacitor applications*. Materials Chemistry and Physics, 2009. **114**(2-3): p. 990-995.
105. Jiang, H., Ma, J., and Li, C., *Polyaniline–MnO₂ coaxial nanofiber with hierarchical structure for high-performance supercapacitors*. Journal of Materials Chemistry, 2012. **22**(33): p. 16939-16942.
106. Patil, D.S., *et al.*, *Facile preparation and enhanced capacitance of the Ag-PEDOT: PSS/polyaniline nanofiber network for supercapacitors*. Electrochimica Acta, 2016. **213**: p. 680-690.

107. Mi, H., *et al.*, *Preparation and enhanced capacitance of core-shell polypyrrole/polyaniline composite electrode for supercapacitors*. Journal of Power Sources, 2008. **176**(1): p. 403-409.
108. Lei, W., *et al.*, *One-step triple-phase interfacial synthesis of polyaniline-coated polypyrrole composite and its application as electrode materials for supercapacitors*. Journal of Power Sources, 2014. **266**: p. 347-352.
109. Xia, X., *et al.*, *Nanostructured ternary composites of graphene/Fe₂O₃/polyaniline for high-performance supercapacitors*. Journal of Materials Chemistry, 2012. **22**(33): p. 16844-16850.
110. Li, S., *et al.*, *Polyaniline-Coupled Multifunctional 2D Metal Oxide/Hydroxide Graphene Nanohybrids*. Angewandte Chemie International Edition, 2013. **52**(46): p. 12105-12109.
111. Han, G., *et al.*, *MnO₂ nanorods intercalating graphene oxide/polyaniline ternary composites for robust high-performance supercapacitors*. Scientific reports, 2014. **4**: p. 4824.
112. Sivakkumar, S. and Saraswathi, R., *Performance evaluation of poly (N-methylaniline) and polyisothianaphthene in charge-storage devices*. Journal of power sources, 2004. **137**(2): p. 322-328.
113. Choudhary, N., *et al.*, *Asymmetric supercapacitor electrodes and devices*. Advanced Materials, 2017. **29**(21): p. 1605336.
114. Mak, W.F., *et al.*, *High-energy density asymmetric supercapacitor based on electrospun vanadium pentoxide and polyaniline nanofibers in aqueous electrolyte*. Journal of the Electrochemical Society, 2012. **159**(9): p. A1481-A1488.
115. Heydari, H. and Gholivand, M.B., *An all-solid-state asymmetric device based on a polyaniline hydrogel for a high energy flexible supercapacitor*. New Journal of Chemistry, 2017. **41**(1): p. 237-244.
116. Bavio, M.A., *et al.*, *Flexible symmetric and asymmetric supercapacitors based in nanocomposites of carbon cloth/polyaniline-carbon nanotubes*. Energy, 2017. **130**: p. 22-28.
117. Lim, Y.S., *et al.*, *Polypyrrole/graphene composite films synthesized via potentiostatic deposition*. Journal of Applied Polymer Science, 2013. **128**(1): p. 224-229.
118. Du, J. and Cheng, H.M., *The fabrication, properties, and uses of graphene/polymer composites*. Macromolecular Chemistry and Physics, 2012. **213**(10-11): p. 1060-1077.
119. Mao, L., *et al.*, *Surfactant-stabilized graphene/polyaniline nanofiber composites for high performance supercapacitor electrode*. Journal of Materials Chemistry, 2012. **22**(1): p. 80-85.
120. Chee, W., *et al.*, *Flexible graphene-based supercapacitors: a review*. The Journal of Physical Chemistry C, 2016. **120**(8): p. 4153-4172.
121. Cheng, Q., *et al.*, *Graphene and carbon nanotube composite electrodes for supercapacitors with ultra-high energy density*. Physical Chemistry Chemical Physics, 2011. **13**(39): p. 17615-17624.
122. Yan, X., *et al.*, *Fabrication of free-standing, electrochemically active, and biocompatible graphene oxide- polyaniline and graphene- polyaniline hybrid papers*. ACS applied materials & interfaces, 2010. **2**(9): p. 2521-2529.

123. Wu, Q., *et al.*, *Supercapacitors based on flexible graphene/polyaniline nanofiber composite films*. ACS nano, 2010. **4**(4): p. 1963-1970.
124. Gao, Z., *et al.*, *Electrochemical synthesis of layer-by-layer reduced graphene oxide sheets/polyaniline nanofibers composite and its electrochemical performance*. Electrochimica Acta, 2013. **91**: p. 185-194.
125. Ge, J., Cheng, G., and Chen, L., *Transparent and flexible electrodes and supercapacitors using polyaniline/single-walled carbon nanotube composite thin films*. Nanoscale, 2011. **3**(8): p. 3084-3088.
126. Dong, X., *et al.*, *Supercapacitor electrode based on three-dimensional graphene-polyaniline hybrid*. Materials Chemistry and Physics, 2012. **134**(2-3): p. 576-580.
127. Yu, M., *et al.*, *Polyaniline nanocone arrays synthesized on three-dimensional graphene network by electrodeposition for supercapacitor electrodes*. Carbon, 2015. **87**: p. 98-105.
128. Cheng, Y., *et al.*, *Flexible and cross-linked N-doped carbon nanofiber network for high performance freestanding supercapacitor electrode*. Nano Energy, 2015. **15**: p. 66-74.
129. Liu, Y., *et al.*, *Polyaniline-graphene composites with a three-dimensional array-based nanostructure for high-performance supercapacitors*. Carbon, 2015. **83**: p. 79-89.
130. Yu, P., *et al.*, *A Novel Sustainable Flour Derived Hierarchical Nitrogen-Doped Porous Carbon/Polyaniline Electrode for Advanced Asymmetric Supercapacitors*. Advanced Energy Materials, 2016. **6**(20): p. 1601111.
131. Wu, J., *et al.*, *A self-assembly route to porous polyaniline/reduced graphene oxide composite materials with molecular-level uniformity for high-performance supercapacitors*. Energy & Environmental Science, 2018. **11**(5): p. 1280-1286.
132. Fan, W., *et al.*, *Graphene-wrapped polyaniline hollow spheres as novel hybrid electrode materials for supercapacitor applications*. ACS applied materials & interfaces, 2013. **5**(8): p. 3382-3391.
133. Zang, X., *et al.*, *Graphene/polyaniline woven fabric composite films as flexible supercapacitor electrodes*. Nanoscale, 2015. **7**(16): p. 7318-7322.
134. Miao, F., *et al.*, *Electrospun carbon nanofibers/carbon nanotubes/polyaniline ternary composites with enhanced electrochemical performance for flexible solid-State supercapacitors*. ACS Sustainable Chemistry & Engineering, 2016. **4**(3): p. 1689-1696.
135. Zeng, S., *et al.*, *Electrochemical fabrication of carbon nanotube/polyaniline hydrogel film for all-solid-state flexible supercapacitor with high areal capacitance*. Journal of Materials Chemistry A, 2015. **3**(47): p. 23864-23870.
136. Yu, P., *et al.*, *Graphene-wrapped polyaniline nanowire arrays on nitrogen-doped carbon fabric as novel flexible hybrid electrode materials for high-performance supercapacitor*. Langmuir, 2014. **30**(18): p. 5306-5313.
137. Ge, D., *et al.*, *Foldable supercapacitors from triple networks of macroporous cellulose fibers, single-walled carbon nanotubes and polyaniline nanoribbons*. Nano Energy, 2015. **11**: p. 568-578.
138. Liu, W., *et al.*, *A wire-shaped flexible asymmetric supercapacitor based on carbon fiber coated with a metal oxide and a polymer*. Journal of Materials Chemistry A, 2015. **3**(25): p. 13461-13467.

139. Xue, M., *et al.*, *Structure-Based Enhanced Capacitance: In Situ Growth of Highly Ordered Polyaniline Nanorods on Reduced Graphene Oxide Patterns*. *Advanced Functional Materials*, 2012. **22**(6): p. 1284-1290.
140. Marcano, D.C., *et al.*, *Improved synthesis of graphene oxide*. *ACS nano*, 2010. **4**(8): p. 4806-4814.
141. Krause, B., *et al.*, *Ultralow percolation threshold in polyamide 6.6/MWCNT composites*. *Composites Science and Technology*, 2015. **114**: p. 119-125.
142. Tayel, M.B., *et al.*, *Sprayed polyaniline layer onto chemically reduced graphene oxide as electrode for high performance supercapacitor*. *Synthetic Metals*, 2016. **217**: p. 237-243.
143. Mao, L., *et al.*, *Surfactant-stabilized graphene/polyaniline nanofiber composites for high performance supercapacitor electrode*. *Journal of Materials Chemistry*, 2012. **22**(1): p. 80-85.
144. Liao, K., *et al.*, *Rod-like polyaniline supported on three-dimensional boron and nitrogen-co-doped graphene frameworks for high-performance supercapacitors*. *Journal of Nanoparticle Research*, 2017. **19**(12): p. 397.
145. Zhang, Y., *et al.*, *Synthesis of novel graphene oxide/pristine graphene/polyaniline ternary composites and application to supercapacitor*. *Chemical Engineering Journal*, 2016. **288**: p. 689-700.
146. Li, Y.Z., *et al.*, *Oriented arrays of polyaniline nanorods grown on graphite nanosheets for an electrochemical supercapacitor*. *Langmuir*, 2012. **29**(1): p. 493-500.
147. Zhang, K., *et al.*, *Graphene/polyaniline nanofiber composites as supercapacitor electrodes*. *Chemistry of Materials*, 2010. **22**(4): p. 1392-1401.
148. Ma, L., *et al.*, *Effects of FeCl₃/ammonium persulfate composite oxidant and magnetic field on film growth rate of polyaniline doped with dodecylbenzenesulfonic acid*. *Journal of Polymer Research*, 2011. **18**(4): p. 595-599.
149. Deng, J.X., *et al.*, *Effect of the oxidant/monomer ratio and the washing post-treatment on electrochemical properties of conductive polymers*. *Industrial & Engineering Chemistry Research*, 2014. **53**(35): p. 13680-13689.
150. Li, B. and Zhong, W.H., *Review on polymer/graphite nanoplatelet nanocomposites*. *Journal of Materials Science*, 2011. **46**(17): p. 5595-5614.
151. Zhao, X., Grätz, O., and Pionteck, J., *Effect of dopant and oxidant on the electrochemical properties of polyaniline/graphite nanoplate composites*. *Polymer International*, 2018. **67**(10): p. 1429-1437.
152. Jo, S., *et al.*, *Simple noncovalent hybridization of polyaniline with graphene and its application for pseudocapacitor*. *Synthetic Metals*, 2015. **209**: p. 60-67.
153. Jiang, X., *et al.*, *An easy one-step electrosynthesis of graphene/polyaniline composites and electrochemical capacitor*. *Carbon*, 2014. **67**: p. 662-672.
154. Cong, H.P., *et al.*, *Flexible graphene–polyaniline composite paper for high-performance supercapacitor*. *Energy & Environmental Science*, 2013. **6**(4): p. 1185-1191.
155. Wang, X., *et al.*, *Crosslinked polyaniline nanorods with improved electrochemical performance as electrode material for supercapacitors*. *Journal of Materials Chemistry A*, 2014. **2**(31): p. 12323-12329.
156. Yan, J., *et al.*, *Preparation of a graphene nanosheet/polyaniline composite with high specific capacitance*. *Carbon*, 2010. **48**(2): p. 487-493.

157. Pruneanu, S., *et al.*, *Characterization of polyaniline by cyclic voltammetry and UV-Vis absorption spectroscopy*. Journal of materials science, 1999. **34**(11): p. 2733-2739.
158. Poussin, D., Morgan, H., and Foot, P.J.S., *Thermal doping of polyaniline by sulfonic acids*. Polymer international, 2003. **52**(3): p. 433-438.
159. Noskov, Y., *et al.*, *Acid-dopant effects in the formation and properties of polycarbonate-polyaniline composites*. Synthetic Metals, 2016. **217**: p. 266-275.
160. Bian, C.Q. and Yu, A.S., *De-doped polyaniline nanofibres with micropores for high-rate aqueous electrochemical capacitor*. Synthetic Metals, 2010. **160**(13): p. 1579-1583.
161. Misoon, O. and Seok, K., *Effect of dodecyl benzene sulfonic acid on the preparation of polyaniline/activated carbon composites by in situ emulsion polymerization*. Electrochimica Acta, 2012. **59**: p. 196-201.
162. Basavaraja, C., *et al.*, *Studies on properties of polyaniline-dodecylbenzene sulfonic acid composite films synthesized using different oxidants*. Macromolecular research, 2009. **17**(8): p. 609-615.
163. Wang, X. and Lee, P.S., *A polydopamine coated polyaniline single wall carbon nanotube composite material as a stable supercapacitor cathode in an organic electrolyte*. Journal of Materials Research, 2015. **30**(23): p. 3575-3583.
164. Song, C., Park, S.J., and Kim, S., *Effect of Modification by Polydopamine and Polymeric Carbon Nitride on Methanol Oxidation Ability of Pt Catalysts-Supported on Reduced Graphene Oxide*. Journal of The Electrochemical Society, 2016. **163**(7): p. F668-F676.
165. Hu, D., *et al.*, *Indocyanine green-loaded polydopamine-reduced graphene oxide nanocomposites with amplifying photoacoustic and photothermal effects for cancer theranostics*. Theranostics, 2016. **6**(7): p. 1043.
166. Ji, M., *et al.*, *Near-Infrared Light-Driven, Highly Efficient Bilayer Actuators Based on Polydopamine-Modified Reduced Graphene Oxide*. Advanced Functional Materials, 2014. **24**(34): p. 5412-5419.
167. Cui, M., *et al.*, *Polydopamine coated graphene oxide for anticorrosive reinforcement of water-borne epoxy coating*. Chemical Engineering Journal, 2018. **335**: p. 255-266.
168. Fu, L., *et al.*, *Preparation and electrocatalytic properties of polydopamine functionalized reduced graphene oxide-silver nanocomposites*. Electrocatalysis, 2015. **6**(1): p. 72-76.
169. Huang, K.-J., *et al.*, *A sensitive electrochemical DNA biosensor based on silver nanoparticles-polydopamine@ graphene composite*. Electrochimica Acta, 2014. **118**: p. 130-137.
170. Qu, K., *et al.*, *Graphene oxide-polydopamine derived N, S-codoped carbon nanosheets as superior bifunctional electrocatalysts for oxygen reduction and evolution*. Nano Energy, 2016. **19**: p. 373-381.
171. Qu, K., *et al.*, *Polydopamine-graphene oxide derived mesoporous carbon nanosheets for enhanced oxygen reduction*. Nanoscale, 2015. **7**(29): p. 12598-12605.
172. Thangavelu, K., *et al.*, *Electrochemical determination of caffeic acid in wine samples using reduced graphene oxide/polydopamine composite*. Journal of The Electrochemical Society, 2016. **163**(14): p. B726-B731.

173. Li, F., *et al.*, *Electroactive gold nanoparticles/polyaniline/polydopamine hybrid composite in neutral solution as high-performance sensing platform*. Analytical Methods, 2011. **3**(7): p. 1601-1606.
174. Cha, I., *et al.*, *Facile electrochemical synthesis of polydopamine-incorporated graphene oxide/PEDOT hybrid thin films for pseudocapacitive behaviors*. Synthetic Metals, 2014. **195**: p. 162-166.
175. Lee, W., *et al.*, *Simultaneous enhancement of mechanical, electrical and thermal properties of graphene oxide paper by embedding dopamine*. Carbon, 2013. **65**: p. 296-304.
176. Liu, K., *et al.*, *Adsorption and removal of rhodamine B from aqueous solution by tannic acid functionalized graphene*. Colloids and Surfaces A: Physicochemical and Engineering Aspects, 2015. **477**: p. 35-41.
177. Xu, J., *et al.*, *Hierarchical nanocomposites of polyaniline nanowire arrays on graphene oxide sheets with synergistic effect for energy storage*. ACS nano, 2010. **4**(9): p. 5019-5026.
178. Hong, X.D., *et al.*, *Three-dimensional reduced graphene oxide/polyaniline nanocomposite film prepared by diffusion driven layer-by-layer assembly for high-performance supercapacitors*. Journal of Power Sources, 2017. **343**: p. 60-66.
179. Zhang, J., *et al.*, *N-substituted carboxyl polyaniline covalent grafting reduced graphene oxide nanocomposites and its application in supercapacitor*. Electrochimica Acta, 2016. **199**: p. 70-79.
180. Zheng, L., *et al.*, *Facile preparation of polydopamine-reduced graphene oxide nanocomposite and its electrochemical application in simultaneous determination of hydroquinone and catechol*. Sensors and Actuators B: Chemical, 2013. **177**: p. 344-349.
181. Luo, J., *et al.*, *Layer-by-layer self-assembled hybrid multilayer films based on poly (sodium 4-styrenesulfonate) stabilized graphene with polyaniline and their electrochemical sensing properties*. RSC Advances, 2013. **3**(39): p. 17866-17873.
182. Coşkun, E., Zaragoza-Contreras, E.A., and Salavagione, H.J., *Synthesis of sulfonated graphene/polyaniline composites with improved electroactivity*. Carbon, 2012. **50**(6): p. 2235-2243.
183. Cho, S., *et al.*, *Fabrication of water-dispersible and highly conductive PSS-doped PANI/graphene nanocomposites using a high-molecular weight PSS dopant and their application in H₂S detection*. Nanoscale, 2014. **6**(24): p. 15181-15195.
184. Cai, X., *et al.*, *Surfactant-assisted synthesis of reduced graphene oxide/polyaniline composites by gamma irradiation for supercapacitors*. Journal of Materials Science, 2014. **49**(16): p. 5667-5675.
185. Yoo, S., *et al.*, *Ammonia gas detection by tannic acid functionalized and reduced graphene oxide at room temperature*. Journal of Nanomaterials, 2014. **2014**.
186. Luo, J., *et al.*, *Tannic acid induced self-assembly of three-dimensional graphene with good adsorption and antibacterial properties*. ACS Sustainable Chemistry & Engineering, 2016. **4**(3): p. 1404-1413.

187. Sun, C., *et al.*, *Adsorption removal of tannic acid from aqueous solution by polyaniline: Analysis of operating parameters and mechanism*. Journal of colloid and interface science, 2017. **487**: p. 175-181.
188. Li, Y., *et al.*, *Iron-tannic acid nanocomplexes: facile synthesis and application for removal of methylene blue from aqueous solution*. Digest Journal of Nanomaterials & Biostructures, 2016. **11**(4): p. 1045-1061.
189. Saito, R., *et al.*, *Raman spectroscopy of graphene and carbon nanotubes*. Advances in Physics, 2011. **60**(3): p. 413-550.
190. Bo, Z., *et al.*, *Green preparation of reduced graphene oxide for sensing and energy storage applications*. Scientific reports, 2014. **4**.
191. Bose, S., *et al.*, *Dual role of glycine as a chemical functionalizer and a reducing agent in the preparation of graphene: an environmentally friendly method*. Journal of Materials Chemistry, 2012. **22**(19): p. 9696-9703.
192. Gong, Y., *et al.*, *Influence of graphene microstructures on electrochemical performance for supercapacitors*. Progress in Natural Science: Materials International, 2015. **25**(5): p. 379-385.
193. Pantoja Castro, M.A. and González Rodríguez, H., *Study by infrared spectroscopy and thermogravimetric analysis of tannins and tannic acid*. Revista latinoamericana de química, 2011. **39**(3): p. 107-112.
194. Božič, M., Gorgieva, S., and Kokol, V., *Homogeneous and heterogeneous methods for laccase-mediated functionalization of chitosan by tannic acid and quercetin*. Carbohydrate polymers, 2012. **89**(3): p. 854-864.
195. Shao, Y., *et al.*, *Design and mechanisms of asymmetric supercapacitors*. Chemical reviews, 2018. **118**(18): p. 9233-9280.
196. Yang, S., *et al.*, *New -Generation Graphene from Electrochemical Approaches: Production and Applications*. Advanced Materials, 2016. **28**(29): p. 6213-6221.
197. Xia, Y., *et al.*, *Thickness-independent capacitance of vertically aligned liquid-crystalline MXenes*. Nature, 2018. **557**(7705): p. 409.

Publications and Conference Contributions

1. Xueyan Zhao, Minoj Gnanaseelan, Dieter Jehnichen, and Jürgen Pionteck, Green and Facile Synthesis of Polyaniline/Tannic Acid-rGO Composites for Supercapacitor purpose (submitted);
2. Xueyan Zhao, Olga Grätz, and Jürgen Pionteck. Effect of dopant and oxidant on the electrochemical properties of polyaniline/graphite nanoplate composites. 2018, Polymer International, 67 (10), 1429-1437, DOI: 10.1002/pi.5663;
3. Xueyan Zhao, Olga Grätz, and Jürgen Pionteck. Electrochemical properties of PANI/GNP composites: Effect of dopant and oxidant. Poster, Graphene 2018 conference, 2018, Dresden, Germany;
4. Xueyan Zhao, Olga Grätz, and Jürgen Pionteck. Effect of dopant and oxidant on the electrochemical properties of PANI/GNP composites. Poster, 3rd NanoCarbon Annual Meeting, 2017, Würzburg, Germany;
5. Xueyan Zhao, Olga Grätz, and Jürgen Pionteck. Effect of dopant and oxidant on the electrochemical properties of PANI/GNP composites. Poster, 17th APME conference, 2017, Ghent, Belgium.

Acknowledgement

The research works presented in this thesis were realized with the help and support from many people. First of all, I would like to thank Prof. Brigitte Voit for being my academic supervisor. She is always patient and pleasant to give me advises. With her guide, I meet many excellent PhD students and had the opportunity to join some academic conferences. Then I want to sincerely thank Dr. Petra Pötschke for let me join in her research group. She binds group members with different research background together and created many chances for us to communicate with other researchers.

In particular, I would like to thank my supervisor Dr. Jürgen Pionteck. He gave me lots of valuable advices and suggestions on my research works, and guided me to become a free-thinking and independent researcher. Moreover, he introduced me lots of knowledge on the culture and life of Germany.

Many thanks to China Scholarship Council for the scholarship (grant No. 201506240099) and for realizing my wish of studying in Germany. This experience is helpful to my academic career and meaningful in my life.

Here, I really thank Mrs. Olga Grätz and Dr. Kai Ke for their kindly help and advices to my research and life, especially in the beginning half year.

I appreciate Dr. Dieter Jehnichen for the XRD test and analysis, Mr. Minoj Gnanaseelan for the SEM test, Dr. Victoria Albrecht for the BET test, Mrs. Kerstin Arnhold for the thermal analysis, Dr. Dieter Fisher for Raman test, Dr. Frank Simon for XPS test, and Dr. Petr Formanek for EDX analysis. I am grateful to Dr. Lothar Jakisch for the guide of FTIR measurement, Dr. Beate Krause for the guide of conductivity test, and Dr. Mazen Azizi for teaching me electrochemical test. Thank SGL Carbon for provide the expanded graphite.

I want to express thanks to many colleagues who gave me suggestions on my research work and shared with me many good ideas. They are Mr. Yilong Li, Mr. Yian Chen, Mr. Xinlei Tang, Mr. Xueyi Wang, Dr. Jianwei Zhang, Dr. Qiang Wei, and Dr. Xinjie Zan.

Besides, special thanks to Dr. Ulrike Staudinger and Ms. Luise Hilbig, who did really care about my life in Germany, and do their best to help me adapt the environment and improve my German language.

Many thanks are delivered to the other colleagues in IPF, especially the members of NB department.

Last but most importantly, I thank my parents, my boyfriend Kai Ni, and many other family members. They give me lots of support and encouragement. Even though I study abroad, I know they are always there for me.

Versicherung

Hiermit versichere ich, dass ich die vorliegende Arbeit ohne unzulässige Hilfe Dritter und ohne Benutzung anderer als der angegebenen Hilfsmittel angefertigt habe; die aus fremden Quellen direkt oder indirekt übernommen Gedanken sind als solche kenntlich gemacht. Die Arbeit wurde bisher weder im Inland noch im Ausland in gleicher oder ähnlicher Form einer anderen Prüfungsbehörde vorgelegt.

Datum:

Unterschrift:

Erklärung

Die vorliegende Arbeit wurde in der Zeit von Oktober 2015 bis Januar 2019 am Leibniz-Institut für Polymerforschung Dresden e.V. im Rahmen des Projektes zum Thema: “Modification of the Electrochemical Properties of Graphite-based Polyaniline Composite for Supercapacitor Application” unter wissenschaftlicher Betreuung von Prof. Dr. rer. nat. habil. Brigitte Voit und Dr. rer. nat. Jürgen Pionteck durchgeführt.

Datum:

Unterschrift: